DIVERSE SOURCES OF NOISE IN BIOLOGICAL SYSTEMS

by

Matthew David Brennan

A dissertation submitted to Johns Hopkins University in conformity with the requirements for the degree of Doctor of Philosophy

Baltimore, Maryland

November, 2015

ABSTRACT

Variation is omnipresent in biological systems. Organisms must survive in fluctuating environments, genetic diversity drives evolution, and finite molecule counts challenge signal processing accuracy. However, in classic cellular biology, this variation is often ignored. While a dose-response curve may show error bars, these are often attributed to measurement error and not assumed to be true biological variation, or noise. Recently, however, sufficiently powerful technology has been developed to measure response of many cells at the single-cell level. These studies have raised significant questions in cellular and systems biology, requiring the development of new methods and revisiting of old models.

In this manuscript, we first develop a novel method based on organism symmetry for differentiating between sources of noise. We apply this method to Drosophila early morphogenesis dorsal-ventral (D-V) cell differentiation. We identify significant position-dependent structure to the noise. Given commonality of organisms exhibiting bilateral symmetry, this method can find very wide applicability. Further, by leveraging information, we are able to demonstrate which components of the noise have a significant effect on Drosophila development. We then investigate noise in the context of a multicellular organism performing gradient detection. In contrast to previous studies, which have focused only on noise outside of the cell, we find that noise inside the cell contributes significantly to gradient detection accuracy. In particular, as a cell grows however, internal communication noise is also expected to grow, complicating comparison of concentrations. We discover this effect

through a combination of using linear mathematics, nonlinear simulations, and *in vivo* experiments on multicellular organoids, we show that results obtained by ignoring internal system variation are incomplete. Finally, we consider noise in the context of a system which must detect signal duration despite variation in the signal amplitude. We show that the Incoherent Type 1 Feed Forward Loop (I1FFL), one of the most common network motifs, is capable of accurately performing this detection function. Taken together, these contributions provide new analytical tools, shed additional light on the importance of biological noise, and support an increasingly wide-held view that variation is a fundamental aspect of biology.

Advisor: Andre Levchenko, PhD

Thesis Committee: Joel Bader, PhD; Takanari Inoue, PhD; Andre Levchenko, PhD

Thesis Readers: Joel Bader, PhD; Andre Levchenko, PhD

ACKNOWLEDGEMENTS

Many individuals have supported and encouraged me along the path leading up to this dissertation. I would first like to thank my advisor, Dr. Andre Levchenko, for constant guidance, and giving me interesting projects to work on as soon as I was a rotation student in the lab. He was patient when I was pitching him on crazy new ideas, and when I wasn't understanding his great ones. I am particularly greatful to have learned from his ability to put the minutiae of a research project in to a broader scientific context.

I would also like to thank my committee members, Dr. Joel Bader and Dr. Takinari Inoue. Besides providing helpful feedback and generosity with their schedules, meeting both of them during the Hopkins interview process was a strong factor in my decision to matriculate.

Before arriving at Johns Hopkins, several other mentors were kind enough to guide my experience in academia. Dr. Dennis Goeckel, after being a great teacher and advisor, was the first to make me think that getting a PhD might be a good idea. Dr. Giusseppe Caire was a patient mentor at USC as I tackled the research challenges he gave me, and was the first to support my foray in to the intersection of information theory and biology. And most recently, Dr. Tara O'Toole, whose passion for biosecurity and voracious appetite for books encouraged me to return from government to complete my studies in biomedical engineering.

It would be wrong of me to omit POTUS, whose inspiration caused me to abandon my first PhD attempt to join government service, meet many friends and new mentors, and pivot my research focus from electrical engineering to biomedical engineering. Thanks, Obama.

During my studies I was able to interact with many great individuals. I owe much gratitude to my primary collaborators, Drs. Bomyi Lim, Andrew Mugler, Stas Shvartsman, and Ilya Neyneman. They shared experience, advice, and data with me that was crucial to the completion of this dissertation. Within the Levchenko Lab, all lab members were good friends, welcoming me warmly to the lab and sharing their advice on how to be successful. I would like to particularly thank Drs. Raymond Cheong and Alex Rhee. Raymond generously provided research ideas and was a close mentor and great scientist whose approval I held in high esteem. Alex provided perspective on the world outside of academia, the importance of staying on task, and a constant sounding board for research directions.

For three decades, my parents, Robert and Diane, have given me all of the love and support necessary to get to this point as a happy person. They moved their lives so my sister and I could be in a good school district, have always been encouraging and supportive of directions I thought were the right to take (guided by the values they gave me), and didn't cry that much when I left my first PhD. Finally, my wife Laura, whose job as a teacher has been much harder than mine, always did everything possible to encourage me, make my life easier, and create a home full of love.

TABLE OF CONTENTS

LIST OF TABLES

LIST OF FIGURES

Chapter 1 Introduction and Background

Variation is everywhere in biological systems [1-6]. Organisms must survive in fluctuating environments, genetic diversity drives evolution, and finite molecule counts challenge signal processing accuracy. However, in classic cellular biology, this variation is often ignored. While a dose-response curve may show error bars, these are typically attributed to measurement error and not assumed to be true biological variation, or noise. However, differences in individual cells have been observed for nearly as long as microscopes have existed [7]. Only recently, however, has technology proved sufficiently powerful to measure response of many cells at the single-cell level. These studies have raised significant questions in cellular biology, particularly when isogenic cells make different decisions to the same apparent input, or are able to make similar decisions despite stochastically varying input.

Clearly, even just from the list mentioned above, biological noise can arise from many sources, and may have a positive or negative impact on an organism. Genetic diversity can arise from copy errors or environmental factors, and while it drives evolution it may also drive disease. In gene expression, transcription may also fluctuate greatly. As shown by Swain and Elowitz, such noise may have multiple components which may be decomposed [8, 9]. In the case of gene transcription, an "extrinsic" component exists, which includes variable numbers of ribosomes, as well

as an “intrinsic” component, which includes fluctuations due to stochastic chemical interactions.

Intrinsic and Extrinsic Noise in Drosophila Development

In this manuscript, we first develop a novel method based on organism symmetry for differentiating between sources of noise. We apply this method to Drosophila early morphogenesis dorsal-ventral (D-V) cell differentiation. The D-V patterning in Drosophila is primarily driven by a single morphogen gradient, Dorsal, an NF-κB homologue [10, 11]. We identify significant position-dependent structure to the noise. Given commonality of organisms exhibiting bilateral symmetry, this method can find very wide applicability. Further, by leveraging information we are able to demonstrate which components of the noise have a significant effect on Drosophila development. While information theory has become increasingly popular in cellular signaling studies, we also apply the concept of entropy, a measure of decision uncertainty, to understand the quantified information in perspective of the complexity of the information required. This concept is currently underutilized in much of systems biology literature.

Internal and External Noise in Gradient Detection

Chemoreception and gradient detection in particular are a key biological process which, when disregulated, contribute to cancer metastasis. Noise has been long recognized as a challenge to chemoreception [12]. In gradient detection, cells must distinguish between the value of a gradient at opposite ends of their membranes. A

simple analysis of this noise may suggest that larger cells can detect shallower gradients, since the absolute difference of concentrations at each end of the cell will be larger, overcoming the noise [13].

These works, however, have largely focused on noise from small counts of molecules outside of the sensing system, while ignoring the fact messages must be conveyed inside the system in order to understand relative strength. In particular, as a cell grows however, internal communication noise is also expected to grow, complicating comparison of concentrations. By using linear mathematics, nonlinear simulations, and *in vivo* experiments on multicellular organoids, we show that results obtained by ignoring internal system variation are incomplete. Indeed, while previous theory suggests that a larger and larger system may detect a gradient with ever-improving precision, we show that there are sharp limitations on that benefit due to the limits placed by internal noise. As we conclude in the chapter, "our analysis provides a way to assess the potential role of inter-cellular communication in other settings, including invasive tumor growth, pointing to the specific parameters that can be altered to disrupt this process or make it less efficient."

Amplitude Noise in Duration Detection

While much work on noise has focused on how it adds to or multiplies a signal, it is also possible for random variation along orthogonal axes to affect signal detection. Recent work suggests that duration of a signal may be important in cell differentiation [14, 15]. The amplitude of a signal (such as molecular concentration) may in this case be considered orthogonal to the actual signal of interest (duration).

However, since the simplest detection circuits generally work as integrators, this amplitude will affect their output.

The Incoherent Type 1 Feed Forward Loop (I1FFL) is one of the most common network motifs, and has several identified functions including pulse generation, response time reduction, and fold-change detection [16-19]. In this proposal, we will demonstrate a new function: its ability to accurately decode signal duration in the presence of such extrinsic noise.

Despite results highlighting the importance of signal duration, little work has been done on identifying circuits which can differentiate signals based on duration. One prime example is the case of T Cell differentiation [15, 20]. While T Cell fate has been shown to be linked to stimulation duration, it is not clear how this may happen robustly in the face of stimulus amplitude, which may vary slowly relative to detection. By identifying even one such circuit, we will provide a plausible mechanism and will highlight duration detection as a fundamental line of inquiry.

Most simple signaling networks, such as an integrator, respond both to amplitude and duration of input. I have explored how the Type 1 incoherent feed-forward loop, a common signaling network motif, may measure signal duration while ignoring amplitude variation. Despite being a well-studied motif, this feature has previously been undiscovered, and is only revealed by considering the correct framework of noise.

INFORMATION-THEORETIC METRICS

Across multiple aims and experiments in this manuscript, information-theoretic metrics will be used to quantify the effects and limitations of noise. In particular, we will use information theoretic entropy to measure the complexity of a desired outcome and capacity to measure the amount of information that may be derived from a signal [21, 22]. These metrics are defined as

$$H = -\sum_{x} p_x \log p_x$$

$$C = \max_{p_x} I(X;Y)$$

$$\begin{aligned} I &= H(X) - H(X|Y) \\ &= H(Y) - H(Y|X) \\ &= \sum_{x,y} p_{x,y} \log \frac{p_{x,y}}{p_x p_y} \end{aligned}$$

While we will be applying this metric to new systems, capacity has been repeatedly shown to be useful in biological contexts. It measures how much information is transmitted through a noisy biochemical signaling process [23, 24] and places limits on how accurately a cell may utilize signaling outputs to discriminate between different input signals. Note that this analysis is independent of the mechanisms used by the system, only on its outputs. Further, by maximizing over the possible input probability distributions, Capacity becomes a function solely of the system defined as P(Y|X), or P(output|input).

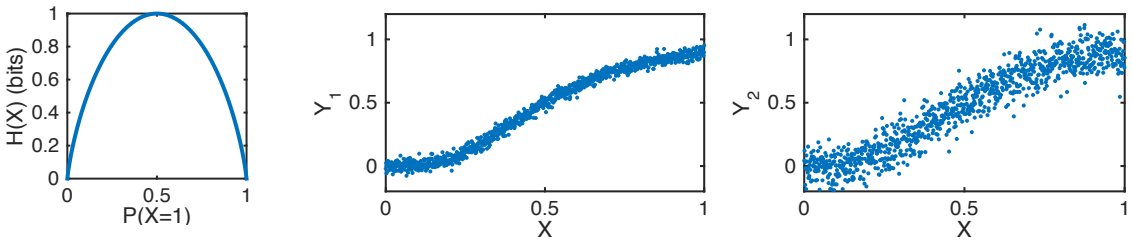

FIGURE 1: ENTROPY AND MUTUAL INFORMATION

a) The entropy of a Bernoulli random variable, where the probability of X=1 is along the horizontal axis. Note that entropy increases as outcome uncertainty increases. B) Samples drawn from two different distributions of P(Y|X). On the left, $I(X;Y_1)$ = 3.1 bits. On the right, as the relationship is weekend, $I(X;Y_2)$ = 2.0 bits.

Noise Deconvolution in a Symmetric System

Deconvolution of noise, or separating out its key components, is a current trend in systems biology research. Many biological processes, including the development of the Dorsal gradient during *Drosophila Melanogaster* development, are bilaterally symmetric processes. This symmetry provides us with two measurements of the same process. In general, we can use these dual measurements to separate the total observed variability in the output of a process into symmetric and asymmetric noise components in a manner analogous to the extrinsic-intrinsic decomposition of gene expression noise developed in [8]. We consider L and R to be measurements of a symmetric process such that

$$\begin{aligned} \mathrm{L} &= f + \gamma_S + \gamma_{A,L} \\ R &= f + \gamma_S + \gamma_{A,R} \end{aligned}$$

We assume that f is the deterministic part of the signal on which L and R are based. γ_S is a single random value which is added to both L and R, where $\gamma_{A,L}$ and $\gamma_{A,R}$ are random values added to the L and R values respectively. We assume that all three

random values are zero mean, that all three are independent of each other, and that $\gamma_{A,L}$ and $\gamma_{A,R}$ are identically distributed. Based on observations of L and R, it is then straightforward to determine the variance of the random values:

$$\begin{aligned}\mathrm{Cov}(L,R) &= \mathrm{Cov}\left(f+\gamma_S+\gamma_{A,L}, f+\gamma_S+\gamma_{A,L}\right)\\ &= \mathrm{Cov}\left(\gamma_S+\gamma_{A,L}, \gamma_S+\gamma_{A,L}\right)\\ &= \mathrm{Var}(\gamma_S)+\mathrm{Cov}\left(\gamma_S,\gamma_{A,L}\right)+\mathrm{Cov}\left(\gamma_S,\gamma_{A,R}\right)+\mathrm{Cov}\left(\gamma_{A,L},\gamma_{A,R}\right)\\ &= \mathrm{Var}(\gamma_S)=\sigma_S^2\end{aligned}$$

$$\begin{aligned}\mathrm{Cov}(L,R)-{}^1\!/_2\left[\mathrm{Var}(L)+\mathrm{Var}(R)\right] &= \mathrm{Var}(\gamma_S)-{}^1\!/_2\left[\mathrm{Var}(L)+\mathrm{Var}(R)\right]\\ &= \mathrm{Var}(\gamma_S)-{}^1\!/_2\begin{bmatrix}2\mathrm{Var}(\gamma_S)+\mathrm{Var}\left(\gamma_{A,L}\right)+\mathrm{Var}\left(\gamma_{A,R}\right)+\\ \mathrm{Cov}\left(\gamma_S,\gamma_{A,L}\right)+\mathrm{Cov}\left(\gamma_S,\gamma_{A,R}\right)\end{bmatrix}\\ &= {}^1\!/_2\left[\mathrm{Var}\left(\gamma_{A,L}\right)+\mathrm{Var}\left(\gamma_{A,R}\right)\right]\\ &= \mathrm{Var}\left(\gamma_{A,L}\right)=\sigma_{A,L}^2=\sigma_{A,R}^2\end{aligned}$$

Symmetric noise is mathematically analogous to extrinsic noise, although in this setting it represents variability that causes the process in one organism to be different than another. Asymmetric noise is mathematically analogous to intrinsic noise, although here it affects one half of the process differently than the other within the same embryo. We can perform this decomposition at every point of a spatially dynamic process and examine how each noise component scales as a function of position.

Chapter 2 How Information Theory Handles Cell Signaling and Uncertainty

Authors

Matthew D. Brennan, Raymond Cheong, Andre Levchenko

Perspective

Intracellular biochemical networks have traditionally been studied by stimulating populations of genetically identical cells and measuring the aggregate response. However, such population-based measurements may obscure the idiosyncrasies of individual cells and therefore suggest deceptively precise input-output relationships. Consequently, signaling pathways have been viewed as the finely tuned circuitry that programs the cell to behave in a predefined manner [25]. Detailed study of cellular biochemistry at the single-cell level now show that cells responding en masse have quite varied behaviors when examined individually [26], raising the question of how precisely signaling pathways can control a cell's actions [27].

It is likely that under most circumstances, cell populations constantly diversify their states, which is indicative of individual cells' ability to adopt functionally distinct states [28]. Thus, there is an uncertainty in signaling outcomes, and responses of cells randomly selected from a population are unpredictable. In this sense, the match between the environmental input and the cellular output can no longer be predefined

and stereotypically precise [1], which hampers the ability of individual cells or small cell ensembles to make decisions in a fluctuating environment, and leads to a fundamentally different view toward analyzing signaling systems. Hence, rather than defining and using seemingly robust and sensitive signaling input-output dependencies to analyze networks and cell behavior, we should instead seek to learn the limits to how well cell signaling can enable decision making, given a cell's uncertain response to changes in the environment.

Variability in cell response is referred to as "noise" and current metrics to characterize noise report on its magnitude but do not quantify how the noise limits the cell's decision-making abilities [6]. Indeed, performance of a signaling network depends on more than just its underlying chemistry. For instance, signaling may be viewed as allowing a cell to "choose" one of several distinct classes of behavior—a type of cellular bet hedging—which can improve some aspects of decision-making but with a cost of increased variability [29]. Therefore, a new "language" may be needed to understand and quantify the impact of noise (variability) on a cell's functionality.

Mathematics is an appropriate language, and provides theory to support it. Indeed, mathematics has already been adopted to understand the workings of another type of "noisy" signaling network, the nervous system [30]. Created to analyze uncertainty in human communication, "information theory" enables the limits of decision-making fidelity to be rigorously defined and measured [31]. Conveniently, its general formulation permits analysis of many complex systems, including those found in biological signaling [32]. Within this theory and in the context of signaling,

information is quantified as the uncertainty in cell behavior that is removed by signaling activity (this should match the knowledge gained by a signaling system about the environment). The amount of information depends on both the amount of variability in the environment (the initial level of uncertainty) and noise in the signaling process itself (affecting the amount of uncertainty remaining). Extending this definition, we can also determine the information capacity of a system, which is the maximum information that a signaling system can obtain about some aspect of the environment under ideal conditions. This capacity is an intrinsic property of the signaling system, as much as the underlying chemistry, in that it is the key determinant of achievable decision-making fidelity [22].

As an example, consider a signaling pathway whose output measures the concentration of an extracellular ligand (i.e., a dose response). Signaling noise prevents a cell from determining the precise ligand concentration. However, does the noise also prevent a cell from resolving different concentrations of the ligand, and if so, how many and how accurately? Information theory states that it is possible to use the noisy signaling output to accurately discriminate different input doses [22]. Furthermore, the number of resolvable concentrations is limited, and is a simple function of the pathway capacity [23]. Alternatively, if mistakes do occur, the capacity determines the minimum amount of error that a cell must tolerate, with higher capacity unambiguously allowing for lower error [31]. Information theory allows such categorical statements without necessarily requiring detailed specifics of the signaling network organization and

operation, and thus can be used to analyze the capabilities of complex and incompletely characterized biological systems.

Currently, we do not understand the decision-making limits of the vast majority of signaling systems, even those affected by variability. Consequently, the factors that affect and regulate those limits are also generally unknown. Thus, from the standpoint of information transfer, it is essential to determine the capacities of these signaling pathways and networks, and the relationships between system structure and capacity. For instance, information lost at each step of processing should prevent information sources and destinations from being separated by more than a few intermediates [4, 33]. Simultaneously, it is often necessary to integrate multiple pieces of information within a cell. Both of these considerations drive the formation of so-called small world networks that are widespread in biological systems and other networks, in which a relatively short path connects any two signaling nodes [34]. Such networks are configured so that multiple signals pass through central nodes, thereby raising the information theoretic question of how the signals are multiplexed through the hub so as to minimally interfere with one another [35].

Acquiring information typically costs the cell energy, time, or opportunity, so a signaling system that collects more information than is necessary or ignores information that is easily obtained wastes valuable resources. Therefore, under evolutionary pressure, it's expected that signaling systems are optimally matched to the sources of information they have evolved to process. Indeed, examples from

neuroscience and developmental biology show that biological systems usually have a capacity that is minimally sufficient for the information they process [36, 37].

This optimality principle can answer long-standing questions that cannot currently be addressed through models or direct experiments. One example is determining which of several putative aspects of environmental input (e.g., ligand dose, rate of dose change, or duration of ligand presentation) are biologically relevant. Information-processing optimality suggests that the aspect of the input associated with a higher capacity is the more pertinent one. This concept further implies that the conditions that maximally utilize the information capacity of a sensory system should reflect the natural fluctuations in the environment. These conditions can be computed from controlled laboratory observations, enabling a form of "inverse ecology" that is sometimes the only feasible way to gain insight into a cell's natural surroundings [38] (Figure 2). Similar arguments can be used to infer which aspect of a cell's response to an environmental input is most relevant to that input [39].

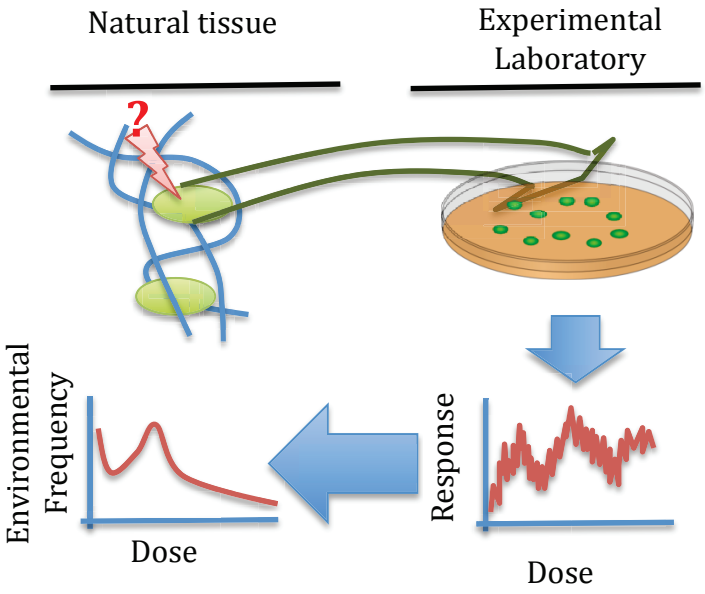

FIGURE 2: INVERSE ECOLOGY

Information theory can provide answers to otherwise unanswerable questions. "Inverse Ecology" uses the principle that organisms have evolved to maximize knowledge of their environment. By experimentally measuring dose-response distributions, one can learn about the environment that the organism evolved to respond to.

As biologists are finding more uses for information theory, it is evolving to handle more complex biological networks [2, 40-42]. By rigorously quantifying the properties and limits of cellular information transfer, new questions will be formulated and answered within the single-cell paradigm shift that is already underway. As the ability to quantify the functionality of signaling networks improves, we will hopefully gain insight into the details of their underlying chemistry while gaining a deeper understanding of their higher-level organization and functionality.

Chapter 3 THE NOISE STRUCTURE AND INFORMATION CONTENT IN THE DORSAL-VENTRAL PATTERNING OF DROSOPHILA EMBRYOS

AUTHORS

Matthew D Brennan[1,2], Bomyi Lim[3], Raymond Cheong[1], Stanislav Shvartsman[3], Andre Levchenko[2]

Affiliations:

[1]Department of Biomedical Engineering, Johns Hopkins University, 3400 North Charles Street, Baltimore, MD 21218, USA. [2]Yale Systems Biology Institute, Yale University, New Haven, CT. [3]Department of Chemical and Biological Engineering and Lewis-Sigler Institute for Integrative Genomics, Princeton University, Princeton, New Jersey, USA.

ABSTRACT

In many developmental systems, multipotent cells measure the local concentration of a morphogen, convert that concentration into an estimate of position, and thus control differentiation and ultimate cell fate. These decisions must be made with sufficient precision for an organism to develop properly, placing requirements on how accurately an individual cell or nucleus must determine the local gradient concentration. Naturally occurring stochastic variation in morphogen gradients raises the question of how accurately developing tissues can be patterned by such instructive inputs. We quantitatively evaluated the levels of nuclear Dorsal, a signal which controls Dorsal-Ventral polarity in *Drosophila* embryos, in hundreds of individual nuclei and at multiple developmental time points. We then developed a

new method to decompose various sources of variability in the Dorsal levels not requiring multiple reporters or detailed dynamical information. This analysis indicated that the Dorsal gradient can be subject to three distinct sources of variability, which nevertheless permit precise patterning and, if partially accounted for, may allow for increased robustness of the developmental process.

INTRODUCTION

Classical theories of morphogenesis propose that concentration gradients of extracellular proteins (known as morphogens) define spatially distinct domains of gene expression and cellular differentiation [11, 43-45]. In *Drosophila* development, the Dorsal-Ventral (D-V) polarity is established prior to gastrulation by the graded nuclear import of Dorsal (Dl), an NF-κB homologue. During nuclear cycle 14, cellular membranes are formed around nuclei, isolating cellular Dl content. Three primary regions of gene expression have been categorized based on the affinity of genes' enhancers for Dl, which roughly correspond to the dorsal ectoderm, the neurogenic ectoderm, and the mesoderm. Furthermore, during this cycle, more specific regions of gene expression arise, with at least six distinct regions of gene expression patterns having direct contributions of Dl to transcriptional regulation [11]. Because of the rarity of phenotypic variation in the fully developed organisms, it is widely believed that embryonic patterning is highly precise [44]. However, this notion must be reconciled with recent observations showing marked variability in morphogen distributions both between individual embryos and within individual embryos [46, 47, 48].

To understand how developmental systems operate robustly when signaling variability is a significant factor, it is important to both quantify the extent to which variability may limit signal precision and to identify the underlying factors which contribute most to this limitation. One convenient way to achieve this is to precisely determine the information content of the morphogenic input [22], which can help quantify another classical concept in developmental biology, the positional

information [24, 49]. In particular, the information capacity of the morphogen gradient, can quantify the maximum amount of positional information that may be conveyed through the mechanisms which link nuclear position to the local concentration of transcription factors and hence to cell differentiation fate. The information capacity metric thus summarizes how the stochastic variability in the morphogen gradient ultimately limits the accuracy of the size and positioning of different cell fate regions. As such, it has previously been applied in the characterization of anterior-posterior patterning in *Drosophila* embryos [49].

While the information capacity provides a useful metric to measure the capability of a morphogen, it does not reveal anything about the underlying sources of signal variability or noise. Noise decomposition methods are frequently used to separate noise into components that are extrinsic and intrinsic to the particular biochemical process [8, 38, 50]. Many of these methods measure correlations between different fluorescent tags targeting the same molecule [51], which can be cumbersome in intact developing systems. Other methods have sought to distinguish between sources of noise by assuming a distribution for the intrinsic noise [52]. Such assumptions are inherently limiting. In this paper, we develop a method of noise decomposition which neither required the development of multiple reporters nor placed assumptions on the structure of the noise. By expanding the mathematical tools used in the decomposition of gene expression noise to bilaterally symmetric biological systems, we can investigate how the different components impact positional information and ultimately limit patterning accuracy.

We combined this new noise decomposition method with information theoretic measures to investigate D-V polarization in *Drosophila* embryos. By leveraging symmetry in the spatial relationship between position and Dl, we characterized the structure within the variability of Dl distribution, identifying at least three distinct sources of noise. Using information capacity as a metric, we evaluated the relative impact of these different noise components on patterning accuracy gaining insight into how *Drosophila* embryos may cope with the inherent developmental noise. In

particular, we found that the positional information available in the Dl gradient is at least sufficient and might substantially exceed the information required for unambiguous cell fate determination, thus ensuring robustness of the patterning process.

RESULTS

HIGH-THROUGHPUT MEASUREMENT OF VARIABILITY IN NUCLEAR DORSAL

In *Drosophila,* D-V axis development is regulated by nuclear transport of the transcription factor Dorsal (Dl), an NF-κB homologue [53-55]. A graded distribution of Toll receptor activation results in the degradation of the Dl inhibitor Cactus, freeing Dl to form a gradient and enter the nucleus [48, 56]. Individual nuclei determine their position in the embryo according to the amount of nuclear Dl, and express genes that regulate differentiation in a manner ultimately dependent on nuclear Dl concentration (Figure 3C) [45, 57, 58]. The levels of nuclear Dl define three fate regions termed Types I, II, and III, which roughly correspond to the future mesoderm, neurogenic ectoderm, and dorsal ectoderm regions [57]. We sought to explore whether and to what degree the variability in Dl gradient would limit the corresponding maximal positional information and thus compromise the patterning capability of the Dl gradient. To achieve this, we first determined and characterized the magnitude and structure of Dl variability within and across multiple Drosophila embryos.

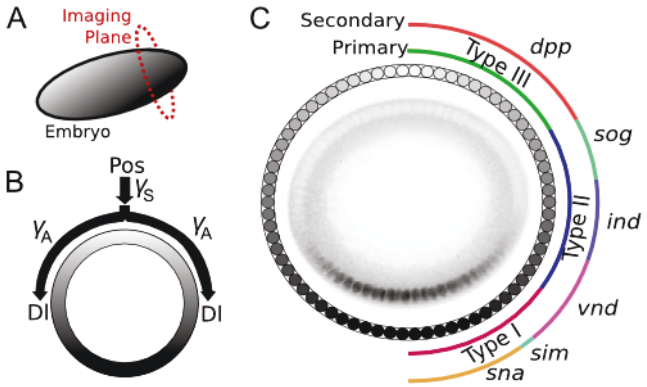

FIGURE 3: ANALYSIS OF THE MAGNITUDE AND VARIABILITY OF DORSAL GRADIENTS

A) A diagram of the ellipsoidal embryo and the perspective of the imaging plane. B) A schematic diagram of how symmetric noise (γ_S), common to two halves of the Dl gradient, and asymmetric (γ_A) noise, which affects the two halves independently, can affect the positional information dependent on the local Dl concentration. Note that while the same asymmetric noise processes affects both sides, its realized local value will generally not be the same. C) Dorsal gradient and specification of primary and secondary cell fates. The center shows a confocal image of a Drosophila embryo immunostained for Dl. The image is inverted, such that high concentrations of Dl appear dark. Surrounding the image is a schematic diagram of the dorsal-ventral gene expression regions, adapted from Hong, et al. (Hong et al., 2008). Primary fate regions are labeled according to their gene promoters' affinity for the Dl transcription factor, while secondary regions are labeled based on representative genes which are expressed in that region.

To investigate the variability in the Dl gradients, we used a previously-described microfluidic device coupled with confocal microscopy and custom image processing software to precisely measure individual nuclei [59] (Figure 3C, SI). Embryonic nuclei were stained with DAPI and an antibody that recognizes Dl. In each of five experiments, we imaged 15-25 embryos, obtaining measurements for hundreds of nuclei in each experiment. Measurements were taken during cell cycle 14, just before the formation of cellular membranes separating the nuclei, a process which freezes the local concentration of Dl, locking-in cellular fate.

At this critical stage of Drosophila embryonic development, we observed variability in the shape of the Dl gradient across embryos as well as within an embryo. Across

embryos, we observed differences in the amplitude and width of the gradient (Figure 4A,B). Within individual embryos, we also examined variability of the Dl profiles along symmetric halves of the sections examined. We found these intra-embryonic Dl distributions to be highly overlapping, but we did observe substantial local differences when comparing Dl concentrations at the same distance along the mirror sides of the Dl gradient (Figure 4A). These observations allowed us to separate the total observed variability in Dl levels into the "symmetric" and "asymmetric" noise components in a manner analogous to extrinsic-intrinsic decomposition of gene expression noise ([8], SI Text). Symmetric noise is mathematically analogous to extrinsic noise, although in this setting it represents variability that equally affects the mirror sides of the Dl gradients. Asymmetric noise is mathematically analogous to intrinsic noise, although here it affects one half of the Dl gradient differently than the other half within the same embryo.

We performed this decomposition at multiple positions around the circumference of the embryo (Figure 4C) and thereby examined how each noise component scaled as a function of Dl concentration (Figure 4D). We found that the relationships between the Dl concentration and both asymmetric and symmetric noise components were non-linear and non-monotonic. In particular, both total and symmetric noise displayed the maximum levels at an intermediate Dl concentration, with a minor peak also found at the maximum Dl levels. On the other hand, the asymmetric noise component displayed monotonic scaling with the Dl levels, up to the maximal concentrations of Dl, where it displayed a slight decrease. Overall, the symmetric noise component was dominant across most of the embryo, constituting the major contribution to the total Dl variability.

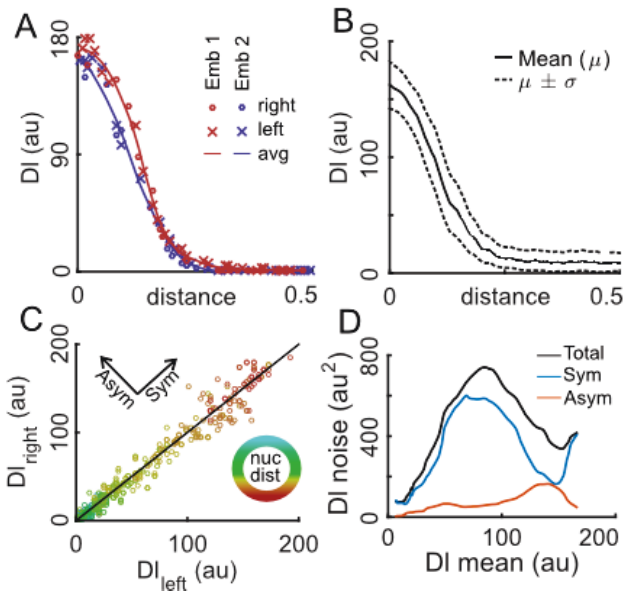

FIGURE 4: MEASUREMENT OF VARIABILITY IN DORSAL GRADIENTS

A) Values of quantified Dl levels in individual nuclei for two example embryos. A smoothened line average based upon the combination of the left and right halves of each embryo is shown, demonstrating variation in the Dl gradient both between embryos and between nuclei at similar positions on different sides of the same embryo. B) The average Dl profile and standard deviation calculated across all embryos. C) A visualization of Dl noise. Left and right nuclei from the same embryos are paired based on their distance from the ventral pole of the embryo. Symmetric noise can be seen as variation along the diagonal line, while asymmetric noise is variation perpendicular to the line. D) A plot of Dl noise vs mean reveals that there is not a simple monotonic relation between the noise and the value of the signal.

NOISE DECOMPOSITION IN A SYMMETRIC SYSTEM REVEALS UNDERLYING STRUCTURE OF NOISE

We next examined the contributions of the asymmetric and symmetric noise components as functions of the dorsoventral position. We again observed that, at any position, symmetric noise tends to be the dominant source of variability in Dl concentration, (Figure 5A,F,K). Of interest, the symmetric noise distribution was not uniform and displayed two major peaks: the first at the position of the maximal Dl concentration, and the second at the position of approximately half-maximal Dl level, suggesting that there might be systematic sources of Dl variability, reflected in

the structure of the symmetric noise component. Indeed, if the position axis was rescaled such that the half-maximal Dl level occurred at the same position for each embryo (the gradient was “width-normalized”), the second peak in symmetric noise was eliminated without affecting the profile of asymmetric noise (Figure 5B,G,L). This suggests that variation in gradient width (here, defined as the distance between the two points where the gradient is reduced by half) is an important source of the symmetric (and total) noise (details on the methods of normalization are provided in Supplemental Material).

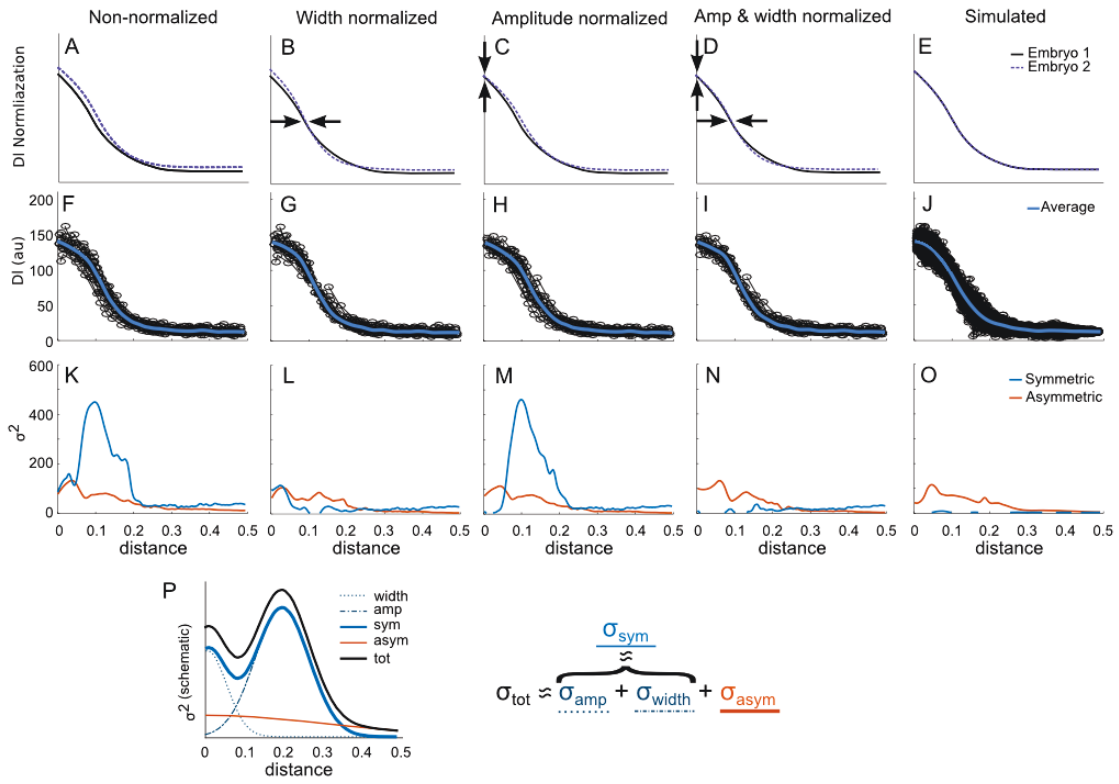

FIGURE 5: NOISE STRUCTURE AND VARIABILITY OF DORSAL GRADIENTS

A-E) Schematic representations of the investigative normalizations yielding different noise components. F-J) Experimental (simulated in J) dorsal profiles, following various normalizations isolating distinct noise components. K-O)Noise components extracted from Dl gradients plotted as functions of normalized position. P) A schematic of the noise structure revealed by distinct normalizations. Total noise is a sum of the symmetric and asymmetric components, with the symmetric noise component primarily accounted by the Dl gradient amplitude and width variability.
To enable the analysis, nuclearized Dl was measured in three experiments, with 15-25 embryos in each experiment. The experimental Dl distributions were width normalized, resulting eliminating the secondary peak of symmetric noise (B,G,L). The experimental Dl distributions were amplitude normalized, eliminating the major peak of symmetric noise (C,H,M). The experimental Dl distributions were both amplitude and width normalized, eliminating nearly all symmetric noise (D,I,N). Simulated Dl distributions generated by subjecting the experimental means of Dl signal to the experimentally characterized asymmetric noise (E,J,O).

In contrast to this gradient "width-normalization," if the maximum levels (amplitude) of each Dl gradient were rescaled to be the same for each embryo

("amplitude-normalized"), the second peak in the symmetric noise distribution remained unchanged (Figure 5C,H,M), but the first peak at the position of the maximal Dl levels was completely removed (Figure 5M). The first peak was not affected when the Dl distributions were width-normalized (Figure 5L). Furthermore, when the gradients were simultaneously amplitude- and width-normalized, the symmetric noise was almost completely removed, whereas asymmetric noise again was unaffected (Figure 5D,I,N). Overall, these results suggested that the symmetric noise component is primarily defined by two sources of variability: the amplitude and the width of Dl gradients across different embryos (Figure 5P). Although the sources of amplitude and width variability could be stochastic, they could also reflect uncertainty inherent in the experimental measurement, as explored below.

The lack of effect of width and amplitude normalization on the distribution of asymmetric noise suggested that it had a more fundamental nature, inherent in the processes leading to the formation of the Dl gradient. To further explore its nature, we tested whether it would display a stochastic distribution, assuming that it may be Gaussian in nature. To accomplish this, we simulated embryos by randomly drawing Dl values from a Gaussian distribution with position-specific mean taken from experimental data (in Figure 5F) and position-specific variance equal to the observed asymmetric noise (in Figure 5K). The resulting noise distribution was completely coincident with the experimentally observed asymmetric noise (Figure 5E,J,O), suggesting that it indeed had a simple stochastic nature, providing important fundamental limitations on the precision of Dl-mediated D-V patterning.

Effect of temporal Dorsal dynamics on noise profiles

We next explored potential sources of variability leading to the symmetric noise component. One such source can be the dynamics of the Dl gradient over the course of the embryo patterning, particularly during cell cycle 14, while the embryo is undergoing significant changes, transitioning most of its nuclei from a syncytium to individual cells [10, 60-62]. The pool of the embryos we sampled for the analysis can

be somewhat asynchronous, suggesting that an extra source of information about the developmental stage of the individual embryos can help explain the observed variability. To investigate how this process affects the noise, we thus labeled embryos from three new experiments with time points based on the length of membrane invagination achieved at the point of staining [63]. We then divided embryos in to three time bins, ensuring there were an equal number of embryos in each bin. Repeating our analysis of noise in the embryos, (Figure 6a) we found that Dl levels indeed exhibited temporal dynamics, which were reflected in the noise profiles. In particular, as developmental time progressed, the first peak of the symmetric noise component (corresponding to amplitude variability) was reduced, whereas the second peak (corresponding to the variability in the gradient width) was apparently unaffected. This was confirmed by decomposition of the symmetric noise into amplitude and width components, by the normalization procedures described above. The results suggested that, indeed, the evolution of the Dl gradient primarily affects the amplitude but not gradient width variability. The asymmetric noise component was also not affected by the temporal dynamics. In summary, these results suggest that the temporal dynamics of Dl gradient is accompanied by a reduction in the degree of variability of the maximum Dl level, but not the variability of the gradient width.

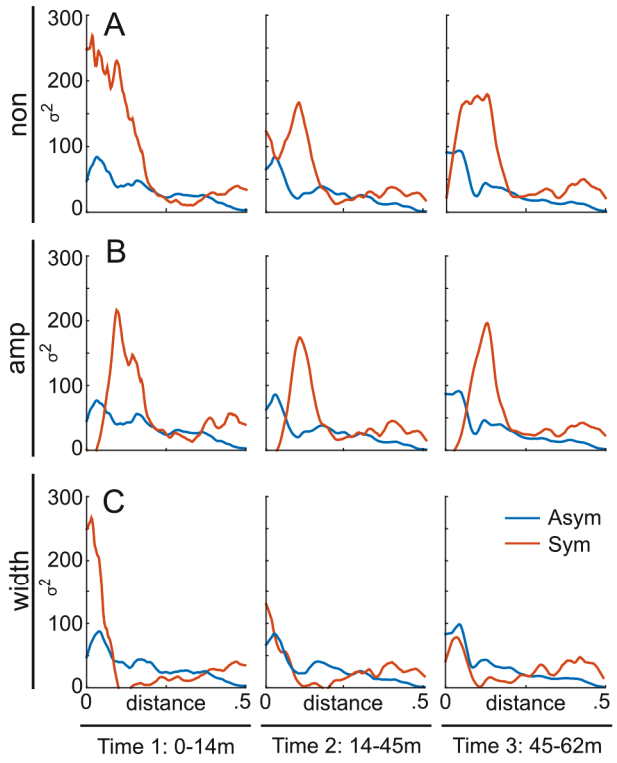

FIGURE 6: TEMPORAL DYNAMICS OF THE DL GRADIENT NOISE STRUCTURE.

Three datasets were tagged with timepoints based on membrane invagination length, where time 0 corresponds to the beginning of cell cycle 14. Embryos were sorted in to three time buckets based on their age at fixation. A) Evolution of noise profiles for non-normalized embryos over time. Notice that as time elapses, the peak at ventral point 0 reduces, while the peak normalized by amplitude noise becomes more prominent. B) Normalizing embryos by amplitude shows that there is not a significant change in the noise previously attributed to width. C) Normalizing embryos by width demonstrates that amplitude noise is greatly reduced over time.

INFORMATION-THEORETIC ANALYSIS QUANTIFIES LIMITS OF MORPHOGEN-BASED PATTERNING

We next sought to determine how precisely the noisy Dl morphogen gradient may specify the position of embryonic developmental regions. Information-theoretic analysis has been recently applied to anterior-posterior axis patterning in early Drosophila embryos [24]. A useful outcome of this method is the determination of the maximum amount of information that can be transferred through a noisy

signaling pathway or transcriptional network. Also known as the information capacity, this value determines number of distinguishable functional outcomes informed by the signaling event [21-23]. In other words, the information capacity places limits on how accurately a biological entity (a cell, a nucleus, a collection of cells or an organism) can discriminate between different input signals, and thus how many distinct responses it can achieve based on this information. We therefore analyzed the information capacity of Dl-mediated patterning, by considering the positional information capacity provided by the nuclear Dl concentration. This capacity quantitatively evaluates how accurately each cell can use its local Dl level to determine its position within the embryo in order to adopt the spatially appropriate differentiation fate. Note that this analysis is independent of the mechanism used by the cell (e.g., the enhancers of genes that are differentially sensitive to different Dl levels) to read out the Dl concentration.

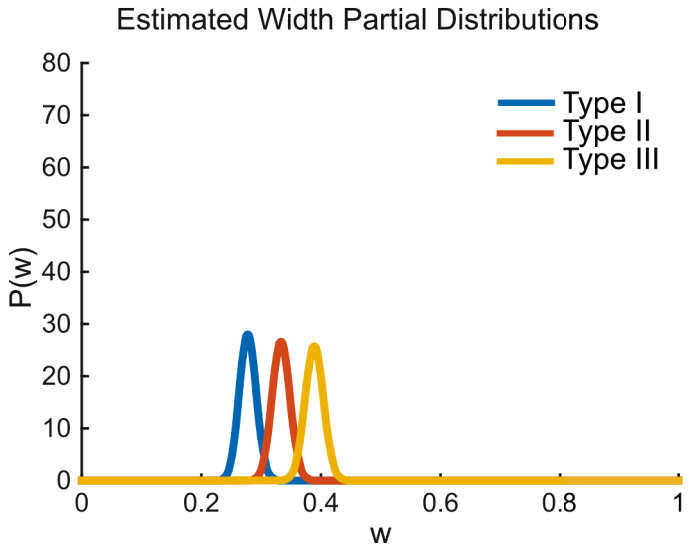

FIGURE 7: ESTIMATION OF ENTROPY OF (AND THUS INFORMATION REQUIRED TO SPECIFY) THE PRIMARY REGIONS OF DL-REGULATED GENE EXPRESSION

Detailed imaging of gene boundaries reveals variability in width along the length of an embryo and from embryo-to-embryo [36]. Indeed, Drosophila embryos vary in diameter by around 2% (Markow et al., 2009). In order to estimate the entropy of the gene domains, we calculated mean and standard deviation of the entropy of samples from a Dirichlet distribution, based on widths of [10 12 14]/36 (see Fig. 1A). Partial probability distributions are shown. The entropy is found to be 1.57±.01 bits.

Using established methods for estimating the information capacity from finite samples [23], we found that the Dl gradient, if subject to both symmetric and asymmetric noise, is capable of conveying 1.63±0.08 bits of information about position to nuclei. To understand this quantity in terms of how it may or may not limit patterning, we determined the minimum amount of information needed to specify the three primary regions of gene expression without error. We considered a nucleus that may be positioned at a random location along the D-V axis. The probability for a specific nucleus to be within a specific primary fate region is proportional to the width of the region. Using these probabilities, we can directly

apply the definition of entropy [22], quantifying the uncertainty in the fate such a nucleus may thus adopt. Measured in bits, the entropy is directly comparable to the information capacity, and is interpreted as the minimum amount of information required by a nucleus to adopt a position-appropriate fate without error. We estimated these probabilities according to available data on the relative sizes of the fate regions (Figure 3C, Figure 7), finding that the corresponding entropy for the primary regions of expression to be 1.57 bits. Thus, the 1.63 bits of information carried by the Dl morphogen gradient is potentially sufficient for nuclei to determine their position within the three primary gene expression regions without error (Figure 8A).

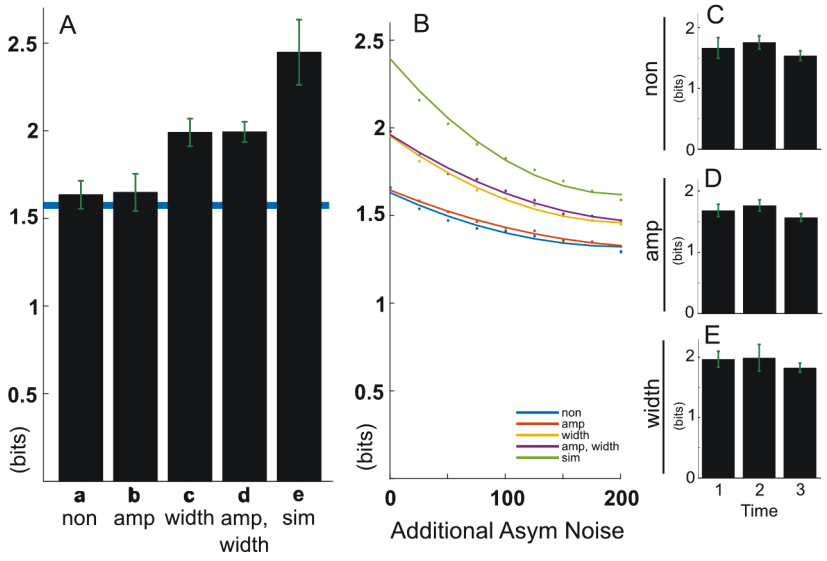

FIGURE 8: IMPACT OF NOISE SOURCES ON THE INFORMATION CAPACITY OF DL GRADIENTS.

A) The positional information capacity of Dl gradient calculated to reflect contributions of different noise components: a, for non-normalized Dl distributions; b, for amplitude-normalized Dl distributions; c, for width-normalized Dl contributions; d, for both amplitude- and width-normalized Dl distributions; e, for simulated Dl distributions lacking symmetric noise. The resulting values of the information capacity of Dl gradients are contrasted with the calculated information needed to unambiguously define either primary (blue horizontal line). Data and error bars are means and standard deviations for n=5 experiments. B) Capacity of the positional information for Dl gradients simulated under various amounts of additional asymmetric noise. The noise was added to either raw experimental Dl distributions, or distributions subject to various normalizations isolating different noise components. C-

E) Capacity of the positional information of the Dl gradient calculated at the different developmental timepoints shown in Fig. 4, calculated for C) non-normalized Dl distributions, D) amplitude-normalized Dl distributions, E) width-normalized Dl distributions.

DORSAL SIGNAL WITHOUT SYMMETRIC NOISE COULD PROVIDE ADDITIONAL INFORMATION

Symmetric noise reflects the inter-embryo variability and, as suggested above, might reflect experimental uncertainty about the timing of the measurement or the exact D-V axis position of the Dl gradient plane. On the other hand, asymmetric noise component is embryo-specific and reflects the intrinsic stochasticity of Dl gradient formation. Therefore, the asymmetric noise component can impose a fundamentally more restrictive limitation on the precision of Dl-mediated patterning. It can thus be of interest to consider how the information content of Dl signal may change if symmetric noise components are individually or jointly "removed" from the total noise affecting Dl gradients. Interestingly, elimination of the "amplitude noise" component did not have a strong effect on the information capacity, yielding 1.65±0.11 bits (Figure 8A). On the other hand, removal of the noise due to variability in the gradient width resulted in a greater information capacity of 1.99±0.08 bits. An argument in favor of this possibility is that this component of noise might be naturally corrected for is that there is an apparent tolerance to the variability in the Dl gradient width along the anterior-posterior axis, at this developmental stage, in spite of variable Dl gradient width [64].

Removal of both gradient amplitude and width noise components similarly increases the morphogenic information capacity to 1.99±0.06 bits. This is the same as the value yielded by the removal of the gradient width uncertainty alone, consistent with no increase in the information capacity following normalization of the gradient amplitude. We have also considered complete elimination of (or, compensation for) the symmetric noise component (see above, and Figure 5E,J,O). Interestingly, the information capacity was very sensitive to the removal of the

residual symmetric noise not accounted for by either gradient amplitude or gradient width variabilities, reaching 2.45±0.19 bits (Figure 8A). Finally, we performed a similar analysis of the information capacity between Dl and the nuclear positions at three developmental time points (Figure 8C-E), finding that the natural temporal variation of the amplitude noise made no significant difference for the value of the information capacity. This result was again in line with the finding that amplitude noise does not have a substantial effect on information capacity. Overall, our results argue that symmetric noise does have a considerable effect on the information capacity of the Dl gradient, with the exception of its amplitude variability component, whose effect is negligible.

ADDITIONAL INFORMATION MAY SERVE AS AN ENVIRONMENTAL BUFFER

As shown above, the amount of information conveyed by Dl may be considerably higher than that required to establish the three primary regions of gene expression, particularly if subject only to asymmetric noise. We considered how this ostensibly excessive information might affect the robustness of Dl mediated gradient patterning. In certain scenarios embryos may be required to develop in an environment with factors, such as variable temperature, which may increase the variability of the patterning signals, including the graded distribution of nuclear Dl. We assume that the resulting variability would be stochastic in nature, and thus primarily increase asymmetric noise. To examine what level of additional noise might compromise the ability to induce appropriate D-V patterning, we simulated Dl gradients with the noise profiles previously determined for each scenario (Figure 5K), but with different levels of additional asymmetric noise. Different levels of asymmetric noise were added at a constant level across the simulated gradients. We then examined the noise levels at which the information capacity drops below the threshold required to robustly induce three patterning zones (Figure 8B). We found that, relative to non-normalized gradients, there was a significant resilience to the added noise that can be introduced, particularly in the case of reduced or eliminated variability in the gradient width. This result argues that intra-embryonic variability

in Dl levels still permits substantial robustness of D-V patterning to factors that can reduce the precision of the chemical gradient formation.

DISCUSSION

Although much has been done to associate positional information with the instructive effects of morphogen gradients, only recently have attempts been made to analyze how noise in morphogen distribution can affect the amount of positional information and thus the fidelity of patterning of developing tissues [24, 49]. Here, we for the first time addressed this question in the context of DV patterning in Drosophila by a well established morphogen, Dorsal. We developed a new technique allowing us to determine the structure of variability in the Dl gradients within an experimentally observed population of *Drosophila* embryos. We found that this variability (or noise) has two major components: the dominant symmetric one, affecting both sides of the Dl gradient in a similar way, and thus primarily stemming from inter-embryonic differences, and the asymmetric one, which affects two sides of the Dl gradient in the same embryo in an uncorrelated fashion, and is thus essentially intra-embryonic in origin. These two components are analogous to commonly used extrinsic (corresponding to symmetric) or intrinsic (corresponding to asymmetric) noise components, with respect to Dl gradient formation [65]. The symmetric noise displayed additional structure, containing identifiable sub-components that could be ascribed to variance in the amplitude and width of Dl gradient. The presence of this structured variability suggests that positional information cannot be infinitely precise. It may be sufficient to establish a pattern of limited complexity, but it may be too constrained by noise to unambiguously define more refined patterns of gene expression in a consistent fashion, either across embryonic population or on two sides of a single embryo. Importantly, our results nevertheless suggest that even in the presence of total (both symmetric and asymmetric) noise, the positional information is sufficient for robustly defining three zones of distinct fates usually assumed to be completely specified by Dl, i.e., presumptive mesoderm, neurogenic ectoderm, and dorsal ectoderm.

The noise structure, revealed by our analysis, suggests that the information can in fact be higher than the simple estimate based on the total noise, particularly if some of the components of the symmetric noise are a part of an experimental rather than endogenous variability, or can be corrected for during embryonic development. Indeed, we found that one of the components of the symmetric noise, the amplitude noise, can decrease over the developmental time, which interestingly coincides with the reported increase in the amplitude of the Dl gradient [61]. This finding suggests that Dl variability can be dynamically controlled and that a precise "time tagging" of the experimental data needs to be performed for unambiguous evaluation of this noise component. However, we also found that the amplitude noise component did not strongly affect the positional information, mitigating the effect of its correction.

The other component of the symmetric noise stems from the uncertainty in the gradient width. Our analysis reveals that this noise component is independent of the developmental time, again consistent with previously observed constancy of the gradient width itself over the same developmental period [61]. However, the width of the Dl gradient varies along the anteroposterior axis, as does the embryo circumference. We found that this component of asymmetric noise had a strong effect on positional information. However, robustness of the developmental patterns to the Dl gradient variation along the A-P axis suggests that either the positional information is sufficient to overcome this component of noise or that there are corrective mechanisms allowing embryos to not be affected by it.

Overall, our data argue that, although the symmetric noise is indeed dominant, it may reflect inherent experimental uncertainty of the embryo analysis, as it may be hard to ensure the consistency of the developmental time or A-P position across multiple embryos within a large population. Conveniently, our method allows to separate this (potentially experimental) source of variability, and focus on the asymmetric noise, intrinsic to nuclear Dl gradient formation. This component constitutes the most fundamental constraint on the precision of developmental patterning by Dl gradient.

The potential for correction of the symmetric noise allows us to question whether the more fundamental constraint of the asymmetric noise can still impose serious limitations on the patterning precision. We found that in this case, the Dl gradient contains more information than needed to define the 3 primary fates, potentially required to ensure robust patterning under less optimal developmental conditions. Developmental outcomes are known to be robust to environmental variations, e.g., in temperature, and also varying dosages of the morphogen, Dl [66, 67]. Such environmental, or genetic, variations may increase the uncertainty or noise in the morphogen distribution or the downstream signaling networks, requiring higher information capacity for a robust outcome. Here, we show that asymmetric noise can indeed be substantially increased without compromising the necessary positional information, accounting for possible high inherent tolerance of the developmental outcomes to environmental perturbations.

In summary, the method proposed in this study allows one to determine the detailed structure of variability in the morphogen distribution from static snapshots of *Drosophila* embryos, and to relate different sources of the variability to identifiable processes in the dynamical evolution of morphogen distribution. Furthermore, the information based analysis can help interpret the role of this variability (or noise) in limiting the capacity of morphogen gradients to establish regions of differential gene expression and cell differentiation. Given commonality of organisms exhibiting bilateral symmetry, this method can find very wide applicability. Specifically, this analysis could be applied to other examples of morphogenic control that display left-right symmetry, e.g. the recent analysis of the wing vein pattern in *Drosophila* [68]. Another attractive feature of the method presented here is its ability to separate the aspects of variability potentially subject to experimental noise (incorporated into the symmetric noise component) from intrinsic variability, based on the relatively simple measurement technique. Overall, this method can help put positional information on a more quantitative footing through quantitative interpretation of the noise sources, both natural and

measurement-related, and by more precise determination of robustness of morphogen-specified tissue pattering to environmental uncertainties.

Materials and Methods

Fly strains

OreR flies were used for all experiments. Flies were cultured and crossed on yeast-cornmeal-molasses-malt extract agar medium at 22°C.

Immunostaining and Microscopy

Mouse anti-Dl (1:100 monoclonal antibody from Developmental Studies Hybridoma Bank) was used as the primary antibody. DAPI (4',6-diamidino-2-phenylindole, 1:10,000; Vector Laboratories) was used to stain the nuclei, and Alexa Fluor conjugates (1:500; Invitrogen) were used as secondary antibodies. Imaging was performed with a Nikon A1-RS confocal microscope with a Nikon 60x 1.4 Plan-Apo oil objective. High-resolution images (1024x1024 pixels, 12 bit depth) were obtained. All images were collected at the focal plane ~85 um from either the anterior or posterior pole. Embryos were imaged in 90% glycerol solution.

Image analysis

DAPI image analysis to identify nuclear boundaries was performed using custom Matlab software adapted from [69]. The perimeter is identified by thresholding the DAPI image channel and identifying the largest object in the image. The maximum value in the DAPI channel is found along 10,000 line segments normal to and equally spaced along the embryo perimeter. A moving average provides an adaptive threshold, and local minima are initial guesses to nuclei boundaries. (Figure 10a). These boundaries are superimposed on the DAPI image (Figure 10b) and a watershed algorithm is applied to identify the outlines of individual nuclei (Figure 10c). Erroneously identified nuclei are filtered out on the basis of candidate nuclei having outlier values of width, height, width/height ratio, and the angle of candidate

nuclei's major axis relative to the perimeter. Dl levels are reported as average pixel intensity of Dl immunofluorescence within each nucleus, and position along the embryo circumference is determined by the closest point along the embryo's perimeter to the nuclei's centroids (Figure 10d,e). Each embryo's profile was fit to a Gaussian curve, and the center of the fit was set as the most ventral point of the embryo (depicted as position 0 in graphs). Embryos where fewer than 30 nuclei could be automatically identified were omitted from further analysis.

Analysis of the noise structure of Dl gradients

Amplitude Normalization: For each two-sided embryo (positions ranging from -0.5 to 0.5), a moving average was used to identify the maximum value of Dl signal for each embryo. Dl values for all embryos were multiplied by the mean of all maximum values, and divided by their respective maximum values, resulting in embryos with equal maximum Dl values. *Width Normalization*: For each embryos, the two points where an embryonic Dl distribution crossed 50% of its maximum (denoted as t), were labeled L_i and R_i, yielding the Dl gradient width estimate: $w_i = L_i - R_i$. Positions of nuclei such thate $L_i \leq pos \leq R_i$ were multiplied by the value of $\text{mean}_i(w_i) / w_i$. The postions of the nuclei with Dl < t and $pos < 0$ were updated by applying $pos = (pos + 0.5) * w_i / \text{mean}_i(w_i) - 0.5$. The postions of the nuclei with $pos < L_i$ were updated by applying $pos = (pos + 0.5) * w_i / \text{mean}_i(w_i) - 0.5$. The postions of the nuclei with $pos < L_i$ were updated by applying $pos = (pos - 0.5) * w_i / \text{mean}_i(w_i) + 0.5$. This maintains embryos with positions ranging from -0.5 to 0.5.

Supplemental Material

Mathematical analysis of the symmetric and asymmetric noise components

We consider L and R to be measurements of a spatially symmetric signal characterizing a stochastic process such that

$$\begin{aligned} L &= f + \gamma_S + \gamma_{A,L} \\ R &= f + \gamma_S + \gamma_{A,R} \end{aligned}$$

We assume that *f* is the deterministic part of the underlying signal constituting symmetrically identical, mirror parts of L and R. γ_S is a single random variable value which affects both L and R, and $\gamma_{A,L}$ and $\gamma_{A,R}$ are random values specific to L and R values respectively. We assume that all three random values have zero mean, that all three are independent of each other, and that $\gamma_{A,L}$ and $\gamma_{A,R}$ are identically distributed. Based on the observations of L and R, it is then straightforward to determine the variance of the random values:

$$\begin{aligned}\mathrm{Cov}(L,R) &= \mathrm{Cov}\left(f+\gamma_S+\gamma_{A,L}, f+\gamma_S+\gamma_{A,L}\right)\\ &= \mathrm{Cov}\left(\gamma_S+\gamma_{A,L}, \gamma_S+\gamma_{A,L}\right)\\ &= \mathrm{Var}(\gamma_S)+\mathrm{Cov}\left(\gamma_S,\gamma_{A,L}\right)+\mathrm{Cov}\left(\gamma_S,\gamma_{A,R}\right)+\mathrm{Cov}\left(\gamma_{A,L},\gamma_{A,R}\right)\\ &= \mathrm{Var}(\gamma_S)=\sigma_S^2\end{aligned}$$

$$\begin{aligned}\mathrm{Cov}(L,R)-{}^1\!/_2\left[\mathrm{Var}(L)+\mathrm{Var}(R)\right] &= \mathrm{Var}(\gamma_S)-{}^1\!/_2\left[\mathrm{Var}(L)+\mathrm{Var}(R)\right]\\ &= \mathrm{Var}(\gamma_S)-{}^1\!/_2\begin{bmatrix}2\mathrm{Var}(\gamma_S)+\mathrm{Var}\left(\gamma_{A,L}\right)+\mathrm{Var}\left(\gamma_{A,R}\right)+\\ \mathrm{Cov}\left(\gamma_S,\gamma_{A,L}\right)+\mathrm{Cov}\left(\gamma_S,\gamma_{A,R}\right)\end{bmatrix}\\ &= {}^1\!/_2\left[\mathrm{Var}\left(\gamma_{A,L}\right)+\mathrm{Var}\left(\gamma_{A,R}\right)\right]\\ &= \mathrm{Var}\left(\gamma_{A,L}\right)=\sigma_{A,L}^2=\sigma_{A,R}^2\end{aligned}$$

ANALYSIS OF NOISE STRUCTURE BY VARIOUS NORMALIZATION METHODS

Operations are all performed on two-sided embryos, with nuclear positions pre-normalized to range between 0 and 1, with the peak Dl located at the position 0. See below for the details of the nuclear position analysis and the normalization of this position (section III).

Steps for amplitude normalization:

- For each embryo *i*, find the max of a moving average m_i
- For each embryo *i,* update Dl values by multiplying by $mean_i\ (m_i) / m_i$

Steps for width normalization:

- Create moving average using all nuclei
- Identify threshold t as half the max of the moving average
- For each embryo i, find the width w_i
    - Find leftmost ($Lindex_i$) and rightmost ($Rindex_i$) nuclei with Dl values > t
    - Use linear interpolation of 3 nuclei $Lindex_{i-1}$, $Lindex_i$, $Lindex_{i+1}$ to determine position (L_i) where profile crosses t. Repeat to find R_i
    - Set $w_i = L_i - R_i$
- For each embryo i, update nuclei position values
    - For nuclei with Dl values > t:
        - $pos = (pos - 0.5) * \text{mean}(w) / w_i + 0.5$
    - For nuclei on left with Dl values < t:
        - $\text{pos} = \text{pos} * (0.5 - \text{mean}(w)/2) / (0.5 - w_i/2)$
    - For nuclei on right with Dl values < t:
        - $\text{pos} = 1.0 - ((1.0 - \text{pos}) * (0.5 - \text{mean}(w)/2) / (0.5 - w_i/2))$

For amplitude & width normalization, amplitude steps are performed first.

NUCLEAR POSITION MEASUREMENTS

After assigning points on the circumference positions from 0 to 10,000, nuclei were assigned positions based on their centroid's closest point on the circumference. To ensure that there was no effect from this normalized measurement, we reanalyzed a data set by assigning nuclei positions based on an absolute distance around the circumference. For a comparable analysis, we then rescaled all embryo positions so that the average maximum position was 10,000. We used normalized positioning as

it is commonly used in other models and taking into account typical *D. melanogaster* embryos do not vary greatly in size around this embryonic age [70].

MATCHING THE NUCLEAR POSITIONS ON TWO SIDES OF DL GRADIENTS

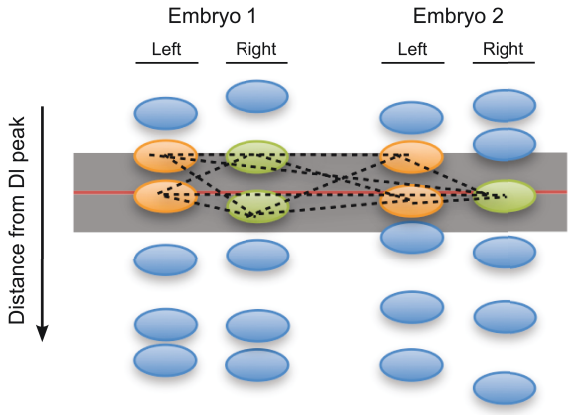

FIGURE 9: MATCHING NUCLEAR POSITIONS ON TWO SIDES OF DL GRADIENTS

Nuclei are paired in order to facilitate comparisons of gradients at equivalent positions on opposite sides.

Because nuclei positions vary across each embryo, one must decide which nuclei to match when separating sources of noise at a particular position**.** A linearized representation of nuclei in two embryos is shown to demonstrate how this is done. For a given position (indicated by the red line), a width of $1/60^{th}$ the embryo perimeter (approximately the width of a nucleus) is considered and nuclei whose centroids fall within the region (shown in grey) are selected. Nuclei shown in orange are included for the calculation of Var(L), and nuclei shown in green are included for the calculation of Var(R). Dashed lines indicate the pairs (all possible pairs between one left nuclei and one right nuclei) that are considered for the calculation of Cov(L,R).

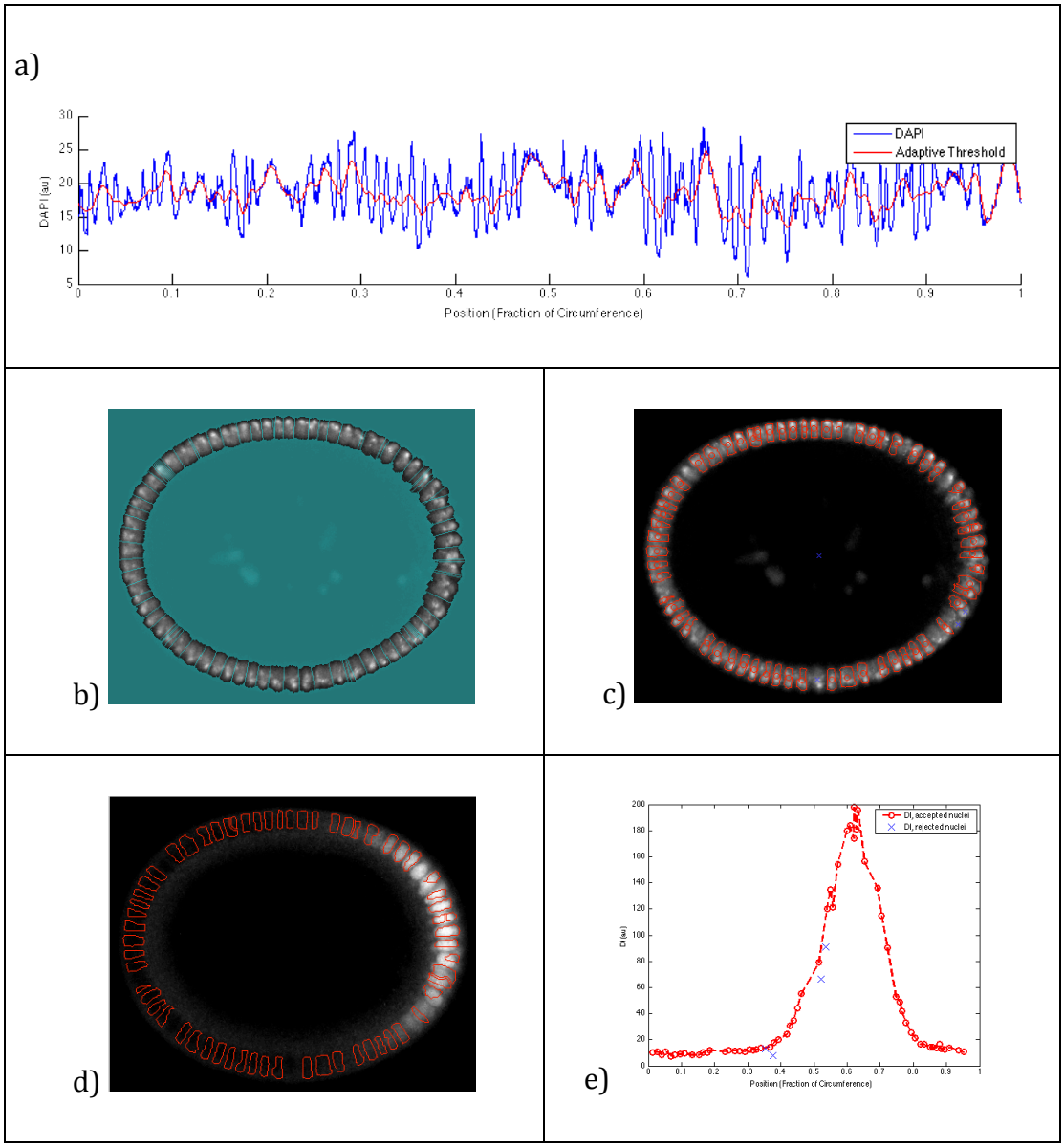

FIGURE 10: QUANTIFICATION OF THE DL SIGNALS

a) The perimeter and raw measurement of DAPI are identified using custom Matlab software as described in [69]. An adaptive threshold is then applied to find approximate nuclei borders. B) These borders are superimposed on the DAPI image. C) a watershed algorithm is applied to the modified DAPI image to identify the outlines of nuclei. D) After filtering erroneously identified nuclei based on unusual width, height, width/height ratio, and angle relative to the perimeter using manually selected values. E) Dl levels are reported as average pixel intensity within nuclei, and position is based on the point on the perimeter nearest the nuclei's centroid.

Chapter 4 CELL-CELL COMMUNICATION ENHANCES THE CAPACITY OF CELL ENSEMBLES TO SENSE SHALLOW GRADIENTS DURING MORPHOGENESIS

AUTHORS

David Ellison[1,4§], Andrew Mugler[2,3§], Matthew Brennan[1,4§], Sung Hoon Lee[4], Robert Huebner[5], Eliah Shamir[5], Laura A. Woo[1], Joseph Kim[1], Patrick Amar[6], Ilya Nemenman[2,7*], Andrew J. Ewald[5]*, Andre Levchenko[4]*

[1] Department of Biomedical Engineering, Johns Hopkins University, Baltimore, MD 21218, USA [2] Department of Physics, Emory University, Atlanta, GA 30322, USA [3] Department of Physics and Astronomy, Purdue University, West Lafayette, IN 47907, USA [4] Department of Biomedical Engineering and Yale Systems Biology Institute, Yale University, New Haven, CT 06520, USA [5] Center for Cell Dynamics, Johns Hopkins University, Baltimore, MD 21205, USA [6] Université Paris-Sud, 91405 ORSAY Cedex, France [7] Department of Biology, Emory University, Atlanta, GA 30322, USA

[§] These authors contributed equally to this work

ABSTRACT

Collective cell responses to exogenous cues depend on cell-cell interactions. In principle, these can result in enhanced sensitivity to weak and noisy stimuli. However, this has not yet been shown experimentally, and, little is known about how multicellular signal processing modulates single cell sensitivity to extracellular signaling inputs, including those guiding complex changes in the tissue form and function. Here we explored if cell-cell communication can enhance the ability of cell ensembles to sense and respond to weak gradients of chemotactic cues. Using a

combination of experiments with mammary epithelial cells and mathematical modeling, we find that multicellular sensing enables detection of and response to shallow Epidermal Growth Factor (EGF) gradients that are undetectable by single cells. However, the advantage of this type of gradient sensing is limited by the noisiness of the signaling relay, necessary to integrate spatially distributed ligand concentration information. We calculate the fundamental sensory limits imposed by this communication noise and combine them with the experimental data to estimate the effective size of multicellular sensory groups involved in gradient sensing. Functional experiments strongly implicated intercellular communication through gap junctions and calcium release from intracellular stores as mediators of collective gradient sensing. The resulting integrative analysis provides a framework for understanding the advantages and limitations of sensory information processing by relays of chemically coupled cells.

INTRODUCTION

Responses of isogenic cells to identical cues can display considerable variability. For instance, a population of cells will typically exhibit substantial variation in gradient sensitivity and migration trajectories within the same gradient of a diffusible guidance signal [71]. The variation in response could arise from the inherent diversity of cell responsiveness [8, 23, 72, 73], but it can be further exacerbated if the gradients of extracellular signals are shallow and noisy [27, 31, 74-77]. In fact, sensing shallow gradients can approach fundamental physical limits that define whether diffusive graded cues can bias cell migration [78, 79]. However, the

spatially biased response can improve and its uncertainty can be substantially reduced if individual cells are coupled while responding to molecular gradients [23, 80-87]. Strong cell-cell coupling might reduce the response noise by averaging individual responses of multiple cells [88-93]. It can also alleviate sensory noise by extending the spatial range of the sensing, thus increasing the potential for more precise detection of weak and noisy spatially graded inputs. Importantly, however, cell-cell communication involved in such collective sensing may be itself subject to noise, reducing the precision of the communicated signals and therefore the advantage gained from an augmented size of the sensory and the response units. The interplay between the increasing signal and accumulating communication noise associated with the multicellular sensing, and thus the limits of this multicellular sensing strategy, remain incompletely understood.

An example of collective cellular response is branching morphogenesis of the epithelial tissue in mammary glands [94-96]. The dynamic processes, whose coordinate regulation leads to formation, growth, and overall organization of branched epithelial structures, are still actively investigated [95]. Conveniently, the morphogenesis of mammary glands is recapitulated in organotypic mammary culture (organoids) [97-99], extensively used to model and explore various features of self- organization and development of epithelial tissues [100]. Epidermal Growth Factor (EGF) is an essential regulator of branching morphogenesis in mammary glands [101, 102]. It has also been identified as a critical chemo-attractant guiding the migration of breast epithelial cells in invasive cancer growth [103]. This property of EGF raises the possibility that it can serve as an endogenous chemo-

attractant guiding formation and extension of mammary epithelial branches, a possibility that has not yet been experimentally addressed.

Our data reveal that the capacity of mammary organoids embedded in collagen I to respond to shallow EGF gradients requires collective gradient sensing, mediated by intercellular chemical coupling though gap junctions. Surprisingly, the advantage of multicellular sensing is limited and is substantially lower than the theoretical predictions stemming from gradient sensing models that do not account for communication noise [74]. We build a theory of the multicellular sensing process, equivalent to the information-theoretic relay channel, which correctly predicts the accuracy of sensing as a function of the gradient magnitude, organoid size, and the background ligand concentration. The theory and the corresponding stochastic computational model trace the reduced sensing improvement to the unavoidable noise in the information relay used by cells to transmit their local sensory measurements to each other. This analysis allowed us to determine the approximate size of a collective, multicellular sensing unit enabling chemotropic branch formation and growth.

RESULTS

To study the response of multicellular mammary organoids to defined growth factor gradients, we developed and used mesoscopic fluidic devices. These devices permitted generation of highly controlled gradients of EGF, that were stable for a few days, within small slabs of collagen gels housing expanding organoids (see Figure 11A, Methods, and Supplementary Information). We found that organoids of

diverse sizes, ranging from 80 to 300 m (or about 200 to 500 cells), developed normally within the device, forming multiple branches in the presence of spatially uniform 2.5 nM of EGF. When monitored over 3 days, the branch formation in such uniformly distributed EGF displayed no directional bias (Figure 11C; Figure 18A). However, if EGF was added as a very shallow gradient of 0.5×10^{-3} nM/ m (equivalent to about 0.5×10^{-2} nM or as little as 0.2% concentration difference across a 10 m cell), branch formation displayed a significant directional bias (Figure 11D). The bias in formation of new branches remained the same when measured on each of the three consecutive days (Figure 20), suggesting that EGF gradient sensing is not a transient response, and that its angular precision neither improves nor decreases with time. The bias was robust to the choice of the bias measure, as six different measures all yielded values at least four standard errors above their respective null values (Figure 12; Figure 17; see also *SI*).

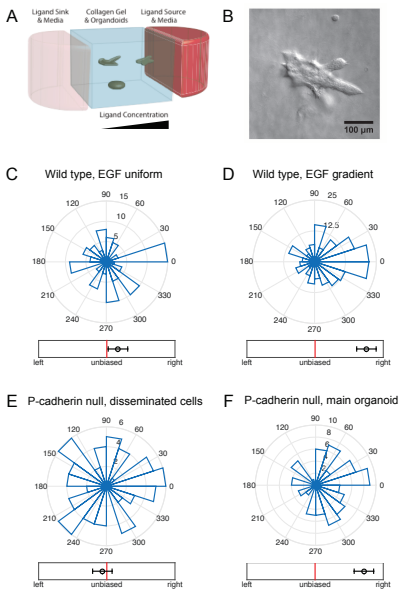

FIGURE 11: ORGANOID BRANCHING BUT NOT SINGLE CELL MIGRATION EXHIBITS BIASED DIRECTIONAL RESPONSE TO AN EGF LIGAND GRADIENT.

(A) A schematic of the mesofluidic device chamber, with high (red) and low (pink) EGF concentration reservoirs and organoids embedded in collagen gel exposed to the resulting EGF gradient (See Supplementary Materials for further information). (B) Example microscopy image of an organoid exposed to a 0.5 nM/mm EGF gradient, with preferential branch formation in the gradient direction (toward the right side of the field of view). (C-F) Angular histograms of (C) organoid branching directions in a uniform background of 2.5 nM EGF (3 biological replicates, 8 experimental replicates, total 110 organoids, total 460 branches); (D) organoid branching directions in a gradient of 0.5 nM/mm EGF (2 biological replicates, 2 experimental replicates, total 200 organoids, total 1283 branches); (E) in-gel migration directions of single cells separating from P-cadherin deficient organoids in a gradient of 0.5 nM/mm EGF (2 biological replicates, 6 experimental replicates, total 255 cells originating from 76 organoids); (F) organoid branching directions for the P- cadherin organoids in a gradient of 0.5 nM/mm EGF (2 biological replicates, 6 experimental replicates, total 79 organoids, total 394 branches). Whereas single cells do not exhibit biased movement, organoids exhibit biased branching. In (C), (D) and (F), branching direction is defined as the angle of the vector sum of the organoid's branches. The number of organoids branching in a specific direction is shown. In (E), cell migration direction is defined as the angle of the vector sum of the displacements of all cells originating from a given organoid. In (C-F), the circular axes measure the number of organoids with that branching direction, and left-right bias underneath each histogram is defined in Figure 12 (measure B).

In spite of the very shallow EGF gradient, it was still possible that the spatial bias in branching was a consequence of the gradient sensing by individual cells within the tips of the branches. To examine the sensitivity of single cells to these shallow gradients in the 3D geometry of collagen gels, we analyzed organoids derived from P-Cadherin knock out mice [104]. Consistent with our previous findings [105], the luminal epithelial core of the organoids derived from P-cadherin null mice remain intact within collagen I gels, but individual and small groups of myoepithelial cells disseminate into the surrounding gel, since P-cadherin is a specific mediator of myoepithelial cell-cell adhesion. These individual dissociated cells displayed extensive migration through the collagen matrix. Although in these experiments the organoids continued to display EGF gradient-guided directional branching responses similar to those of WT organoids, the dissociated cells migrated in a completely unbiased manner (Figure 11E, F; Figure 18B; Figure 19; see also *SI*). Cell motility and the distance traveled by single cells within the gels generally were the same as those observed in similar experiments performed in spatially homogenous 2.5 nM EGF distributions (data not shown). These results were corroborated by experiments in which dissociated single mammary epithelial cells isolated from WT mice or MTLn3-B1 cells were embedded in the same devices and subjected to the same experimental inputs (Figure 20). The results of these experiments suggested that, in spite of considerable motility, there was no evidence of chemotaxis by these cells, in response to EGF gradients that were capable of triggering biased chemotropic response in organoids. Overall, our results reveal that cell-cell coupling within organoids permits sensing of EGF gradients not detectable by single cells.

A

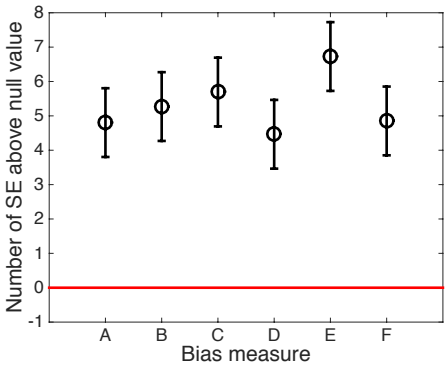

B

	Description	Null value	Measured value
A	vector sum of branches, projected in gradient direction	0 μm	52 ± 10 μm
B	whether A is positive (1) or negative (0)	0.5	0.68 ± 0.03
C	A, normalized by mean branch length	0	0.69 ± 0.12
D	fraction of branches pointing right	0.5	0.55 ± 0.01
E	fraction of east/west branches pointing west	0.5	0.61 ± 0.02
F	D, weighted by branch length	0.5	0.56 ± 0.01

FIGURE 12: ORGANOIDS BRANCHING IS SIGNIFICANTLY BIASED, REGARDLESS OF THE CHOICE OF THE BIAS MEASURE.

(A) Six bias measures are shown, as described in the table in panel (B) (the gradient points in the θ = 0 direction, such that 'right' means the up-gradient half of the plane cos θ > 0, "east" means the up-gradient quarter of the plane cos θ > cos π/4, and "west" means the down- gradient quarter of the plane cos θ < cos 3π/4). The table lists the null (unbiased) values for each measure, as well as the measured values from the data, averaged across all organoids, and with uncertainty given by the standard error (SE). All measured values are at least 4 standard errors above their respective null values. See Supplementary Materials for further analysis. Note that, visually, measure B, used throughout the text, seems less biased than the histograms in Figure 11; this is because the histograms only count the number of branches in specific directions, while the measure B additionally weighs each branch by its length

Can enhanced collective gradient sensing by multiple cells be explained by a quantitative theory, permitting experimental validation? The classic Berg-Purcell (BP) theory of concentration [106] and gradient [74, 78] detection can explain why a larger detector (in this case, an organoid) has a better sensitivity than a smaller one (a cell). Briefly, the mean number of ligand molecules in the volume of a detector of a linear size *A* is $\bar{\nu} \sim \bar{c}A^3$, where c is the concentration being determined, and overbar represents averaging. This number is Poisson distributed, so that the relative error in counting is $(\delta\nu/\bar{\nu})^2 = (\delta c/\bar{c})^2 = 1/\bar{\nu} \sim 1/(\bar{c}A^3)$. This bound can be

modified to include temporal integration of the ligand diffusing in and out of the receptor vicinity [107]. However, the organoids show steady branching and no improved directional sensitivity over the three days of experiments (Figure 21), so the sensing can be assumed to occur on time scales much shorter than the overall branching response, without long-time integration. Estimation of spatial gradients by a cell or a multicellular ensemble involves inference of the difference between (or comparison of) concentrations measured by different compartments of the detector [74, 75, 78] (branches grow too slowly for a temporal comparison strategy to be useful [108]). For a detector consisting of two such compartments, each of size $a \ll A$, the mean concentration in each compartment is $\bar{c}_{\pm} = \bar{c}_{1/2} \pm gA/2$, where $c_{1/2}$ is the concentration at the center of the detector, and g is the concentration gradient. For each of the compartments, the BP bound gives $(\delta c_{\pm}/\bar{c}_{\pm})^2 \sim 1/(\bar{c}_{\pm}a^3)$. Subtracting the two independently measured concentrations estimates the gradient, $g = (c_+ - c_-)/A$, which results in the signal-to- noise ratio (SNR, or inverse of the error):

$$\frac{1}{\mathrm{SNR}} \equiv \left(\frac{\delta g}{g}\right)^2 \approx \frac{\bar{c}_{1/2}}{a^3(Ag)^2}. \qquad [1]$$

Thus the sensing precision should improve without bound with the span of the gradient being measured (A), with the gradient strength (g), and with the volume over which molecules are counted (a^3). However, the precision should decrease with the background concentration ($\bar{c}_{1/2}$) because it is hard to measure small changes in a signaling molecule against a large background concentration of this molecule.[1] Note that Eq. [1] seems to predict an infinitely precise measurement when $\bar{c}_{1/2} \to 0$, and

there are no ligand molecules. This paradox is resolved by the simple observation that the background concentration of the signaling molecule and the organoid size are not independent: in a linear gradient, $\bar{c}_{1/2}$ is limited from below by $Ag/2$, and, generally, small $\bar{c}_{1/2}$ is only possible for a small organoid if the gradient is nonzero. In this *low concentration* limit of the BP theory, which is often the subject of analysis [74, 78], $Ag \sim \bar{c}_{1/2}$. Then Eq. [1] transforms to $\mathrm{SNR} \sim \bar{c}_{1/2} a^3$, and the SNR *increases* with $\bar{c}_{1/2}$. Overall, this interplay between the size and the concentration depends on $\bar{c}_{1/2}(A)$, which may take different forms depending on where organoids of different sizes are in the experimental device. Typically, the SNR has an inverted U-shape: it first grows with $\bar{c}_{1/2}$ because the span of the organoid increases, and then it drops because small differences of large concentrations must be estimated by a cell or a cell ensemble (Figure 22; also see *SI*). Interestingly, this decrease in gradient sensitivity does not require receptor saturation, as is commonly assumed [109]. Calculations that account for true receptor geometries of the sensor give results similar to Eq. [1] [74]. A critical prediction of this theory is that precision of gradient sensing (expressed as SNR) always increases with the organoid size *A.* We next contrasted this prediction with experimental data.

To examine whether the precision of gradient sensing increases with the organoid size, we examined the bias of response of differently sized organoids naturally formed in our assays. (Figure 13). To enable the comparison, we computed the fraction of organoids with $L_U > L_D$, where $L_U(L_D)$ is the sum of branch lengths (projected in the gradient direction) pointing up (down) the gradient (measure B in

Figure 12). The corresponding theoretical prediction can be inferred from the analysis of a one- dimensional array of *N* coupled cells subjected to a ligand gradient. In particular the experimentally determined difference between "up" and "down" pointing branch numbers can be compared with the theoretically predicted probability that the measured number of ligand molecules in the *N*'th cell is larger than in the first cell in the array, $\nu_N > \nu_1$. We take ν_n as Gaussian-distributed with mean $\bar{c}_n a^3$ and variance $\bar{c}_n a^3 + \eta^2$, where the first term accounts for the Poisson nature of the molecular counts, and η^2 represents the additional noise downstream of sensing, which can dominate the sensory noise, but is assumed to be unbiased (multiplicative noise was also considered, with similar effects, see Figure 23 and *SI*). We set the value of η^2 by equating the experimental and theoretical bias probabilities averaged over all organoid sizes and background concentrations observed in the experiments. Figure 13A demonstrates that bias increases roughly linearly with the gradient strength in both the experiments and the BP model. However, Figure 13B shows that the experimental bias saturates with organoid size, while the BP theory would predict an increase without bounds. Further, Figure 13C shows that the experimental bias is generally weaker than that predicted by the BP theory. These disagreements with experimental results suggest that a new theory of multicellular gradient detection is required.

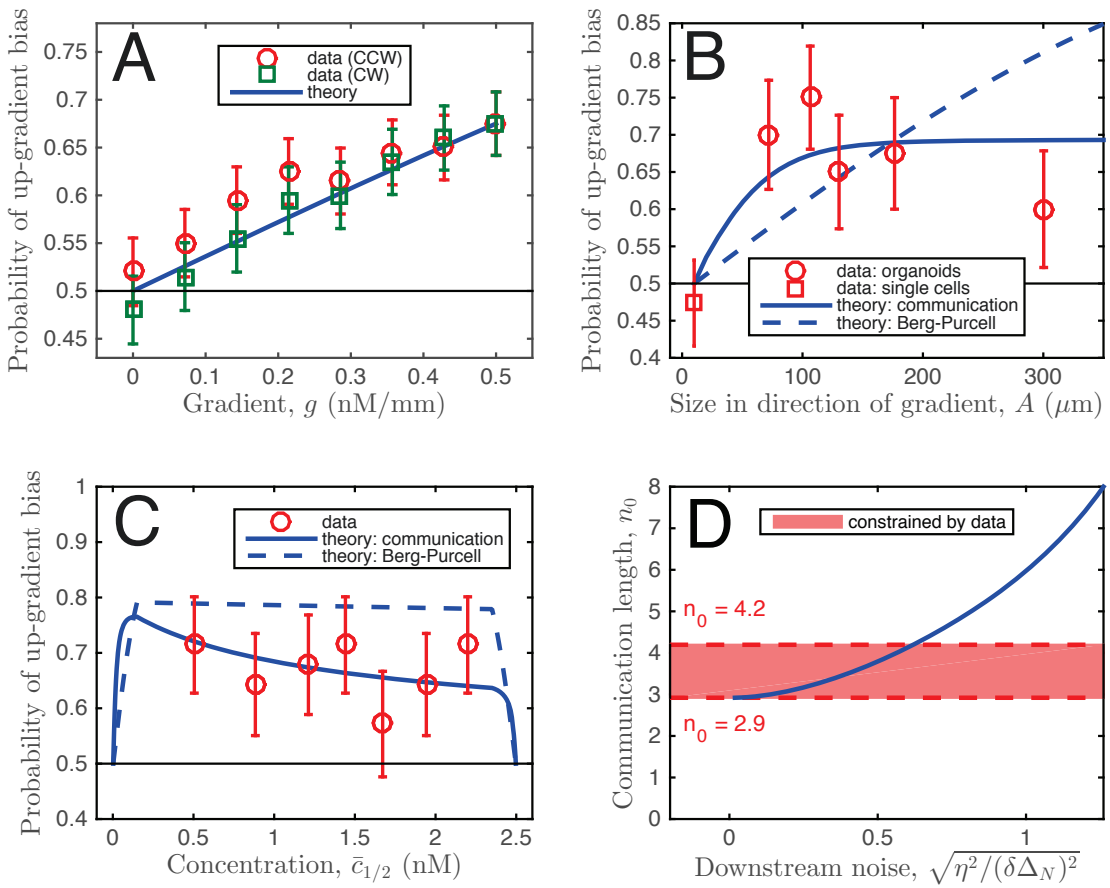

FIGURE 13: ORGANOID BRANCHING BIAS FOR DIFFERENT PARAMETERS: DATA SUPPORT THEORY OF COMMUNICATION-CONSTRAINED GRADIENT SENSING.

(A-B) Experimentally measured bias (denoted as "data") is plotted vs.: (A) EGF gradient strength, (B) organoid size, and (C) background EGF concentration. For the data, bias is measured as the fraction of organoids with $L_U > L_D$, where $L_U(L_D)$is the sum of branch lengths, projected in the gradient direction, pointing up (down) the gradient (measure B in Figure 12). Error bars are standard errors. In (A), gradient response is estimated for different branching response directions, with the response axis rotated by the angle θ, either clockwise (CW) or counterclockwise (CCW) with respect to the gradient directions, reducing the effective gradient by $\cos\theta$. In (B), the organoid body size is measured excluding branches, and the bias for single cell migration is measured as for organoid branches, but with cell displacement replacing branch length. In (C), stability of bias at large concentration shows absence of significant saturation effects. Theory: The bias is calculated as the probability that , where $\Delta_N(\Delta_1)$is the Gaussian-distributed concentration difference in the cell furthest up (down) the gradient, with mean and variance given by the model as described in the text. The classic Berg-Purcell (BP) theory predictions, which do not account for

communication, are equivalent to setting the communication length n_0 to infinity in the theory that accounts for the communication. The downstream noise η^2 is set by the data. In A, this leaves no free parameters, and in B and C, after assuming a cell size of a = 10 μm μ and taking the limit of large gain β/μ, this leaves only the communication length n_0. The curve for $n_0 = 3.5$ is shown in comparison to the BP curve to illustrate the effect of communication. In (B) and (C), the theoretical curves are obtained by averaging uniformly over the ranges of organoid size or midpoint concentration seen in the experiments (10-600 μm, 0.22-2.47 nM), except where prohibited by geometry, as in Figure 22. Since background concentration and size of the organoids are not independent, this results in the nonmonotonic dependence in (C). Specifically, the nonmonotonicity comes from the noisy comparison of large, similar concentrations, as explained in the text, and also because organoids with large midpoint concentration are at the edge of the device and cannot be large. (D) Communication length n_0 is constrained by the data. Minimum $n_0 \geq 2.9$ is determined by the fact that downstream processes can only add noise, not remove it ($\eta^2 \geq 0$). Maximum is determined by the condition that data and theory in B agree sufficiently that χ^2/(degree of freedom) < 1.

To develop the new theory, we note that, by assuming that information, collected by different parts of a spatially extended detector, can be integrated in an essentially error free fashion, the BP approach neglects a major complication: the communication noise. Indeed, to contrast spatially distributed inputs, e.g., the local EGF concentration, the information collected in different parts of a coupled multi-cellular ensemble must be communicated over large distances by means of noisy, molecular diffusion and transport processes. The unavoidable communication errors set new, unknown limits on the highest accuracy of sensing. From this perspective, the BP analysis accounts for the *extrinsic* noise of the ligand concentration, but not for the *intrinsic* noise [8, 9] of multi-cellular communication. To study the communication noise effects, we again approximated an organoid by a one-dimensional chain of *N* cells, each of size *a*, for a total length of *A*=*Na* parallel to the gradient direction. The observed independence of the response bias of the background EGF concentration (Figure 13C) supports an adaptive model of sensing.

We chose a minimal adaptive model allowing for chemical diffusive communication, based on the principle of local excitation and global inhibition (LEGI) [110-112]. In the *n*th cell, both a local and a global molecular messenger species are assumed to be produced in proportion to the local external EGF concentration c_n at a rate β, and are degraded at a rate μ. Whereas the local messenger species is confined to each cell, the global messenger species is exchanged between neighboring cells at a rate γ, which provides an intrinsically noisy communication. The local messenger then excites a downstream species, while the global messenger inhibits it. In the limit of shallow gradients, the excitation level reports the difference Δ_n between local and global species concentrations (see *SI*). The difference $\Delta_{N,1}$ in the edge cells provide the sensory readout: positive/negative Δ shows that the local concentration at the edge is above/below the average, and hence the cell is up/down the gradient. Note that an individual cell within this multi-cellular version of the LEGI model cannot detect a gradient, as the readout will always be zero within statistical fluctuations.

In our analysis, we again note the absence of temporal integration of EGF gradients (Figure 21; see also the extension of our analysis to the temporal integration case in Ref. [107]). Further, since there is no evidence for receptor saturation at high concentration (Figure 13C), we confine ourselves to the linear response regime for theoretical studies. These assumptions allow us to calculate the limit of the sensory precision of the gradient detection, as a function of organoid size *N* and the background concentration (see *SI* and Figure 22). We find that precision initially grows with *N*, then saturates at a maximal value (Figure 22C). This is in contrast to

the BP estimate, Eq. [1], which predicts that precision grows indefinitely with *N*. In our model we expect precision to be the highest in the limits of a large organoid ($N \gg 1$), fast cell-to-cell communication ($\gamma/\mu \gg 1$), and large local and global messenger species concentrations ($\beta/\mu \gg 1$). In these limits the saturating value of the sensory error takes the simplified form (Eq. [46] in *SI*)*:*

$$\frac{1}{\mathrm{SNR}} = \left(\frac{\delta\Delta_N}{\bar{\Delta}_N}\right)^2 = \frac{\bar{c}_N}{a^3(n_0 a g)^2} = \frac{\bar{c}_{1/2} + gaN/2}{a^3(n_0 a g)^2}, \qquad [2]$$

where $n_0 = \sqrt{\gamma/\mu}$. Comparing Eq. [2] to the BP estimate, Eq. [1], we see that even when communication noise is accounted for, the organoid can achieve the noise-free bound, but with an *effective size* of $A = n_0 a$ instead of the actual size $A = Na$. Thus n_0, which grows with the communication rate γ, sets the length scale of the effective sensory unit within the organoid: it is the number of neighbors with which a cell can reliably communicate before the information becomes degraded by the noise. Beyond $N \sim n_0$, a larger organoid is predicted to achieve no further benefit to its sensory precision. Additionally, because of this finite communication length scale, the sensory precision is predicted to depend on the concentration at the edge cell(s), rather than in the middle of the organoid. Thus the interplay between the concentration and the organoid size is also very different compared to the predictions of the standard BP theory.

We first tested the new theory that accounts for communication by simulating the multi-cellular, LEGI- based sensing with a spatially extended Gillespie algorithm (see *SI* for details). This analysis allowed us to explore the non-linear (Michaelis-Menten

type) biochemical reaction regime. We verified that our theoretical predictions were fully consistent with this stochastic model in the linear regime, and were still qualitatively valid when the dependence of the local and the global signaling reactions on the input was allowed to gradually saturate (Figure 14). In particular, under all assumptions, the advantage of increasing detector rapidly reached a maximum value. This maximum SNR value, however, gradually decreased with increasing saturation, suggesting predominant effects of decreasing sensitivity of saturating chemical reactions to the differences in the input values.

We then compared the predictions of our new theory of multicellular gradient sensing to the experimental measurements. To do that, we calculated the probability that the gradient indeed biases the branching response, i.e., that $\Delta_N > \Delta_1$, where Δ_n was assumed in the theory to be a Gaussian- distributed variable with the mean $\bar{\Delta}_n$ and variance $(\delta\Delta_n)^2 + \eta^2$ (the case of the multiplicative noise is treated in the SI and Figure 23). The first term in the variance is calculated in the *SI*, and the second reflects the added noise downstream of gradient sensing, set by the average organoid bias, identical to the one found in the BP theory above. Figure 13A-C demonstrates the excellent agreement between experiment and theory that accounts for the communication noise, suggesting that the new theory is a much better explanation of the data than the BP analysis.

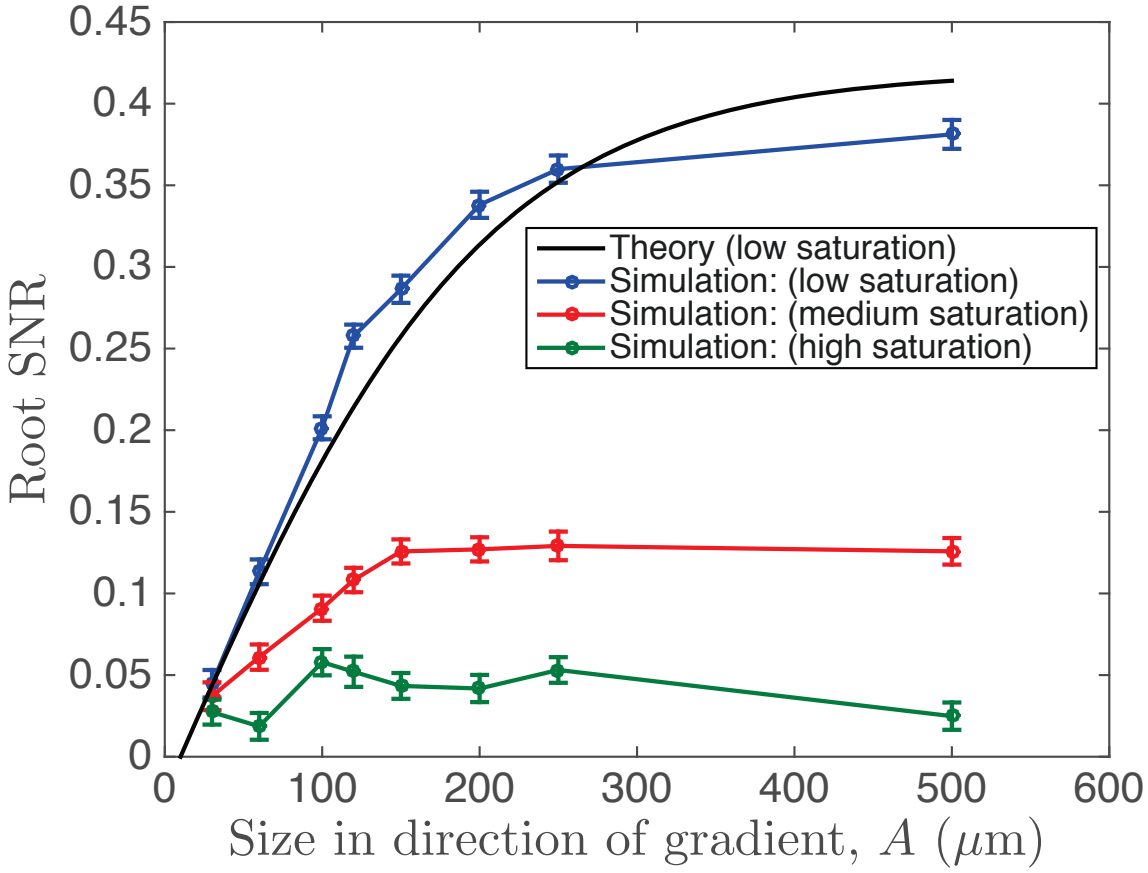

FIGURE 14: SATURATION OF SIGNALING RESPONSES REDUCES THE MAXIMUM SNR IN THE SIMULATION OF MULTICELLULAR GRADIENT SENSING.

To investigate effects of signaling saturation, we simulated a multicellular stochastic LEGI model using a spatially resolved implementation of the stochastic simulation algorithm (see SI) and measured the simulated organoid bias at different saturation levels. The figure shows the square root of the SNR (mean response squared over its variance), where for the response we take the deviation of the species activated by the local and suppressed by the global messenger from its mean value. This is the closest equivalent to Δ_N*, and to the bias measure in Figure 13 and Figure 22. For the theory and the simulations, we set molecules per cell volume per cell diameter,* $n_0 = \sqrt{\gamma/\mu} = 10$ *cells,* $\bar{c}_N = 1000$ *molecules per cell volume. We contrasted the theory and the simulations by matching the low saturation curves for small organoid sizes. The effects of saturation in activation/suppression of the response by the messengers result in earlier saturation of the SNR curves, as expected.*

The experimental data in Figure 13B place constraints on the possible range of values of the size of the effective multi-cellular sensing unit, n_0. The requirement that $\eta^2 \geq 0$ (downstream processes only increase noise, they do not decrease it) places the lower bound $n_0 \geq 2.9$ (Figure 13D). Roughly speaking, the edge cell must communicate with at least three neighbors if the inability of the observed bias to reach 1 was due *entirely* to sensory noise, with no additional noise downstream. Further, the requirement that the model agree with the data within error bars in Figure 13B also places the upper bound $n_0 \leq 4.2$ (similar limits come from the multiplicative model, Figure 23). That is, a functional sensing unit of four cells or less is required to explain why all organoids, which range in width from approximately 8 to 30 cells, display roughly the same bias, independent of their size. Thus Figure 13 demonstrates that cells receive reliable information from only a few nearby cells, and this number is tightly bounded. The tightness of the bound implies that the noise downstream of the sensing process is relatively small. Crucially, in our theory, a cell not communicating with the neighbors cannot detect a gradient, and a nonzero value of n_0 is *qualitatively* different from $n_0 = 0$. We thus tested if gradient sensing would be altered if cell-cell communication was prevented in the organoids.

A central prediction of the theoretical analysis is that preventing cell-cell communication can lead to a complete loss of sensing of shallow gradients. One simple way cell-cell communication can occur in epithelial layers is by means of gap junctions. We therefore explored the effect of disrupting the gap junction communication using four distinct inhibitors: 50 nM Endothelin-1, 50 M flufenamic

acid, 0.5 mM octanol and M carbenoxolone [113]. Although the mode of inhibition was different for these distinct compounds, application of each one of them resulted in a complete loss of directional bias in response, while the branching itself was present, and was similar to that without gap junction perturbation in spatially uniform EGF concentrations (Figure 15A, Figure 24). Crucially, this result also confirms that communication over the effective sensory unit is due to intracellular chemical diffusion, rather than through the extracellular medium or due to a mechanical coupling. The likely candidates for gap junction mediated cell-cell coupling are calcium or inositol trisphosphate (IP3), both of which are second messengers that can control intracellular Ca release. EGF is known to stimulate Ca signaling [114] at least in part through stimulation of IP3 synthesis, thus providing a source of these intracellular messengers.

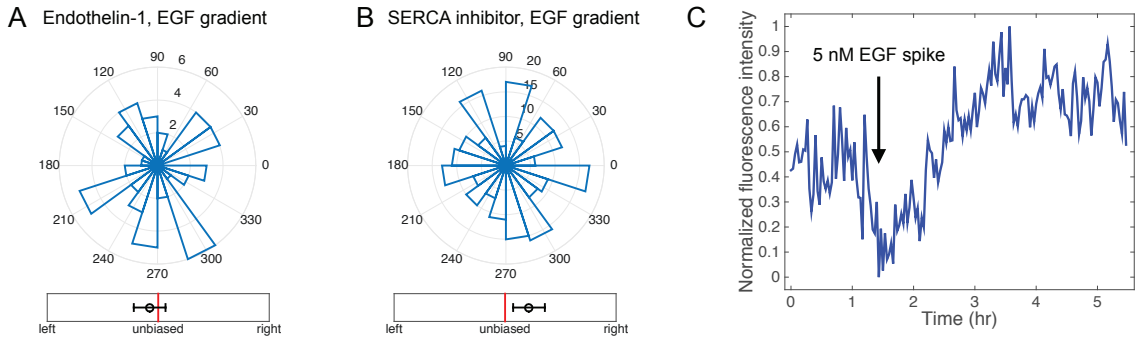

FIGURE 15: CELL-TO-CELL COMMUNICATION PROCEEDS THROUGH GAP JUNCTIONS AND INVOLVES CALCIUM IONS.

Directional histograms and biases (measure B in Figure 12) of organoids in 0.5 nM/mm EGF gradient with (A) 50 nM of a gap junction blocker Endothelin-1 added, (2 biological replicates, 3 experimental replicates, total 54 organoids, total 177 branches), and (B) with 100 nM of thapsigargin, a SERCA inhibitor, depleting internal calcium stores (2 biological replicates, 2 experimental replicates, total 214 organoids, total 1071 branches). Both (A) and (B) show absence of directional response by

multicellular organoids in these conditions. (C) 2.5nM EGF is added to the device and the total Ca signaling is measured in organoids obtained from GCaMP4, under the control of the CAG promoter (see evidence for cell-cell coupling within these organoids in SI).

To examine Ca signaling more directly, we used organoids obtained from transgenic mice, expressing genetically encoded Ca reporter GCaMP4, under the control of the CAG promoter [115]. We confirmed that addition of 2.5 nM EGF to the medium indeed triggered a pulse of calcium signaling in a typical organoid (Figure 15C). Furthermore, the Ca activity throughout the branching processes was coordinated, releasing calcium nearly simultaneously in cells at the tips of growing branches, suggesting cell-cell communication leading to Ca releases (see *SI*, Figure 25). To deplete intracellular Ca stores and thus potentially disrupt the effect of chemical cell-cell coupling, we treated the organoids with sarco/endoplasmic reticulum Ca2+-ATPase (SERCA) inhibitor thapsigargin. This treatment indeed was sufficient to disrupt EGF gradient sensing in the treated organoids (Figure 15B and Figure 18D). Surprisingly, SERCA inhibition also enhanced the branching elongation: the average length of a branch increased from 74 ± 1 m for WT organoids to 201 ± 3 m with SERCA blocking; the organoids appear to be almost entirely composed of branches after 3 days under these conditions. This result suggested that gap junction-mediated exchange of a molecular regulator that can trigger intracellular calcium release may have a negative effect on the local branching response, consistent with the assumed negative role of the diffusive messenger postulated in the LEGI model. We finally note that small molecules exchanged though gap junctions (e.g., IP3 or calcium ions) would be a natural choice for the cell-cell coupling intercellular messenger, since their smaller size and larger diffusion coefficient (compared to

peptides) allow for a larger , which, in turn, increases the size of the effective sensory unit n_0 and improves the sensing accuracy.

DISCUSSION

Morphogenesis and growth of complex tissues is orchestrated by diverse chemical and mechanical cues. These cues not only specify patterning of developing tissues but also direct tissue growth and expansion. However, we still lack details of how these collective, multi-cellular processes are controlled by spatial gradients of extracellular ligand molecules. Here we used mathematical modeling, computational simulations, and experimentation in a novel gradient generating device to study the directional guidance of branch formation and extension in a model of mammary tissue morphogenesis. Our data revealed that multicellular constructs undergo directionally biased migration in shallow gradients of EGF that are undetectable to single cells. Further, our analysis suggests that cell-cell communication through gap junctions underlies the increased gradient sensitivity, allowing the cell ensembles to expand the range of EGF concentrations they can sense within the gradient, and thus enhance the overall guidance signal. Increasing evidence suggests that collective sensing of environmental signals, particularly if accompanied by secretion of a common signal that enables averaging of variable and noisy signaling in individual cells, can help improve reliability of signaling, cell fate choices, and behavioral actions. Examples are abundant in coordinated pathogen actions or immune responses [75, 103-108, 116]. Similarly, individual sensing and collective decision-making in morphogenesis and animal group behaviors have been shown to amplify

weak signals observed by individual agents and to develop coherent, long-range patterns [90, 91, 117, 118]. In contrast to 'all-to-all' signaling or response communication cases, here we focused on the case of sequential communication of a signal between the sensing units, in a relay fashion, which can enhance the sensing precision by enhancing the effective input itself. Critically, this communication mechanism, mediated by diffusive coupling through gap junctions, can be seen as an information-theoretic relay channel [22, 119], see Figure 16. The theoretical analysis we present here is thus one of the first departures from the simple point-to-point information-processing paradigm in systems biology. In fact, our calculations of reliability of multicellular signaling, presented in this paper and in [107], are equivalent to calculating channel capacities of various Gaussian relay channels.

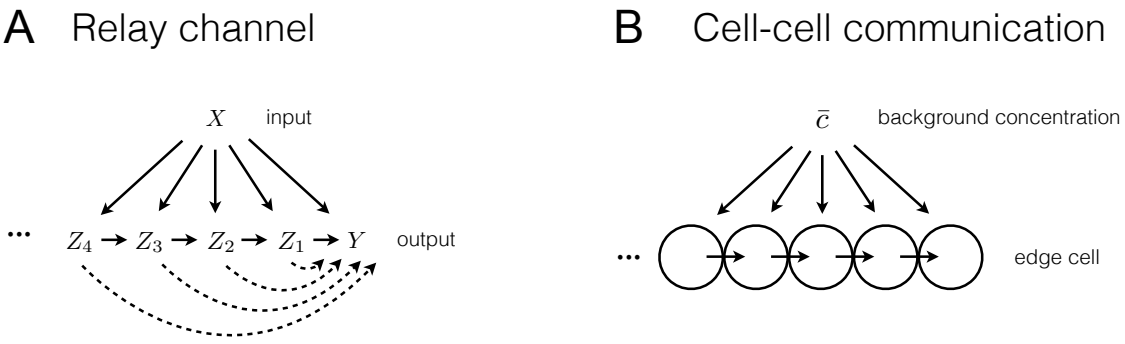

FIGURE 16: MULTICELLULAR GRADIENT SENSING IS AN EXAMPLE OF A RELAY CHANNEL.

(A) A diagram of an information-theoretic relay channel. Differently scrambled versions of the input signal are communicated to the output, but also to the intermediate relay units. In their turn, the intermediate units relay the information further along the chain, and ultimately to the output unit. (B) Interpretation of gradient sensing as a relay channel. The local concentration, which is a biased and noisy version of the background concentration, is measured by every cell, and then relayed to the edge cell using the diffusive messenger to produce an estimate of the background concentration.

The key consequence of the relay communication mechanism is that it is subject to a gradual buildup of communication noise, mitigating the gain from the signal increase, and providing a fundamental limit on effectiveness of such collective sensing responses. This result runs counter to the prevailing intuition that sensing accuracy should increase without bound with the system size [12], for multicellular systems in development [93] and also for other multi-agent sensory systems. These intuitive expectations are flawed precisely because they fail to take into account the importance of communication uncertainty, which provides fundamental limits on the gains resulting from multicellular sensing. Our integrated analysis reveals that this multicellular sensing strategy in growing mammary branches is indeed limited by the noisy cell-cell communication. Importantly, we were able to combine theory and experiments to estimate these limits for EGF gradient response of mammary branching and found them to be much tighter than those that assume that all of the spatially distributed information is immediately actionable: growth of the branch beyond the size of the maximum effective multicellular sensing unit does not improve the sensing accuracy. We estimate that the sensing unit is approximately 3-4 cell lengths, a size that is consistent with the number of cell layers in small end buds of a growing mammary duct [120] (see also Supp. Movie 1). Some large end buds in vivo contain significantly more cell layers and our analysis suggests that these additional cells may be primarily involved in other functions, such as proliferation and differentiation, and not gradient sensing. The narrow bounds on the number of interacting cells also suggest that the "actuation" noise downstream of sensing is minimal, paralleling related findings in the nervous system [121].

Interestingly, the theoretical analysis predicted that the sensory unit size is specified by a simple formula describing the typical distance traveled by a diffusing messenger molecule before it degrades or is inactivated, consistent with simpler estimates of the molecular communication reach [122]. Our analysis also provided a new way to interpret the dependence between the background ligand concentration and gradient sensing – saturation of receptors is not needed to explain the often-observed decrease in the sensory precision at high concentration [78, 79, 109]. Rather, the loss of precision is ascribed to increasing noise to signal ratio, stemming from the need to compare large, noisy concentrations. Similar limits might exist in any biological systems with spatially distributed sensing of spatially graded signals, including single cells or multi-nuclear syncytia.

Our results suggest that the intercellular communication underlying multicellular sensing in growing mammary tissue is mediated by calcium signaling events, as depletion of internal stores by a SERCA inhibitor both enhanced the branch formation and inhibited gradient detection. Thus release of calcium from internal stores is consistent with a negative or limiting effect on the local branch formation or extension. The release can be controlled by either IP3 or calcium itself, both of which can diffuse through gap junctions. Therefore, the inhibitory diffusive signal postulated by the LEGI models of gradient sensing may rely on the ultimate release of calcium from internal stories, as also suggested by our imaging of calcium with the genetically encoded probe. This role of calcium is consistent with its enhancement of retraction of the leading front in migrating cells [123]. Consistent

with the LEGI model, gradient sensing was persistent in time and exhibited very low sensitivity to the local background EGF concentration. The use of the LEGI model in our analysis, both in mathematical modeling and in spatially distributed Gillespie simulations, also showed results quantitatively consistent with the experiments, suggesting that this model was appropriate for describing the diffusively coupled collective EGF sensing.

Overall, we conclude that collective gradient sensing suggested for many natural developmental processes [124], as well as for pathological invasive tissue expansion [103], is an effective strategy, which, though subject to important limitations, can help explain the observed differences in the single cell and multicellular chemotactic responses. Importantly, the experimentally validated theory proposed in our analysis provides a way to assess the potential role of inter-cellular communication in other settings, including invasive tumor growth, pointing to the specific parameters that can be altered to disrupt this process or make it less efficient.

Materials and Methods

Experimental device.

Custom PDMS devices were developed using stereolithography, yielding culture area approximately 5mm wide, 10mm long and 1mm tall (see Figure 11B). The sides of the device are open wells that allow the use of standard pipettes to change media and six replicates of the entire device is contained within a standard six-well plate. Before use, the center cell culture area is filled. This action is assisted by the hexagonal pillars, which are used to trap the liquid 3D ECM and organoid mixture

within the cell culture area before the 3D ECM can harden [125]. Once the 3D ECM matrix of choice has hardened, the open wells can be filled as previously mentioned. Both *in silico* and *in vivo* (see *SI* and Figure 26) tests demonstrate a stable linear EGF gradient across the cell culture area for approximately three days, after which the media can be replenished as needed. Various compounds were added to collagen gel at final concentrations, as indicated, along with the organoids.

STEREOLITHOGRAPHY & PDMS CASTING.

Using the 3D rendering software SolidWorks (Dassault Systems), we drew the final mold for the PDMS devices. The design was electronically transmitted to FineLine Prototyping (Raleigh, NC) where it was rendered using high-resolution ProtoTherm 12120 as the material with a natural finish. Proprietary settings were used to accurately render the pillars. In two to three days the mold was shipped and after its arrival we mixed PDMS monomer to curing agent in a 10:1 ratio (Momentive RTV615). After mixing, the liquid PDMS was poured into the mold and a homemade press was used to keep the top surface flat. This press from bottom to top consisted of a steel plate, paper towel, piece of a clear transparency film, the mold with PDMS, another piece of a transparency, paper towel, piece of rubber, and an another steel plate. The entire assembly was placed in the oven at 80°C and baked overnight. The devices were then washed, cut, and placed on top of 22x22mm coverslips (72204-01, Electron Microscopy Sciences). Six devices where then placed inside an autoclave bag and sterilized. When needed, the bag was opened in a sterile environment and the devices were filled and placed inside a 6-well plate.

Device preparation for time-lapse imaging

In order to allow for real-time imaging, the devices were fabricated as described above, and were then cut from the PDMS using a 16mm sharp leather punch to create a circular device. The device was sterilized with ethanol and then plasma treated before being bonded directly to the bottom of a glass-bottomed 6-well plate with a 20mm hole (LiveAssay).

Collagen preparation

Rat-tail Collagen (354236, BD Biosciences) was pH balanced using 1M NaOH (S2770, Sigma) mixed to a final concentration of 3mg/mL with 10x DMEM (D2429, Sigma). This mixture sat in an ice block in aliquots of no more than 1.5mL until fibers formed, typically approximately 75 min (described in detail in Ref. [99]). Cells were then mixed in at 2.5 organoids/mL and a 100 L pipet tip was used to draw 75 L of the suspension. The pipette was inserted into the pre-punched hole and the suspension was gently injected into the device. The device was placed on a heat block for no more than 10 min before the side wells were filled with solution. The lid was replaced on the 6-well plate and the whole assembly was plated inside the incubator at 37°C with 5% CO2.

Confocal Microscopy

Confocal imaging was performed as previously reported [98, 126]. Briefly, imaging was done with a Solamere Technology Group spinning disk confocal microscope, using a 40× C-Apochromat objective lens (Zeiss Microimaging). Both fixed and time-lapse images were acquired using a customized combination of Manager

(https://www.micro-manager.org) and Piper (Stanford Photonics). Thereafter image stacking and adjustments were done with Imaris (Bitplane) in order to maximize clarity, but these adjustments were always done on the entire image.

DIC Microscopy

Phase contrast images were taken with an Axio Observer DIC inverted microscope (Carl Zeiss, Inc) using AxioVision Software (Carl Zeiss, Inc). All image processing was either done with Adobe Photoshop CS 6.0 (Adobe) or Fiji (GPL v.2) for clarity, but always done on the entire image.

Image Quantification

A custom Fiji program was written to measure the angle and length of the resulting branches. Additionally this program allows the user to draw a freehand outline around the body and/or the branch and body of the whole organoid. From these outlines area, a fit ellipse, and a Feret diameter were computed along with related statistics. After all measurements were made, a custom MatLab (MatWorks, Inc) program was written to create the graphs.

Primary mammary organoid isolation

Cultures are prepared as previously described [99]. Mammary glands are minced and tissue is shaken for 30 min at 37°C in a 50 ml collagenase/trypsin solution in DMEM/F12 (GIBCO-BRL), 0.1 g trypsin (GIBCO-BRL), 0.1 g collagenase (Sigma C5138), 5 ml fetal calf serum, 250 l of 1 g/ml insulin, and 50 l of 50 g/ml gentamicin (all UCSF Cell Culture Facility). The collagenase solution is centrifuged at 1500 rpm for 10 min, dispersed through 10 ml DMEM/F12, centrifuged at 1500 rpm

for 10 min, and then resuspended in 4 ml DMEM/F12 + 40 l DNase (2U/ l) (Sigma). The DNase solution is shaken by hand for 2–5 min, then centrifuged at 1500 rpm for 10 min. Organoids are separated from single cells through four differential centrifugations (pulse to 1500 rpm in 10 ml DMEM/F12). The final pellet is resuspended in the desired amount of Growth Factor Reduced collagen.

MULTICELLULAR GRADIENT SENSING MODEL

Theoretical results are derived using a stochastic dynamical model of multicellular sensing and communication. The model includes Langevin-type noise terms corresponding to ligand number fluctuations, stochastic production and degradation of internal messenger molecules, and exchange of messenger molecules between neighboring cells in a one- dimensional chain. The model is linearized around the steady state. The mean and instantaneous variance of the readout variable N are obtained by Fourier transforming and integrating the power spectra over all frequencies. This leads to an expression in terms of the matrix of exchange reactions, whose inverse (the "communication kernel") we solve for analytically and approximate in the appropriate limits to obtain Eq. [2]. See *SI* for more information.

STATISTICAL ANALYSIS

Angular histograms (e.g., Figure 11C-F) plot the distribution of branching directions over all organoids. For each organoid, the branching direction is defined as the angle of the vector sum of its branches. A branch vector extends from the organoid body (defined by the fitted ellipse) to the tip of the branch. For single cell movement (Figure 17E), the definitions are the same, except that branch vector is replaced by

the displacement vector, from where the cell broke away from the organoid, to where the cell is observed in the image. The breakaway point is taken to be the nearest branch tip. Data contained in the angular histograms are reduced to a single bias measure in one of six ways, as described in Figure 12**.** Measure B is also shown in Figure 11, Figure 13, and Figure 14. See *SI* for comparison of the bias measures.

SUPPLEMENTARY INFORMATION

1. MEASURING BIAS IN ORGANOID BRANCHING

To ensure that our determination of response bias is robust to our analysis technique, we measured bias in several different ways (Figure 17), using data for wild-type organoids in the presence of an EGF gradient (Figure 11D). Figure 17A shows a histogram of the angles of all branches, irrespective of which organoid the branch comes from. Figure 17B shows a histogram of all organoid angles, where organoid angle is defined as the angle of the vector sum of all branches coming from a given organoid. Thus Figure 17A is a branch-based histogram, whereas Figure 17B is an organoid-based histogram. Figure 17A and B demonstrate that both a branch-based and an organoid-based analysis indicate that the response of wild-type organoids is significantly biased in the gradient direction. Figure 17C shows the six different bias measures defined in Figure 12, applied to both the branch-based and the organoid-based data. In all cases, the response is significantly biased with respect to the null value. This demonstrates that the determination of bias is robust to the choice of bias measure.

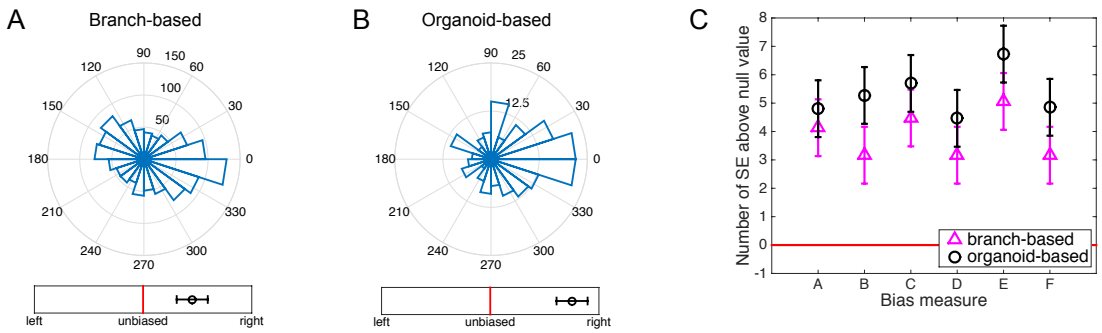

FIGURE 17: BIAS DETERMINATION IS ROBUST TO CHOICE OF MEASURE.

All bias measures used in this study are shown, here for wild-type organoids in a 0.5 nM/mm EGF gradient. (A) Histogram of branch angles, irrespective of which organoid the branch comes from. (B) Histogram of organoid angles, defined as the angle of the vector sum of all branches coming from a given organoid. (C) Six bias measures, defined in Figure 12. Measure B is shown underneath panels A and B. In all panels A-C, the response is significantly biased with respect to its standard error (SE).

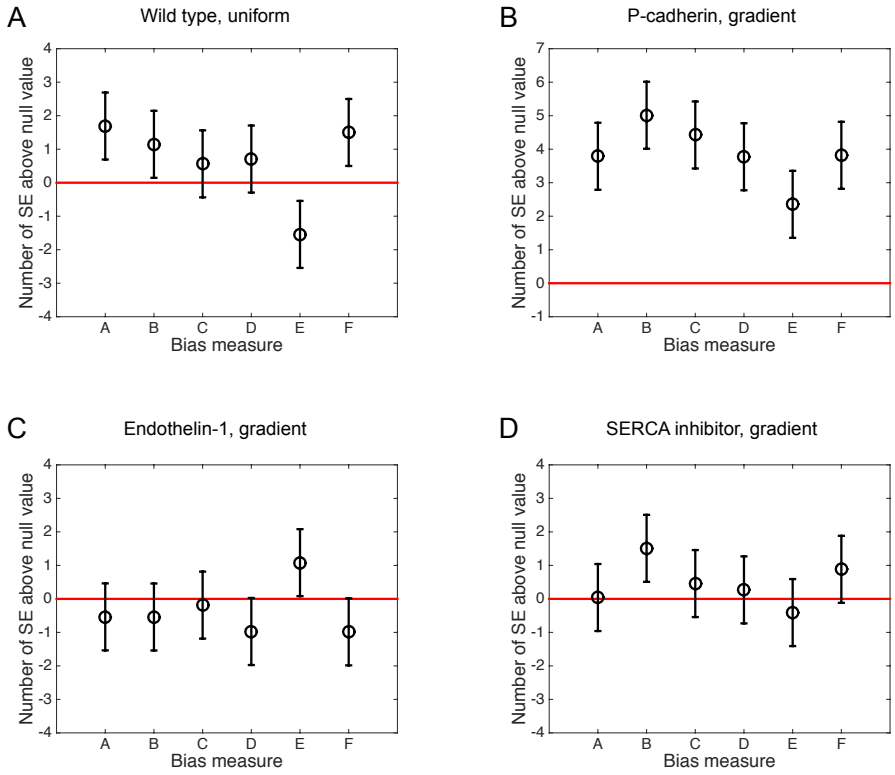

FIGURE 18: ROBUSTNESS TO BIAS MEASURE PERSISTS IN DIFFERENT EXPERIMENTAL CONDITIONS.

The six bias measures are shown for (A) wild-type organoids in a uniform 2.5 nM EGF background concentration, (B) organoids with P-cadherin knockout in a 0.5 nM/mm EGF gradient, (C) organoids exposed to Endothelin-1 in a 0.5 nM/mm gradient, and (D) organoids with SERCA inhibitor in a 0.5 nM/mm EGF gradient (Figs. 1C and F and 4A and B of the main text). In all cases, the response is either significantly biased (B), or not significantly biased (A, C, D), irrespective of choice of bias measure.

In general, we find that it does not matter whether we use a branch- or organoid-based measure to determine bias. Therefore, we focus on organoid-based measures for most of the study, since this metric retains the information about the organoids producing the branches, rather than considering branches as completely independent entities. Moreover, in general we also find that the determination of bias is robust to the choice of bias measure (see Figure 18 and Figure 19 below). Therefore we focus on measure B for most of the study, since it is easy to interpret

and to compare with the theory: it is the probability that the vector sum of an organoid's branches points up the gradient, not down the gradient.

Figure 18 shows the six bias measures for each of the other experimental conditions considered in the main text. We see in all cases that the presence or absence of bias is robust to the choice of measure.

2. Measuring bias in single-cell movement

To ensure that our determination of bias in single-cell movement is also robust to the analysis technique, we subject the single-cell data to a similar multitude of bias measures. For single cells, the analog of a "branch" is the distance the cell migrates over time. Therefore, if more cells migrate to the right than to the left, then the cells exhibit a biased response. Figure 19 shows the same bias measures computed for organoid branching, but now for single cell migration distances, for the experiment in which the P-cadherin mutation promotes shedding of single cells from the organoid. We compute the bias measures both (i) averaged over all cells, irrespective of the organoid from which cells are shed (Figure 19A, analogous to the "branch-based" measures in Figure 17C) and (ii) averaged per organoid, by accounting for the organoid from which the cells are shed (Figure 19B, analogous to the "organoid-based" measures in Figure 11C). In both cases, we see that the single-cell movement is not significantly biased, and that the absence of bias is robust to

the choice of measure.

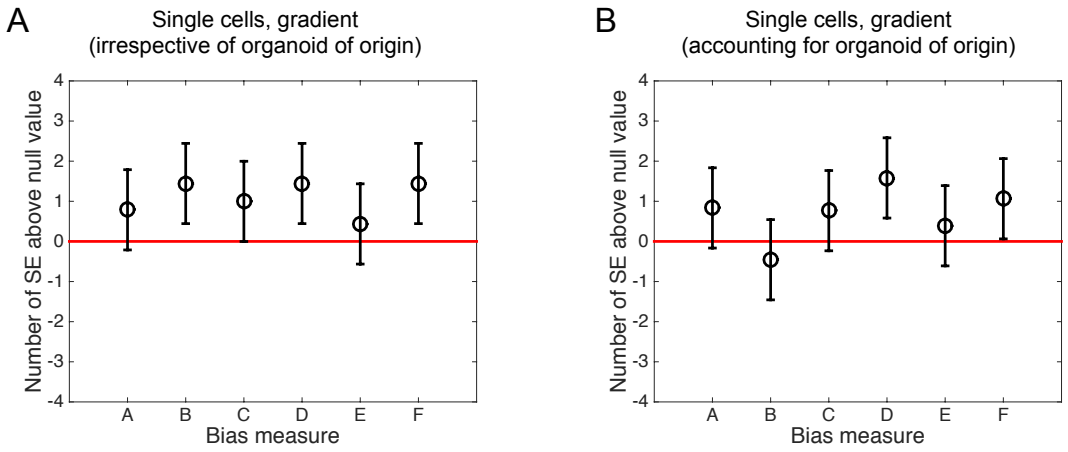

FIGURE 19: SINGLE-CELL MOVEMENT IS UNBIASED BY ALL MEASURES.

The six bias measures are shown for single-cell movement in a gradient of 0.5 nM/mm EGF (Figure 11E of the main text), taking as the fundamental unit (A) a single cell (analogous to Figure 17A) or (B) the net displacement of all single cells originating from a single organoid (analogous to Figure 17B). In both cases, the response is not significantly biased, and the absence of bias is robust to the choice of measure

3. MECHANISTIC MODEL OF COMMUNICATING CELLS

Here we present the stochastic model of gradient sensing by communicating cells. We consider a one-dimensional chain of N cells parallel to the gradient direction. As in the experiments, the mean EGF signal concentration varies linearly along the direction of the chain as

$$\bar{c}_n = \bar{c}_N - ag(N-n), \tag{1}$$

where $\bar{c}_n$ is the local concentration near the nth cell, a is the cell diameter, g is the concentration gradient, and $\bar{c}_N$ is the maximal concentration at the Nth cell. The observed independence of bias on background concentration (Figure 13C) supports an adaptive model of sensing. We therefore choose a minimal adaptive model based

on the principle of local excitation and global inhibition (LEGI) [112]. In the nth cell, both a local and a global molecular species are degraded at a rate μ and produced at a rate β in proportion to the number of signal molecules in the vicinity, which is roughly $c_n a^3$. Whereas the local species is confined to each cell, the global species is exchanged between neighboring cells at a rate γ, which provides the communication. Because there is no experimental evidence for receptor saturation (Figure 13C of the main text), we confine ourselves to the linear response regime, in which the dynamics of the local and global species satisfy the stochastic equations

$$\frac{dx_n}{dt} = \beta(c_n a^3) - \mu x_n + \eta_n, \tag{2}$$

$$\begin{aligned}\frac{dy_n}{dt} &= \beta(c_n a^3) - \mu y_n + \gamma(y_{n-1} + y_{n+1} - 2y_n) + \xi_n \\ &= \beta(c_n a^3) - \mu \sum_{n'=1}^{N} M_{nn'} y_{n'} + \xi_n,\end{aligned} \tag{3}$$

where

$$M_{nn'} \equiv (1 + 2\gamma/\mu)\delta_{nn'} - (\gamma/\mu)(\delta_{n',n-1} + \delta_{n',n+1}) \tag{4}$$

is the tridiagonal matrix governing degradation and exchange. Here x_n and y_n are the molecule numbers of the local and global species, respectively, and the terms η_n and ξ_n are the intrinsic Langevin noise terms with zero mean and covariances

$$\langle \eta_n(t)\eta_{n'}(t')\rangle = (\beta \bar{c}_n a^3 + \mu \bar{x}_n)\delta_{nn'}\delta(t - t'), \tag{5}$$

$$\begin{aligned}\langle \xi_n(t)\xi_{n'}(t')\rangle = [&(\beta \bar{c}_n a^3 + \mu \bar{y}_n + \gamma \bar{y}_{n-1} + \gamma \bar{y}_{n+1} + 2\gamma \bar{y}_n)\delta_{nn'} \\ &- (\gamma \bar{y}_n + \gamma \bar{y}_{n-1})\delta_{n',n-1} - (\gamma \bar{y}_n + \gamma \bar{y}_{n+1})\delta_{n',n+1}]\delta(t - t').\end{aligned} \tag{6}$$

Equation 5 and the first line of Eq. 6 contain the Poisson noise corresponding to each reaction, while the second line of Eq. 6 contains the anti-correlations between neighboring cells introduced by the exchange. Equations 4 and 6 are modified at the edges $n = \{1, N\}$ to include exchange with just one neighboring cell.

In the LEGI framework, the local species excites a downstream species, while the global species inhibits it. In the limit of shallow gradients, the relative noise in the excitation level of this downstream species is equivalent to that in the difference $\Delta_n = x_n - y_n$ between local and global species' molecule numbers. To see this, we recall from Ref. [112] that, in the LEGI model, the excitation level r depends on the ratio of activator x to inhibitor y as

$$r = \frac{x/y}{x/y + z}, \tag{7}$$

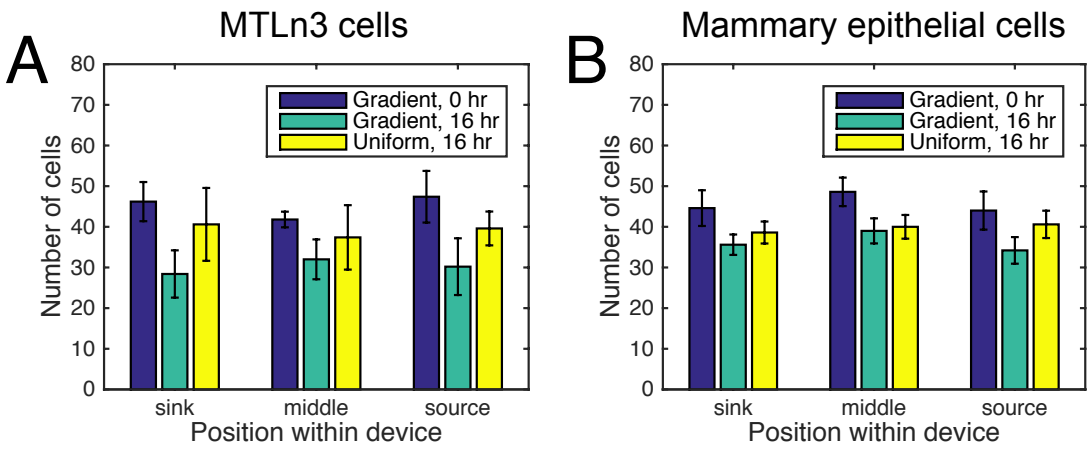

FIGURE 20: ABSENCE OF DIRECTIONAL SENSITIVITY IN INDIVIDUAL CELLS IS NOT A BYPRODUCT OF P-CADHERIN KNOCKOUT.

Motile MTLn3 single cells (A) and single cells from dispersed WT organoids (B) were deposited in the 0.5 nM/mm EGF gradient and 2.5 nM uniform EGF distribution for 3 days. No statistically significant accumulation of cells in different sections of the device

was noted, indicating absence of directional sensitivity, just like for the P-cadherin knockouts (Figure 11E).

where z is a constant. At equal activation and inhibition, $x = y$, the excitation level is $r_0 = 1/(1+z)$. Defining $s \equiv r - r_0$ as the deviation from this level, Eq. 7 can be written in terms of $\Delta = x - y$ and y as

$$s = \frac{z}{(1+z)^2}\frac{\Delta}{y}, \tag{8}$$

where, for shallow gradients, we have assumed that the quantity Δ/y is small. Small fluctuations among s, Δ, and y are therefore related as

$$\delta s = \frac{z}{(1+z)^2}\left(\frac{\delta\Delta}{\bar{y}} - \frac{\bar{\Delta}}{\bar{y}^2}\delta y\right), \tag{9}$$

or equivalently,

$$\left(\frac{\delta s}{\bar{s}}\right)^2 = \left(\frac{\delta\Delta}{\bar{\Delta}}\right)^2\left(1 - \frac{\bar{\Delta}}{\bar{y}}\frac{\delta y}{\delta\Delta}\right)^2 \approx \left(\frac{\delta\Delta}{\bar{\Delta}}\right)^2, \tag{10}$$

where the last step once again assumes $\bar{\Delta}/\bar{y}$ is small. Thus we see that relative fluctuations in s are equivalent to those in Δ. We therefore take Δ as our readout variable, focusing in particular on Δ_N, the molecule number difference in the cell furthest up the gradient, since this cell initiates the morphological branching observed in the experiment.

4. Absence of directional sensitivity in single cells

While Figure 11E showed the absence of directional sensitivity in individual cells, it remains possible that this insensitivity is a result of the P-cadherin knockout. To

alleviate this possibility, we deposited individual cells from the MTLn3 mammary epithelial cell line [88], as well as individual cells from dispersed WT organoids into the experimental device for 3 days. Over this time, the cells can move over distances comparable to those determined organoid experiments. Directionally biased motility would result in enrichment of cells in different device zones (source of EGF, middle of the device, and sink of EGF). As seen in Figure 21, no enrichment is observed, indicating that the absence of directional sensitivity in individual cells is not a byproduct of the P-cadherin knockout.

5. Instantaneous vs. temporally-integrated gradient sensing

Since the foundational publication of Berg and Purcell [12], most work on molecular sensing has considered the setup where a sensor integrates the signal over a certain time t, much larger than the typical turnover time of the ligand molecules, which is controlled by diffusion. As the diffusion brings new molecules to the vicinity of the sensor, fluctuations are averaged out, resulting in a typical $\sim 1/\sqrt{t}$ decrease of the sensory error. Analyses of gradient sensing not considering [127] and considering communication [107] among the neighboring cells have also revealed similar time dependence due to temporal integration. In contrast, Figure 20 shows the organoids do not exhibit an increase in sensory precision with time between 1 and 3 days of the experiment duration. This suggests that the integration (or memory) time in this system is smaller than the typical diffusive turnover time. As a consistency check, we point out that the diffusion coefficient of EGF in extracellular space is about 50 um^2/s [128]. Thus a typical diffusion time across a 300 um

organoid would be (300 um)^2/(50 um^2/s) = 30 min, so many biochemical signaling reactions – and integration scales defined by them – are faster (see [107] for a more careful analysis of time scales relevant for collective gradient sensing). Therefore, in what follows, we consider that Δ, an instantaneous steady-state, rather than time-averaged, difference of the local and the global messenger species, is the readout of our model most relevant for the experiments. At the same time, we refer the reader to the companion article, Ref. [107], where a full analysis with temporal integration is presented. The integration does not change the qualitative picture developed here (existence of a finite gradient sensing unit), but provides somewhat different values for the dependence of the sensory limits on the system parameters.

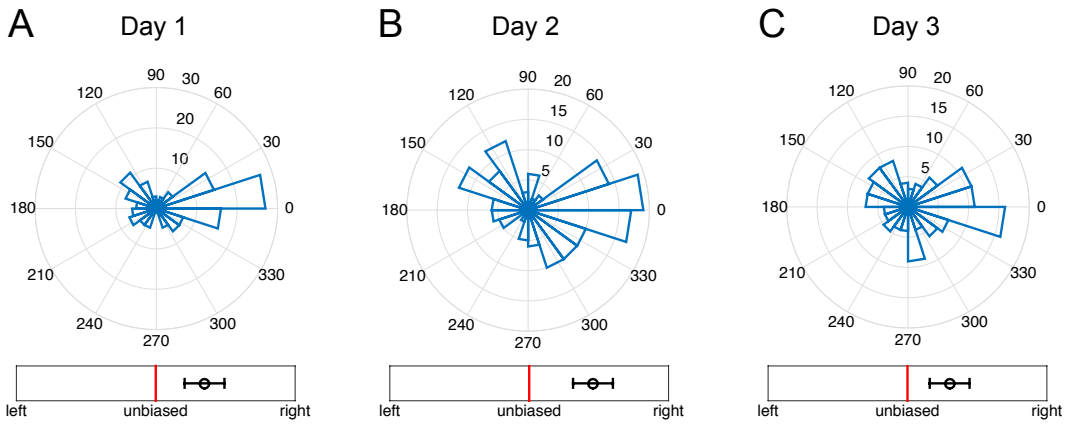

FIGURE 21: TEMPORAL STABILITY OF GRADIENT SENSING

Angular histograms of branch directions for new branches appearing during (A) day 1 (total 145 branches), (B) day 2 (total 157 branches), and (C) day 3 (total 132 branches) of continual exposure of organoids to a 0.5 nM/mm EGF gradient. Branch angles are plotted irrespective of the organoid from which each branch originates. The gradient of EGF is in the 0° direction. Plots are non-cumulative, in that B shows only branches that form during day 2 (and not day 1), and C shows only branches that form during day 3 (and not days 1 and 2). The number of branches changes since the organoids change their morphology with time, but there is clearly no evidence of an improving accuracy of branch formation angle, and hence no evidence of temporal

integration. Bias is measured by measure B from Figure 12 (but for individual branches, as in Figure 17).

6. MEAN AND VARIANCE OF THE READOUT VARIABLE

The mean and variance of the readout variable are

$$\bar{\Delta}_N = \bar{x}_N - \bar{y}_N, \tag{11}$$

$$(\delta\Delta_N)^2 = (\delta x_N)^2 + (\delta y_N)^2 - 2\ \mathrm{cov}(x_N, y_N), \tag{12}$$

where $\mathrm{cov}(x_N, y_N) = \langle (x_N - \bar{x}_N)(y_N - \bar{y}_N) \rangle$ is the covariance. These expressions in turn depend on the mean and variance of x_N and y_N, which we now calculate from Eqs. 2 and 3 in steady state. The mean of x_N follows straightforwardly from Eq. 2,

$$\bar{x}_N = G\bar{c}_N a^3, \tag{13}$$

where the term $G \equiv \beta/\mu$ describes the factor by which the number of local species molecules is amplified beyond the number of detected signal molecules. Similarly, the mean of y_N follows from Eq. 3,

$$\bar{y}_N = G \sum_{n=0}^{N-1} K_n \bar{c}_{N-n} a^3, \tag{14}$$

where $K_n \equiv M^{-1}_{N,N-n}$. We see that, due to the communication, the global species number in the edge cell is a weighted sum of the signal measurements made by all the other cells. The weighting is determined by K_n, which we call the communication kernel and discuss in detail in the next section.

The variance of x_N is easiest to derive in Fourier space. We first consider the fluctuations $\delta x_N = x_N - \bar{x}_N$ and $\delta c_N = c_N - \bar{c}_N$, in terms of which Eq. 2 reads

$$\frac{d\delta x_N}{dt} = \beta \delta c_N a^3 - \mu \delta x_N + \eta_N. \tag{15}$$

Fourier transforming and rearranging obtains

$$\tilde{\delta x}_N = \frac{\beta \tilde{\delta c}_N a^3 + \tilde{\eta}_N}{\mu - i\omega}. \tag{16}$$

Since we are interested in the instantaneous readouts only, the variance is then the integral over all frequencies of the power spectrum $S_x(\omega) = \langle \tilde{\delta x}_N^* \tilde{\delta x}_N \rangle$,

$$(\delta x_N)^2 = \int_{-\infty}^{\infty} \frac{d\omega}{2\pi} S_x(\omega) = \beta^2 \int_{-\infty}^{\infty} \frac{d\omega}{2\pi} \frac{S_c(\omega) a^6}{\mu^2 + \omega^2} + \int_{-\infty}^{\infty} \frac{d\omega}{2\pi} \frac{\langle \tilde{\eta}_N^* \tilde{\eta}_N \rangle}{\mu^2 + \omega^2}, \tag{17}$$

where the cross terms vanish because signal fluctuations are not cross-correlated with local species fluctuations. The noise spectrum follows from Eq. 5, $\langle \tilde{\eta}_N^* \tilde{\eta}_N \rangle = \beta \bar{c}_N + \mu \bar{x}_N = 2\mu \bar{x}_N$, upon which the second term in Eq. 17 integrates to $\bar{x}_N$. The first term in Eq. 17 depends on the power spectrum of signal fluctuations, which for a Poisson process with timescale τ reads $S_c(\omega) a^6 = 2\tau \bar{c}_N a^3 / [1 + (\omega\tau)^2]$. We are considering instantaneous readouts, which is equivalent to the diffusion of EGF being slow, i.e., $\tau \to \infty$ and $S_c(\omega) a^6 \to 2\pi \delta(\omega) \bar{c}_N a^3$. This is the same as assuming that the number of signal molecules is Poisson-distributed but fixed in time. Thus Eq. 17 becomes

$$(\delta x_N)^2 = G^2 \bar{c}_N a^3 + \bar{x}_N. \tag{18}$$

The first term is the extrinsic noise. It arises from fluctuations in the signal molecule number. Since these fluctuations are Poissonian, the variance of the signal molecule number equals its mean $\bar{c}_N a^3$. Then, as these fluctuations are propagated

to the local species, they are amplified by the gain G^2. The second term is the intrinsic noise. The intrinsic noise arises from fluctuations in the local species number itself. These fluctuations are also Poissonian, and thus the variance equals the mean $\bar{x}_N$.

We follow the same procedure to find the variance of y_N. The result is

$$(\delta y_N)^2 = G^2 \sum_{n=0}^{N-1} K_n^2 \bar{c}_{N-n} a^3 + \bar{y}_N. \tag{19}$$

The extrinsic noise (first term) once again scales with the gain G^2. It depends on the same kernel K_n that determines the mean, which reflects the fact that, as seen in Eq. 15, upstream fluctuations propagate through linear systems in the same way as the signals themselves [129]. The intrinsic noise (second term) is once again equal to the mean $\bar{y}_N$, which is a necessary consequence of the fact that Eq. 3 is an open system whose reaction rates are linear in the species numbers [130].

Finally, we apply the same technique to find the covariance, which is the integral over all frequencies of the cross-spectrum $\langle \tilde{\delta x}_N^* \tilde{\delta y}_N \rangle$. The result is

$$\mathrm{cov}(x_N, y_N) = G^2 K_0 \bar{c}_N a^3. \tag{20}$$

This expression has a straightforward interpretation: it is the product of two extrinsic standard deviations. The first is the square root of the extrinsic noise in the local species, $\sigma_x \equiv \sqrt{G^2 \bar{c}_N a^3}$. The second is the square root of the extrinsic noise in the global species, but only the component affecting the Nth cell, $\sigma_y \equiv \sqrt{G^2 K_0^2 \bar{c}_N a^3}$. The reason that only extrinsic noise enters is because x_N and y_N only co-vary due to

fluctuations in the extrinsic signal. The reason that only the Nth component of the global noise contributes is because the local species is not communicated, and thus any effect on y_N due to other cells cannot co-vary with x_N. Finally, the reason that the covariance takes the form of a product of standard deviations is because x_N and y_N depend identically on the signal (Eqs. 2 and 3), and therefore the correlation coefficient corresponding to extrinsic fluctuations $\mathrm{cov}_{\mathrm{extrinsic}}(x_N, y_N)/(\sigma_{x_N}\sigma_{y_N})$ is equal to one.

From the mean, variance, and covariance of x_N and y_N, the mean and variance of the readout variable follow via Eqs. 11 and 12. The only thing that remains is to solve for the communication kernel K_n, which we describe next.

7. Communication kernel

The communication kernel $K_n \equiv M^{-1}_{N,N-n}$ is found by inverting the tridiagonal matrix $M_{nn'}$. First we derive the inverse, and then we present an approximation of K_n in the limit of strong communication and many cells.

Defining $\rho \equiv \mu/\gamma$, the diagonal (u), superdiagonal (v), and subdiagonal (w) terms of $\rho M_{nn'}$ (Eq. 4) are

$$\begin{aligned} u_n &= \begin{cases} \rho+1 & n=1, \\ \rho+2 & 2 \le n \le N-1, \\ \rho+1 & n=N, \end{cases} \\ v_n &= -1 \qquad 1 \le n \le N-1, \\ w_n &= -1 \qquad 1 \le n \le N-1. \end{aligned} \tag{21}$$

The inverse of any tridiagonal matrix can be calculated by recursion [131, 132],

$$M^{-1}_{nn'} = \rho \begin{cases} (-1)^{n+n'} v_n \dots v_{n'-1} \theta_{n-1} \phi_{n'+1} / \theta_N & n \le n', \\ (-1)^{n+n'} w_{n'} \dots w_{n-1} \theta_{n'-1} \phi_{n+1} / \theta_N & n > n', \end{cases} \tag{22}$$

where θ_n and ϕ_n satisfy

$$\begin{aligned} \theta_0 = 1, \quad \theta_1 = u_1, \quad \theta_n = u_n \theta_{n-1} - v_{n-1} w_{n-1} \theta_{n-2} \quad & 2 \le n \le N, \\ \phi_{N+1} = 1, \quad \phi_N = u_N, \quad \phi_n = u_n \phi_{n+1} - v_n w_n \phi_{n+2} \quad & N-1 \ge n \ge 1. \end{aligned} \tag{23}$$

Since both v_n and w_n are constant and equal to -1, Eq. 22 simplifies to

$$M^{-1}_{nn'} = \rho \begin{cases} \theta_{n-1} \phi_{n'+1} / \theta_N & n \le n', \\ \theta_{n'-1} \phi_{n+1} / \theta_N & n > n'. \end{cases} \tag{24}$$

From Eq. 24 we can also deduce that the inverse is symmetric. We write the first few terms of θ_n and notice the pattern,

$$\begin{aligned} &\theta_0 = 1, \\ &\theta_1 = \rho + 1, \\ &\theta_2 = (\rho+2)(\rho+1) - 1 = \rho^2 + 3\rho + 1, \\ &\theta_3 = (\rho+2)[(\rho+2)(\rho+1) - 1] - (\rho+1) = \rho^3 + 5\rho^2 + 6\rho + 1, \\ &\quad \vdots \\ &\theta_n = \sum_{j=0}^{n} \binom{n+j}{2j} \rho^j \quad 0 \le n \le N-1. \end{aligned} \tag{25}$$

The last term θ_N does not conform to the pattern because u_N is different from its previous terms, so we calculate θ_N explicitly from θ_{N-1} and θ_{N-2} and simplify,

$$\theta_N = \sum_{j=1}^{N} \binom{N+j-1}{2j-1} \rho^j. \tag{26}$$

Then, since v_n and w_n are constants and $u_n = u_{N-n+1}$, we notice from Eq. 23 that

$$\phi_n = \theta_{N-n+1}. \tag{27}$$

Inserting Eqs. 25-27 into Eq. 24 and simplifying, and recalling that the inverse is symmetric, we arrive at the expression

$$M^{-1}_{nn'} = M^{-1}_{n'n} = \frac{\sum_{j=0}^{n-1} \binom{n-1+j}{2j} \rho^j \sum_{k=0}^{N-n'} \binom{N-n'+k}{2k} \rho^k}{\sum_{\ell=0}^{N-1} \binom{N+\ell}{2\ell+1} \rho^\ell} \quad n \leq n' \tag{28}$$

for the inverse. The communication kernel is a particular case,

$$K_n \equiv M^{-1}_{N,N-n} = \frac{\sum_{j=0}^{N-n-1} \binom{N-n-1+j}{2j} \rho^j}{\sum_{\ell=0}^{N-1} \binom{N+l}{2l+1} \rho^\ell} \quad . \tag{29}$$

The communication kernel is normalized, $\sum_{n=1}^{N} K_n = 1$, which is consistent with its interpretation as a weighting function.

Now we show that in the limit of strong communication and a large number of cells, the communication kernel can be approximated by an exponential distribution. Since all dependence on n occurs in the numerator of Eq. 29, we approximate the numerator only, and then we set the denominator using the fact that K_n is normalized. The approximation of the numerator follows two steps. First, the factorials in the choose function are written using the Stirling approximation. Second, the sum is simplified using the saddle point approximation.

We expect K_n to have the strongest support at the edge cell and nearby cells, i.e. for small values of n. Therefore, applying the Stirling approximation to the numerator of Eq. 29 is valid in the limit

$$N \gg j^* \gg 1, \tag{30}$$

where j^* is the value at which the summand peaks. We will see below that this condition is satisfied in the limit of strong communication and many cells.

Ignoring the denominator, we write the exchange kernel as $K_n \propto \sum_j e^{-g_j}$, where

$$\begin{aligned} g_j &\equiv -\log\left[\binom{N-n-1+j}{2j}\rho^j\right] \\ &= -\log\left[(N-n-1+j)!\right] + \log\left[(N-n-1-j)!\right] + \log\left[(2j)!\right] - j\log\rho. \end{aligned} \tag{31}$$

Applying the Stirling approximation $\log(x!) = (x+1/2)\log x - x + (1/2)\log(2\pi)$ yields

$$\begin{aligned} g_j = & -\left(N-n+j-\frac{1}{2}\right)\log(N-n+j-1) + \left(N-n-j-\frac{1}{2}\right)\log(N-n-j-1) \\ & + \left(2j+\frac{1}{2}\right)\log(2j) - j\log\rho + \frac{1}{2}\log 2\pi. \end{aligned} \tag{32}$$

We now apply the saddle point approximation, which means we approximate j as continuous and expand g_j to second order around its minimum value, permitting the evaluation of a Gaussian integral,

$$K_n \propto \sum_j e^{-g_j} \approx \int dj \ \exp\left[-g_* - \frac{1}{2}g_*''(j-j_*)^2\right] = e^{-g_*}\sqrt{\frac{\pi}{g_*''}}. \tag{33}$$

Here j^* is the value at which the minimum g_* occurs and at which the second derivative g_*'' is evaluated. It is found by setting to zero the first derivative of Eq. 32,

$$\begin{aligned} g_j' = & -\log(N-n+j-1) - \log(N-n-j-1) + 2\log(2j) - \log\rho \\ & - \frac{1}{2(N-n+j-1)} - \frac{1}{2(N-n-j-1)} + \frac{1}{2j}. \end{aligned} \tag{34}$$

Ignoring the last three terms because their denominators are precisely the three quantities we have assumed are large, we solve $g_j' = 0$ to find

$$j^* = \psi(N - n - 1), \tag{35}$$

where $\psi \equiv \sqrt{\rho/(\rho+4)}$. Eq. 35 shows that $j^* \sim \psi N$, which means Eq. 30 can be written

$$1 \gg \psi \gg 1/N. \tag{36}$$

The left condition in Eq. 36 requires that ψ is small. This is satisfied in the strong communication limit $\gamma \gg \mu$, since then $\psi \approx \sqrt{\rho}/2 = \sqrt{\mu/\gamma}/2 \ll 1$. The right condition in Eq. 36 requires that N is large (there are many cells), such that the kernel falls to nearly zero still within the organoid.

Inserting Eq. 35 value into Eq. 32 yields

$$g_* = -\left(N - n - \frac{1}{2}\right)\log\left(\frac{1+\psi}{1-\psi}\right) + \frac{1}{2}\log[4\pi\psi(n-1)]. \tag{37}$$

Then differentiating Eq. 34, once again ignoring the last three terms,

$$g_j'' = \frac{-1}{N-n+j-1} + \frac{1}{N-n-j-1} + \frac{2}{j}, \tag{38}$$

and inserting Eq. 35 yields

$$\begin{aligned} g_*'' &= \frac{-1}{(1+\psi)(N-n-1)} + \frac{1}{(1-\psi)(N-n-1)} + \frac{2}{\psi(N-n-1)} \\ &= \frac{2}{\psi(1-\psi^2)(N-n-1)}. \end{aligned} \tag{39}$$

Now we evaluate the saddle point result (Eq. 33),

$$\begin{aligned} K_n &\propto \exp\left[\left(N - n - \frac{1}{2}\right)\log\left(\frac{1+\psi}{1-\psi}\right)\right]\sqrt{\frac{1}{4\pi\psi(N-n-1)}}\sqrt{\frac{\pi\psi(1-\psi^2)(N-n-1)}{2}} \\ &\propto e^{-n/n_0}, \end{aligned} \tag{40}$$

where in the second step we drop all n-independent prefactors and define $n_0 \equiv 1/\log[(1+\psi)/(1-\psi)]$. We recover the proper prefactor by enforcing normalization, $1 = \sum_n K_n \approx \int dn\ K_n$,

$$K_n \approx \frac{1}{n_0} e^{-n/n_0}, \tag{41}$$

and we see that the kernel falls off exponentially with the number of cells n from the edge cell.

The kernel length scale n_0 can be simplified in the strong communication limit, in which $\psi \approx \sqrt{\rho}/2$ is small,

$$n_0 \approx \frac{1}{\log(1+2\psi)} \approx \frac{1}{2\psi} \approx \frac{1}{\sqrt{\rho}} = \sqrt{\frac{\gamma}{\mu}}. \tag{42}$$

We see that the length scale is the square root of the ratio of a diffusion term (γ) to a degradation term (μ). This is the same form as the length scale of morphogen profiles that are set up by diffusion and degradation, which, like the communication kernel, are exponential in shape [133].

8. Fundamental limit to the precision of instantaneous gradient sensing with communication

We now complete our calculation of the relative noise in the readout variable Δ_N. In the strong communication and many cells limit, the sums in Eqs. 14 and 19 can be approximated as integrals over all positive n that are then easily evaluated using the exponential form of the kernel (Eq. 41) due to the linearity of $\bar{c}_n$ in n (Eq. 1). We insert the results, along with Eqs. 13, 18, and 20, into Eqs. 11 and 12 to obtain

$$\bar{\Delta}_N = \bar{x}_N - \bar{y}_N = G\bar{c}_N a^3 - G\bar{c}_{N-n_0} a^3 = G(n_0 a g)a^3, \tag{43}$$

$$(\delta\Delta_N)^2 = \left(G^2\bar{c}_N a^3 + \bar{x}_N\right) + \left(G^2\frac{\bar{c}_{N-n_0/2}}{2n_0}a^3 + \bar{y}_N\right) - 2\left(G^2\frac{\bar{c}_N}{n_0}a^3\right), \tag{44}$$

From Eqs. 43 and 44 we obtain the relative noise

$$\left(\frac{\delta\Delta_N}{\bar{\Delta}_N}\right)^2 = \frac{1}{a^3(n_0 a g)^2}\left[\left(\bar{c}_N + \frac{\bar{c}_{N-n_0/2}}{2n_0} - 2\frac{\bar{c}_N}{n_0}\right) + \frac{1}{G^2}\left(\bar{c}_N + \bar{c}_{N-n_0}\right)\right]. \tag{45}$$

Eq. 45 gives the relative uncertainty in the system's estimate of the gradient via its readout Δ_N, in the limit of many cells. In the brackets, the first term in parentheses arises due to the extrinsic noise. The second term in parentheses arises due to the intrinsic noise. The extrinsic and intrinsic terms have a similar structure, and in general as a function of N they will have a similar shape, because they both arise from the same kernel (Eq. 29). The intrinsic term reflects the counting noise from the finite number of internal communicating molecules. The extrinsic noise reflects the imperfect averaging performed by the global molecular species, since it has a finite communication length scale.

In principle, the intrinsic noise can be made arbitrarily small by producing more local and global species molecules, which is equivalent to increasing the gain G. Moreover, we observe that in the extrinsic noise, the second and third terms are smaller than the first term by a factor of n_0. This is because these terms, which involve the global species, benefit from measurements of the external signal across roughly n_0 cells due to the communication. These terms are therefore small relative to the first in the strong communication limit. We are then left with

$$\left(\frac{\delta\Delta_N}{\bar{\Delta}_N}\right)^2 = \frac{\bar{c}_N}{a^3(n_0 a g)^2}. \tag{46}$$

This is the central result of this section. Eq. 46 is the fundamental limit to the precision of instantaneous (not temporally averaged) gradient sensing via a LEGI-style adaptive, communicating system. Unlike for a system with temporal integration [107], Eq. 46 does not depend on the measurement time and depends on the spatial averaging scale as $\sim 1/n_0^2$.

Figure 22 shows the values of $(\mathrm{SNR}_N)^{1/2} = \bar{\Delta}_N/\delta\Delta_N$, from Eqs. 11, 12 with the limiting values, or the fundamental limits, given by Eq. 45. In particular, Figure 22D and E are the analogs of Figure 13B and C, except that Figure 13 plots the estimate of the organoid bias, $P(\Delta_N > \Delta_1)$, which is easily obtained from SNR_n. Note that in Figure 22D, SNR_N decreases at large N because large organoids push the Nth cell to higher concentrations, where gradient sensing is less precise. In contrast, in Figure 13B, the bias $P(\Delta_N > \Delta_1)$ saturates, for two reasons: (i) bias derives from the both SNR_1 and SNR_N, which are pushed to opposite concentration regimes for large organoids, and (ii) Figure 13 also includes additive downstream noise, which is independent of both size and concentration, and thus tends to flatten out

dependencies.

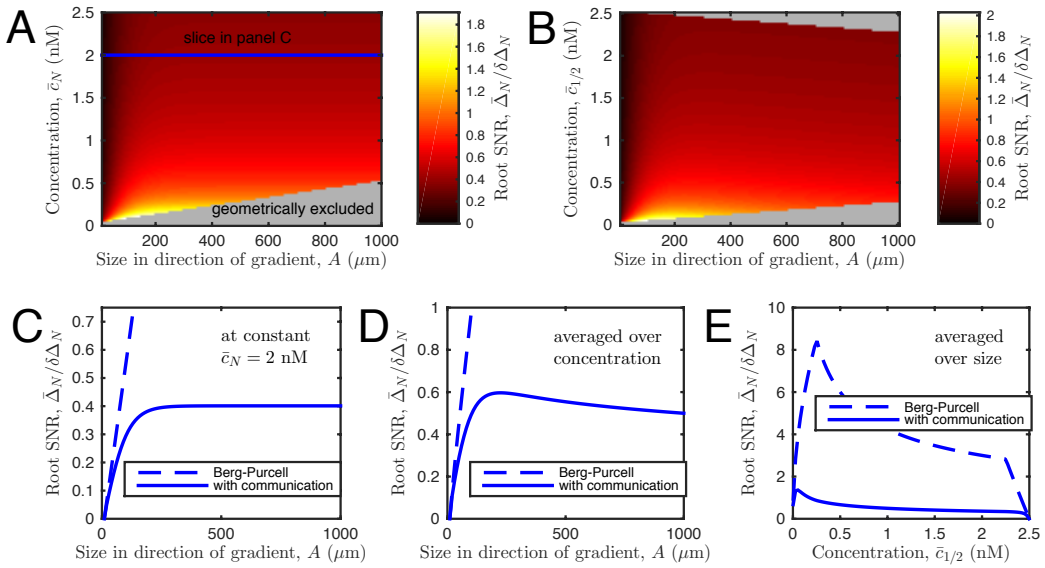

FIGURE 22: PRECISION OF GRADIENT SENSING IN A MODEL ACCOUNTING FOR CELL-TO-CELL COMMUNICATION.

Signal-to-noise ratio (SNR) vs. (A) organoid size A and (B) background concentration. For reference we show the concentration referenced at both the edge cell $\bar{c}_N$ (A) and the midpoint cell $\bar{c}_{1/2}$ (B). The fact that the largest organoids must be centered within the device, and therefore have maximal $\bar{c}_N$ and median $\bar{c}_{1/2}$, gives rise to the geometrically excluded regions in A and B. (C) SNR vs. size at constant $\bar{c}_N$ (see slice in A), and the corresponding estimate based on the work of Berg and Purcell (BP) and others [12, 74, 76, 78] (Eq. 1 in the main text). Whereas SNR for BP increases indefinitely with size, SNR in our theory saturates due to the finite length of cell communication. (D) SNR vs. size, averaged over all geometrically allowed concentrations, and organoid sizes between 10 and 1000 µm. SNR now decreases at large size, since the largest organoids have the largest $\bar{c}_N$ values, and gradient sensing is less precise on a large background concentration. Note that whereas SNR decreases with size here, bias still saturates with size in Figure 13B, for reasons explained in the text here. (E) SNR vs. concentration $\bar{c}_N$, averaged over all geometrically allowed sizes. Parameters are a = 10 µm, g = 0.5 nM/mm, G = 10, and n_0 = 5.

9. Spatially resolved Gillespie stochastic simulations to explore modification of fundamental limits to the precision of instantaneous gradient sensing under violation of linearity assumptions

Reaction	Rate
$A_n^* + R_n \rightarrow A_n^* R_n$	5e-2
$A_n^* R_n \rightarrow A_n^* + R_n$	5e-4
$A_n^* R_n \rightarrow A_n^* + R_n^*$	1e-3
$I_n^* + R_n^* \rightarrow I_n^* R_n^*$	5e-2
$I_n^* R_n^* \rightarrow I_n^* + R_n^*$	5e-4
$I_n^* R_n^* \rightarrow I_n^* + R_n$	1e-3
$S_n + A_n \rightarrow S_n A_n$	5e-2
$S_n A_n \rightarrow S_n + A_n$	5e-4
$S_n A_n \rightarrow S_n + A_n^*$	1e-3
$A_n^* \rightarrow A_n$	1e-4
$I_n + S_n \rightarrow I_n S_n$	5e-2
$S_n I_n \rightarrow S_n + I_n$	5e-4
$S_n I_n \rightarrow S_n + I_n^*$	1e-3
$I_n^* \rightarrow I_n$	1e-4
$I_n^* \rightarrow I_{n+1}^*$	1e-2
$I_n^* \rightarrow I_{n-1}^*$	1e-2
$I_n \rightarrow I_{n+1}$	1e-2
$I_n \rightarrow I_{n-1}$	1e-2

TABLE 1: SIMULATION PARAMETERS USED IN THE SPATIALLY-EXTENDED GILLESPIE SIMULATIONS WITH LOW SATURATION.

Our theory above made two linearity assumptions. First, we assumed that receptors are not saturated at high ligand concentrations, allowing us to treat the production rate of messenger molecules as a linear function of the position. Second, we assumed that the readout is the difference of the local and the diffusive messenger. In more conventional analysis of LEGI models, the readout is the concentration a

response molecule *R*, positively modified by the activator *A* and negatively modified by the inhibitor, *I* [75, 111, 112]. To verify how our findings for the fundamental limits of collective gradient sensing are affected by these assumptions, we set up numerical stochastic and spatially-extended simulations of the system. Organoids were simulated using the HSim rule-based modeling program [134], version released 4/27/2015. For parameter exploration, a Python script generated model files with appropriate parameters and called HSIM with random seeds. Simulations were run on IBM NeXtScale nodes with Intel Xeon E5-2660 V2 and V3 processors.

Simulations were run for model organoids represented as coupled linear chains with the following numbers of cells: 3, 6, 10, 12, 15, 20, 25, and 50. For each simulated cell *n*, a set of molecules (S_n, A_n, I_n, R_n) was initiated which interacted only with each other (Table S1). In the LEGI model, S_n (the signal molecule) activates A_n and I_n. The activated A_n was allowed to activate R_n, and the activated I_n was allowed to deactivate it. I_n was also allowed to diffuse to become $I_{n\pm1}$. Each interaction was modeled as a Michaelis-Menten reaction. A_n and I_n were both allowed to deactivate with equal rates. Spherical cells with diameter 10 micron were initialized with $A_n = 1000$, $I_n = 1000$, $R_n = 500$, and $R_n^* = 500$ molecules. S_N was initialized to 1000 in each simulation's final cell, with the gradient of 5 molecules per cell. All kinetic parameters present in both the theory and the simulations were selected to match (see Figure 14 of the main text and Table S1). To investigate the effects of saturation, deactivation rates of A_n and I_n were scaled by 1/4 and 1/10 for partial and full saturation, respectively. High saturation of A_n and I_n was confirmed

by removing reactions with R_n and observing nonlinear response to varying S_n. The diffusion rate of I_n was scaled accordingly to maintain a communication strength $n_0 = \sqrt{\gamma/\mu} = 10$ cells. Supplementary Table S1 shows the values of all kinetic rates used in the low saturation simulations.

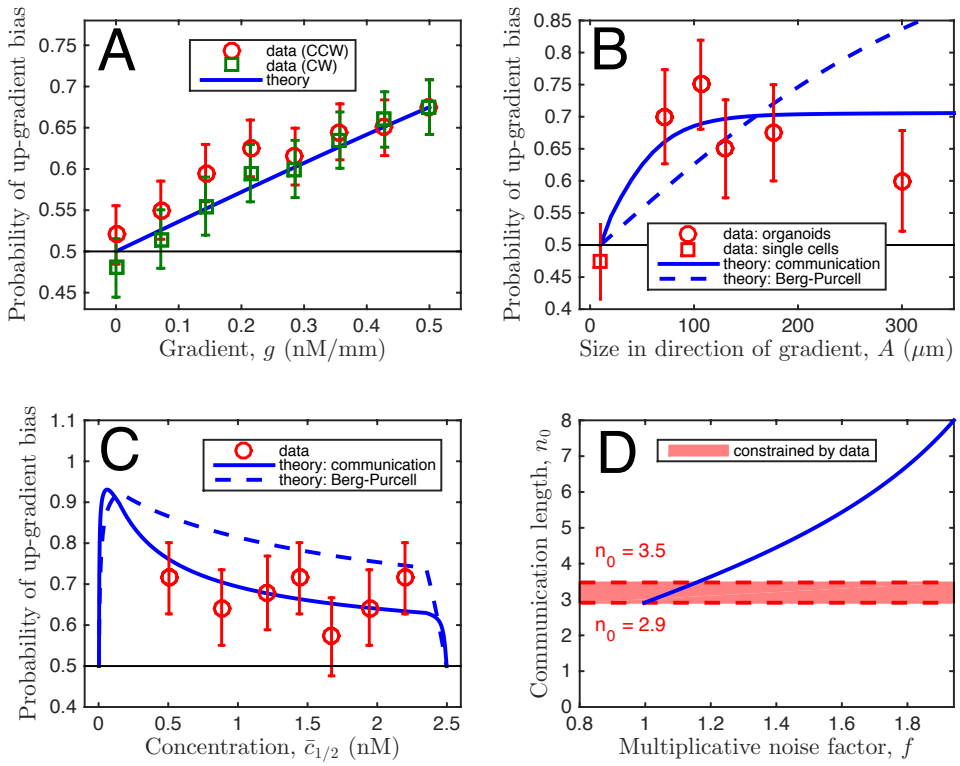

FIGURE 23: COMPARISON OF DATA WITH THEORY, WITH MULTIPLICATIVE INSTEAD OF ADDITIVE NOISE.

Identical to Figure 13 of the main text, except that in the theory the downstream noise is multiplicative, instead of additive, as described in the text here. Importantly, the conclusions, namely that the data support our theory with communication over BP theory (B and C), and our estimate for n_0 (here between 2.9 and 3.5) (D), are robust to the treatment of downstream noise.

For each scenario (low, medium, and high saturation) and each number of cells, 16,384 simulations were run for a total of 393,216 runs. Simulations were ran

sufficiently long (10,000 sec) so that the SNR had reached the steady state. SNR is reported as the squared mean over the variance of

$$\frac{R_n^* - R_n}{(R_n^* + R_n)/2}$$

in the final cell at the end of simulations. Error bars are determined by bootstrap sampling, reporting variance of 100 re-samples of size 16,384 taken from the original data with replacement.

10. Limits on the size of the multicellular sensory unit with multiplicative downstream noise

In the main text, Figure 13, we compared theoretical predictions of the BP model, as well as the model accounting for the communication noise, with the experimental data under the assumption that the noise in initiation of the phenotypic response, downstream of the gradient sensing, is additive. Here we consider a multiplicative noise model. For the BP theory, we again calculate the probability that the measured number of ligand molecules in the *N*'th cell is larger than in the first, $\nu_N > \nu_1$. However, now we take ν_n as Gaussian-distributed with mean $\bar{c}_n a^3$ and variance $\bar{c}_n a^3 f^2$, where $f^2 \geq 1$ represents the multiplicative increase due to downstream noise. Similarly, for our theory with diffusive communication, we calculate the probability that $\Delta_N > \Delta_1$, where Δ_n is Gaussian-distributed with mean $\bar{\Delta}_n$, and variance $(\delta\Delta_n)^2 f^2$, where both $\bar{\Delta}_n$ and $(\delta\Delta_n)^2$ are calculated earlier in this Supplementary Information. Figure 23 is the multiplicative noise analog of Figure 13. Importantly, Figure 23 demonstrates that our results depend only weakly on the assumed properties of the

downstream noise. In particular, with either additive or multiplicative noise, the data support our theory with communication over BP theory (Figure 13B and C, and Figure 23B and C), and we obtain similar estimates of the multicellular sensory unit given by n_0 (Figure 13D and Figure 23D).

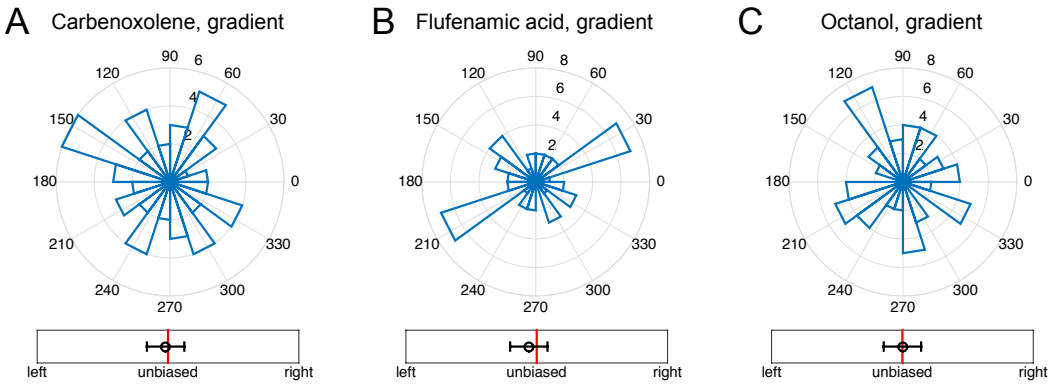

FIGURE 24: GAP-JUNCTION BLOCKING DRUGS REMOVE BIASED RESPONSE OF ORGANOIDS

Directional histograms of organoids in 0.5 nM/mm EGF gradient after treatment with (A) 50 μM Carbenoxolone (2 biological replicates, 3 experimental replicates, total 59 organoids, total 206 branches), (B) 50 μM Flufenamic acid (2 biological replicates, 3 experimental replicates, total 49 organoids, total 173 branches), and (C) 0.5 mM Octanol (2 biological replicates, 3 experimental replicates, total 64 organoids, total 222 branches). In all cases, as well with Endothelin-1 (Fig. 5A in the main text), the treatment removes the directional response seen in wild type organoids (Figure 11D in the main text).

11. TREATMENTS WITH GAP JUNCTION-BLOCKING DRUGS REMOVE ORGANOID RESPONSE TO EGF GRADIENTS

In addition to Endothelin-1, Figure 24 confirms that other other gap-junction blocking drugs also remove the directional response of the organoids.

12. CALCIUM SIGNALING IS COORDINATED IN NEARBY CELLS

To test the hypothesis that the global, diffusive inhibitory messenger in the organoids is related to calcium signaling (such as IP3 or calcium itself) we manually tracked 5 cells in the area at the front of a growing branch in an organoid derived from a transgenic mouse expressing genetically encoded Ca reporter GCaMP4, under the control of the CAG promoter [115], see Figure 25. Calcium spikes in these cells are highly synchronized, indicating communication by calcium spikes inducing messengers. Note also that the size of the tip is consistent with our estimate of the gradient sensing unit (about 4 cells)

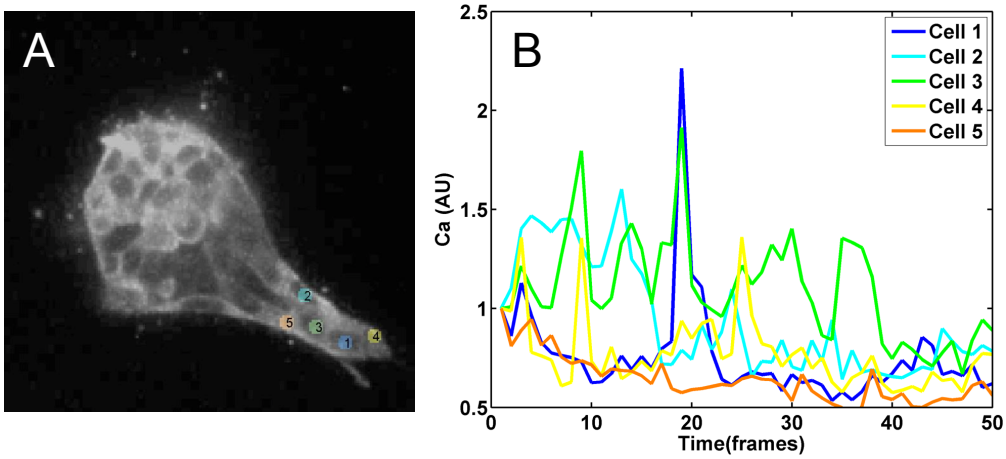

FIGURE 25: CALCIUM SIGNALING IN GROWING ORGANOID BRANCHES

(A) Five cells are tracked in the growing tip of an organoid for 500 min (see Supp. Movie 1 for the movie of the first two hours of the growth). (B) Calcium signal from each of the five cells, color-coded as in (A). Each frame is 10 min. Notice multiple cells firing nearly synchronously at frames 3, 9, 14, and 19, indicating coupling among the adjacent cells.

13. GRADIENT ESTABLISHMENT IN THE DEVICE

Numerical simulations show that a linear gradient of EGF, a 6.4 kDa protein, is established in our device in less than 24 hrs. We verify this by flowing an easily

observable 10 kDa fluorescent protein (Dextran, Cascade Blue, Life Technologies) through the system and imaging it a day after the initition of the experiment. Figure 26, indeed, shows a nearly linear gradient. EGF is smaller, has a higher diffusion coefficient, and will establish a stable gradient even faster.

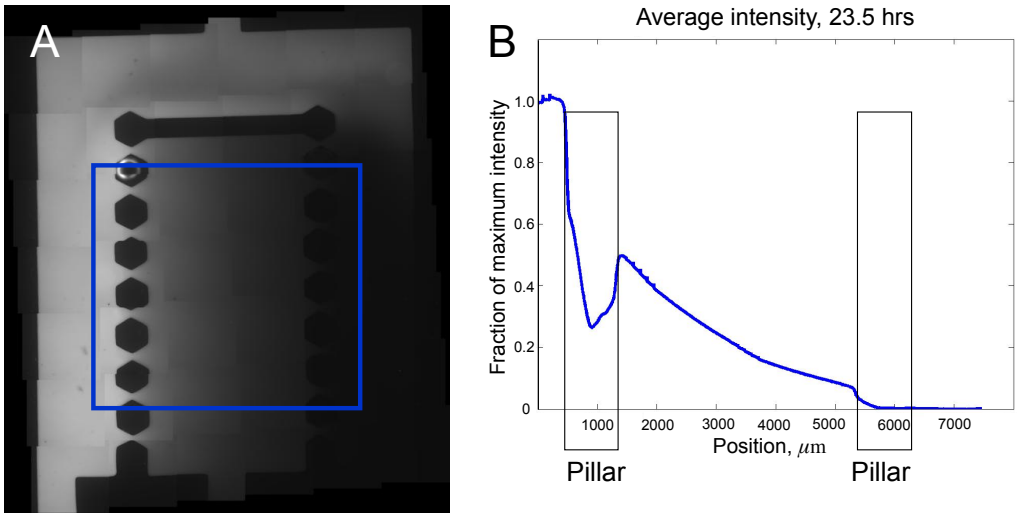

FIGURE 26: GRADIENT ESTABLISHMENT IN THE EXPERIMENTAL DEVICE.

(A) Image of the device with the 0.5 nM/mm gradient of 10 kDa Dextran Blue used to visualize diffusion of EGF. Area over which the concentration is averaged is shown by a blue square. (B) Average gradient within the blue square as a function of the distance from the left edge of the device, 23.5 hours after the start of the experiment. A nearly linear profile is visible.

Chapter 5 Robust detection of signal duration in genetic and signaling networks

Background

It has recently been discovered that a number of cell signaling systems are responsive to the duration of a signal [15, 135-138]. If one were to imagine what circuit is behind that detection, the simplest that could come to mind is an integrator. Its peak signal would correspond to the amount of time that a signal was present for. Integration, however is naturally affected not only by the duration of a signal, but also by its amplitude. In the context of this detection problem, variations in amplitude would be a confounding "noise" to the detection circuit.

While fast, intrinsic fluctuations in signal strength could be smoothed by integration, extrinsic fluctuations tend to occur on larger time scales. Extrinsic noise has been repeatedly shown to be a dominant source of noise in biochemical signaling networks [8, 139]. In genetic networks, this noise can come from transcriptional bursts and variations in transcription factor or ribosome copy numbers. In chemosensory networks, this noise can come from both fluctuations of the actual signal or variation in number of receptors. Any of these effects may occur on time scales slower than signal detection time, thus presenting a serious challenge to an integrating circuit attempting to detect duration.

Given these challenges, it is of interest to identify somewhat more complex circuits which are capable of detecting signal duration in the face of amplitude noise. By

identifying basic motifs which are capable of performing this task, we may accomplish multiple goals. First, when biological systems have been found to detect signal duration, we will give researchers a motif to focus on, narrowing their search for specific mechanisms. Secondly, when such a motif has been found in a biological system, researchers will know to attempt experiments with inputs of duration besides simply varying input strength. Finally, we will provide a design pattern which synthetic biologists may use in applications for which signal duration may be of interest.

In the following sections, we will explore the Incoherent Type 1 Feed Forward Loop (I1FFL) motif. As one of the most common network motifs, and has several identified functions including pulse generation, response time reduction, and fold-change detection [16-19, 140]. Here, we demonstrate a new function: its ability to accurately decode signal duration in the presence of amplitude noise. While many features of the I1FFL have been described in literature, the circuit has not previously been analyzed in the context of this dynamic signal. In this chapter, we will demonstrate the circuit's basic ability, understand how its may be explained by basic equations describing the circuit, and explore how broadly (in terms of circuit parameter variation) the circuit may perform this task.

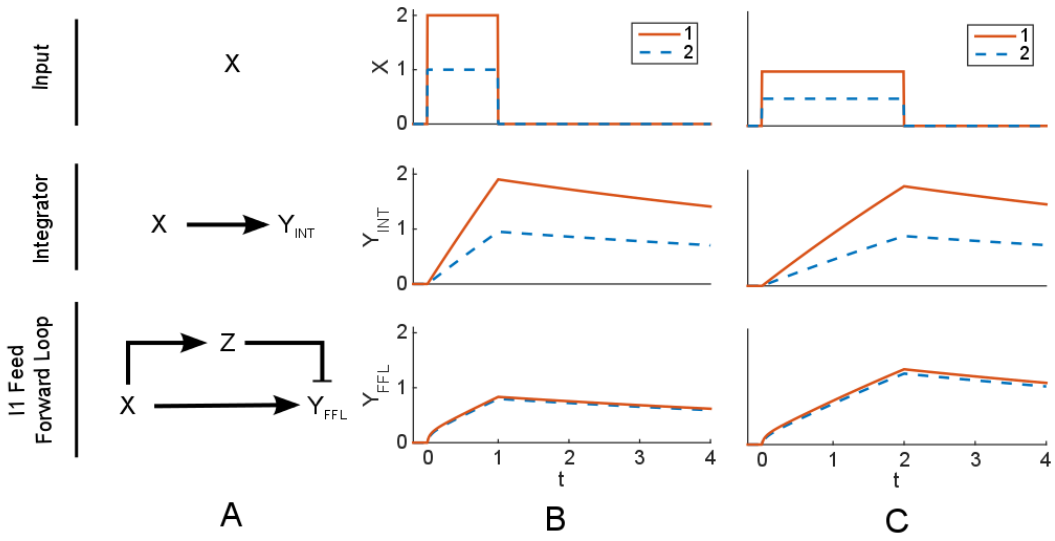

FIGURE 27: COMPARISON OF A SIMPLE INTEGRATOR AND A FEED FORWARD LOOP

A) Schematics of a simple integrator network and an Incoherent Type-1 Feed Forward Loop. B) Two inputs (X) of duration 1 and different amplitudes are plotted, along with the integrator and I1FFL networks' responses to each. For inputs of the same duration, the peak integrator response to one signal is 100% larger than to the other, while the peaks of the I1FFL response differ by only 4%. C) Two inputs (X) of duration 2 and different amplitudes are plotted. Again, the integrator response is 100% different for these inputs while the I1FFL response shows only 6% difference. Notice that between figures B and C, the maximum value of the FFL grows with the duration, while the maximum value of the integrator corresponds to the combination of the duration times the amplitude. Simulation parameters for the integrator are B=1, a3=1/10. Simulation parameters for the I1-FFL are B_0=20, a_1=10, B_1=15, K_1=1, K_2=1/10, K_3=1000, a_2=1/3.

THE I1FFL CAN DECODE SIGNAL DURATION

The feed forward loop motif consists of an input node (X), an intermediate node (Z) which is affected by X, and a final output node (YFFL) which is affected both by X and Z. In the Incoherent Type 1 Feed Forward Loop (I1FFL), the direction of these effects is as shown in Figure 27A and described in the equations below:

$$\frac{dZ}{dt} = \beta_0 X - \alpha_1 Z \quad (1)$$

$$\frac{dY_{FFL}}{dt} = \beta_1 \frac{X/K_1}{1 + X/K_1 + Z/K_2 + XZ/K_1K_2K_3} - \alpha_2 Y_{FFL} \quad (2)$$

We first consider some specific examples of how the I1FFL may behave differently than an integrating circuit (Figure 27, Table 2). We perform simple ODE calculations of the equations describing the I1FFL and the integrator in Matlab, and present each circuit with four inputs. When presented with inputs of equal duration but differing amplitudes, the maximum output of the integrator doubles with the doubled amplitude, while the maximum output of the I1FFL changes by only 4-6%. It is also notable that the maximum response of the integrator to inputs labeled 1 and 2 is nearly identical between Figure 27 panels B & C. This is caused by the inputs having the same value of their amplitude times duration (or, area under the signal), as you would expect for an integrator. The I1FFL does not share this behavior, maintaining similar maximum outputs only for similar duration signals.

X Dur	X Amp	max(Y_{INT})	% Diff Y_{INT}	max(Y_{FFL})	% Diff Y_{FFL}
1	2	0.95	100%	0.80	4%
1	1	1.9		0.83	
2	1	0.9	100%	1.3	6%
2	0.5	1.8		1.4	

TABLE 2: MAXIMUM RESPONSE OF INTEGRATOR AND FFL TO INPUTS

Table of inputs and maximum responses to signals, corresponding to plots and simulation parameters in Figure 27B,C. While Y_{INT} (integrator response) doubles when amplitude doubles, Y_{FFL} (I1FFL response) changes by 6% or less.

To understand how the I1FFL performs this task, we can observe that Z is a repressive element that mirrors the strength of X (Figure 27A). When Y_{FFL} is

repressed by Z in proportion to the amount it is activated by X, then we would expect the level of both cancel out and only the amount of time that the signal is activated to affect its output.

To evaluate this intuitive understanding more rigorously, we consider a system where Z achieves steady-state much faster than Y_{FFL}. At steady state, this gives $Z = X\,{}^{\beta_0}/_{\alpha_1}$. If we assume ${}^{X}/_{K_1} + {}^{Z}/_{K_2} \gg 1 + {}^{XZ}/_{K_1K_2K_3}$, then equation 2 reduces to

$$\begin{aligned}\frac{dY_{FFL}}{dt} &= \beta_1 \frac{{}^{X}/_{K_1}}{{}^{X}/_{K_1} + {}^{X\beta_0}/_{\alpha_1 K_2}} - \alpha_2 Y_{FFL} \\ &= C - \alpha_2 Y_{FFL}\end{aligned}$$

where

$$C = \beta_1 \frac{K_2\alpha_1}{K_2\alpha_1 + K_1\beta_0}$$

is not a function of X. This approximation of course requires X>0, however the degradation term already requires that X be above a certain threshold in order to affect Y_{FFL}. Thus, we have shown how, under a few assumptions, the I1FFL circuit, in the presence of any signal, may increase at a rate which is not determined by the amplitude of the input signal.

Cooperativity, Z K_D and Gain Are Key Parameters

So far, in order to demonstrate the plausibility of the I1FFL's detection capability, we have considered circuits with specific example parameters or assumed

constraints on parameter values. In order to understand whether this capability of signal detection in the presence of amplitude noise extends broadly to I1FFL circuits without hand-selected parameters, we must determine which parameters are the most important to the circuit's performance.

In order to quantify the performance of a circuit with a given set of parameters, we must consider its response to a range of signal durations as well as a distribution of random amplitudes. By running many simulations of each circuit for a set of signal durations (X_{dur}), taking a random value for signal amplitudes (X_{amp}) we may build up the circuit's probabilistic response $P(Y_{FFL}|X_{dur})$. For simplicity, we will continue to refer to Y_{FFL} as a single value, $\max(Y_{FFL}(t))$, of the system's dynamic output.

Next, we must reduce this joint distribution for a given set of parameters to a single performance metric, indicating how responsive Y_{FFL} is to X_{dur}. To do this, we will utilize the information-theoretic concept of capacity. Capacity measures the maximum amount of information shared between two random, but related, variables. In this case, we consider the variables to be X_{dur} and Y_{FFL}, and capacity is computed as

$$C = \max_{P(X_{dur})} \mathrm{I}(X_{dur}; Y_{FFL})$$

where

$$
\begin{aligned}
\mathrm{I}(X_{dur};Y_{FFL}) &= \sum_{X_{dur},Y_{FFL}} \mathrm{P}(X_{dur},Y_{FFL}) \log_2 \frac{\mathrm{P}(X_{dur},Y_{FFL})}{\mathrm{P}(X_{dur})\mathrm{P}(Y_{FFL})} \\
&= \sum_{X_{dur},Y_{FFL}} \mathrm{P}(Y_{FFL}|X_{dur})\mathrm{P}(X_{dur}) \log_2 \frac{\mathrm{P}(Y_{FFL}|X_{dur})\mathrm{P}(X_{dur})}{\mathrm{P}(X_{dur})\mathrm{P}(Y_{FFL})} \\
&= \sum_{X_{dur},Y_{FFL}} \mathrm{P}(Y_{FFL}|X_{dur})\mathrm{P}(X_{dur}) \log_2 \frac{\mathrm{P}(Y_{FFL}|X_{dur})}{\sum_{X_{dur}} \mathrm{P}(Y_{FFL}|X_{dur})\mathrm{P}(X_{dur})}
\end{aligned}
$$

Therefore, I(X_{dur}; Y_{FFL}) can be seen as a function of P(X_{dur}) and P(Y_{FFL}|X_{dur}). Since capacity is maximized over P(X_{dur}), it is reduced to be a function of only P(Y_{FFL} | X_{dur}), the distribution which we have already described how to obtain.

Now that we have a metric describing the performance of the circuit, we can use a sensitivity analysis to explore which parameters affect it the most. We choose to use the FAST sensitivity analysis method, primarily due to its ability to handle non-linear and non-monotonic functions [141]. The output of the FAST analysis is a metric which determines, over all parameter sets explored, what percent of variance in the performance was determined by variance in each parameter. We evaluated 1000 parameter sets per parameter, for a total of 7000 sets. Most parameters were allowed to vary from 1e-4 to 1. The exception to this was parameter K_3, the cooperativity parameter. Since values of K_3 less than 1 indicate cooperative binding, while values of K_3 greater than 1 indicate competitive binding, K_3 was allowed to vary from 1e-4 to 10. For each parameter set, 20 durations were evaluated. 10,000 simulations were run for each duration, for a total of 1.4 billion simulations. Simulations were run in Python 2.7.6 [142] leveraging the NumPy Library [143]. FAST analysis was performed in R [144] using the sensitivity package [145]. We found that the most significant parameters, measured either by first order effect or

total effect, were K_3 (cooperativity), K_2 (the K_D of Z), and B_1 (the gain of Y_{FFL} from X, relative to its decay).

Parameter	Variance contribution
K_3	36%
K_2	32%
B_1	28%
α_2	2%
K_1	1%
α_1	0%
B_0	0%

TABLE 3: FAST PARAMETER SENSITIVITY ANALYSIS

Summary of the results of the FAST parameter sensitivity analysis. Evaluating 7,000 different parameter sets, each parameter is sorted by the percent of variance in the circuit's capacity that was attributable to variation of that parameter. This variance contribution and ranking give us an indication of how important a parameter is to the I1FFL's ability to detect signal duration in the presence of amplitude noise.

I1FFL Detects Duration Better Than Amplitude Over a Wide Range of Parameters

Now that key parameters have been identified, we are able to determine consider whether the circuit does indeed behave as a duration detector over a reasonable range of parameters. While any positive value of capacity is sufficient to show that the circuit is capable of conveying information about signal duration, we would like to show that it may be more likely intended to convey information about duration than other signal properties, such as amplitude.

In order to determine this, we consider C_{dur} / $C_{amp.}$ C_{dur} = C(X_{dur}; Y_{FFL}) is the metric used in the previous section, the capacity between signal duration and YFFL. We will

calculate it in the same manner as before, picking a parameter set and a range of durations, and running many simulations with random signal amplitudes. To measure C_{amp} = C(X_{amp}; Y_{FFL}), we will perform similar experiments. For the same set of parameters, we will choose a set of amplitudes, and run many simulations with random signal durations.

Based on our previous results, we are primarily interested in the circuits performance when varying the three parameters B_1, K_2, and K_3. We run three sets of analyses, each time varying two of the three parameters, fixing all others (Figure 28). We see that over a wide range of the three parameters, the circuit provides better response to signal duration than it does to signal amplitude. This suggests that not only is the I1FFL capable of transducing information about signal duration, it is indeed the most likely output for I1FFL circuits with a significant range of parameters.

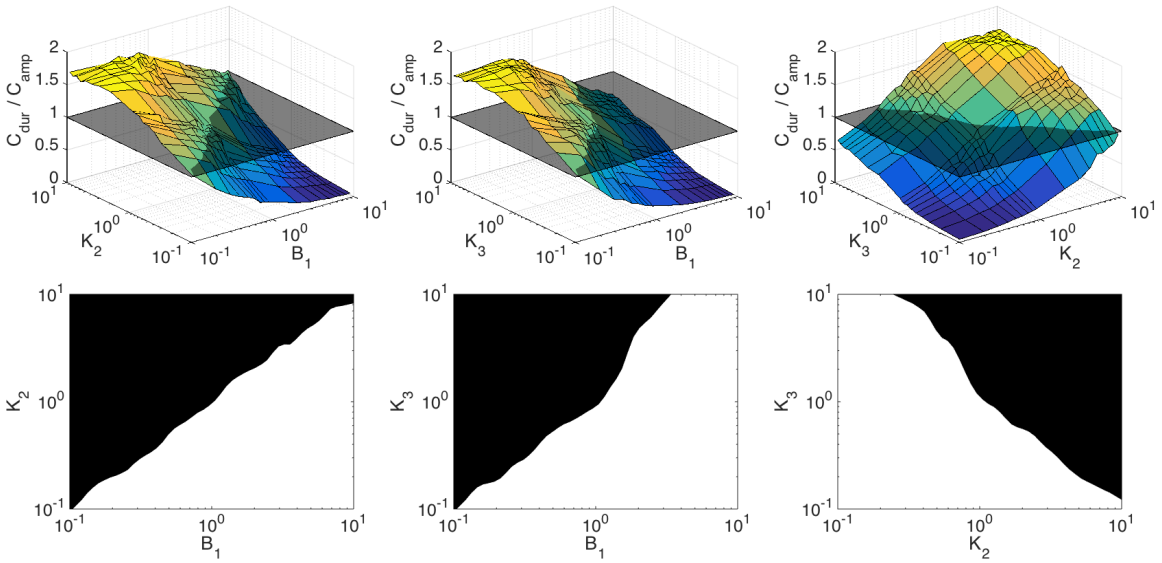

B_1 vs K_2 B_1 vs K_3 K_2 vs K_3

FIGURE 28: RELATIVE RESPONSE OF I1-FFL TO AMPLITUDE VS DURATION ACROSS PARAMETERS

Plots of C_{dur}/C_{amp}*, the relative ability of the I1FFL to convey information about duration vs amplitude, over a range of parameters. Values greater than 1 imply that the circuit carries more information about signal duration than it does about signal amplitude. Top charts display the exact value of* C_{dur}/C_{amp}*. Bottom charts are black where* C_{dur}/C_{amp} *is greater than 1. We ran simulations of fixed durations with random amplitudes to calculate* C_{dur}*, and simulations of fixed amplitudes with random durations to calculate* C_{amp}*. We vary combinations of two parameters at a time, limited to the three parameters determined to be most influential to the I1FFLs amplitude detection capability in the above sensitivity analysis.*

RESPONSE OF CIRCUIT TO SPECIFIC SCENARIOS

Finally, we consider some additional variations of parameters and inputs. While all inputs given to the system so far have been pulse inputs, we consider that many signals may take a different shape, or that a sharp pulse may be distorted by the time it is transduced by other elements of a signaling network. We evaluated the circuits basic response to a linear ramp input, and find that it does still reliably respond to signal duration rather than signal amplitude (Figure 29A).

Next, we consider that a circuit which is able to detect "duration" of a signal could be misled if the "off" level of a signal is non-zero, since we may expect that it could be driven by the duration of the non-zero "off" signal. We simulated a circuits which were exposed to 1% of the signal amplitude long enough to reach steady state, and then presented them with a full-strength fixed-duration response (Figure 29B). We find that the circuit is still capable of responding to the full strength signal, and that its maximum amplitude is still predictive of the signal duration and not the signal amplitude. Its reactions to signals of different durations is, however, somewhat compressed relative to a circuit which was not exposed to a background signal.

Finally, we consider that signal durations of interest may be longer than the adaptation time of the sensing circuit (Figure 29C). Indeed, if B_1 and g_2 are greatly increased, the circuit response is very fast, and Y_{FFL} reaches a maximum which is driven by the input signal's amplitude, not its duration.

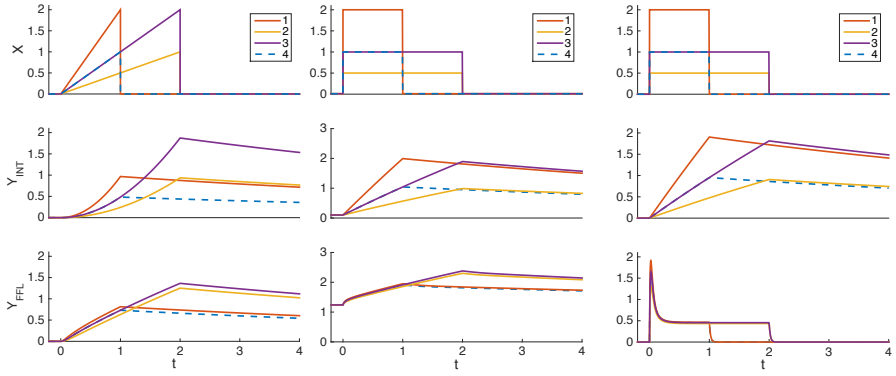

FIGURE 29: RESPONSE OF CIRCUIT TO VARIOUS CHALLENGES

Response of I1FFL (Y_{FFL}) and simple integrator (Y_{INT}) to changes in input and parameters. A) A linear ramp input. Performance is equivalent to a pulse input, with the Y_{INT} response changing by 100% in response to different amplitudes and the YFFL response changing by <11%. B) The presence of a continuous signal of 0.01 (1% of or 0.5% of considered amplitudes of 1 and 2, respectively). Performance is equivalent, though it is clear that the variation of Y_{FFL} responses to signals of different durations is compressed. C) Consideration of a fast FFL circuit. We set B_1=500 and g_2=50, and observe that the circuit is not capable of detecting durations on the same order as before, as its maximum value is reached while the signal is still present.

DISCUSSION

In this chapter, we have shown the superior ability of the I1FFL circuit to detect the duration of a signal. We have shown that it may do this robustly under a wide range of parameters and multiple input signal shapes. We have laid the groundwork for future explorations of circuits where signal duration is of interest (such as T-Cells). Further, as the I1-FFL is one of the most common signaling motifs, we expect that analysis of some of the dynamic response of these circuits may reveal other biological systems where signal duration is a driving factor.

While the I1FFL circuit has been extensively researched in the past, it has most often been analyzed in the context of its steady-state responses. Here, we considered not only the dynamic response of the circuit but also what "noise," or challenges to detection, exist in such a system. These considerations revealed this circuit's duration detection ability.

Chapter 6 DISCUSSION

SUMMARY OF RESULTS

In this dissertation, we have explored multiple facets of how noise affects biological systems. In order to do so, we have brought to bear techniques from engineering and math to improve our understanding of biology. We have introduced new techniques for analyzing noise, and demonstrated how including noise in analysis changes our understanding of how systems perform. In Chapter 2, we emphasized this by considering the ways in which Information Theory can be a revealing tool in biological research.

In Chapter 3, we investigated an important development pathway in the model organism *Drosophila*. We developed original software to rapidly and accurately measure the nuclearized Dorsal based on confocal microscope images. This both increased the number of nuclei we were able to analyze in a short amount of time, necessary for performing solid statistical analysis, and reduced levels of experimental noise.

We then developed a novel technique of noise deconvolution, separating out symmetric and asymmetric components of noise in the Dorsal profile. This technique produces results analogous to the frequently-used intrinsic/extrinsic noise paradigm [8, 73] and expands the growing field of techniques for noise deconvolution [6, 50, 146-148]. Using this technique and additional experiments

with multiple developmental timepoints, we show that width noise is a dominant source of embryo-to-embryo variation in the Dorsal profile.

In Chapter 4, we developed experimentally-grounded theoretical and computer simulation models to evaluate gradient detection in multi-cellular organoids. In contrast to previous results, we show that it is not ideal for an organism attempting to sense a gradient to grow indefinitely. Experimental data was collected on mouse mammary epithelial organoids, a model for breast cancer, in collagen to closely simulate their *in vivo* environment [103, 105]. We develop a three-dimensional computer simulation model to evaluate the performance of LEGI, a commonly-considered paradigm in gradient sensing [112]. By considering the noisy internal communication required to transfer information about the concentration of a chemical in multiple points to a single point insides of the cell, we show that the marginal benefit of organism size rapidly goes to zero. Our theoretical and computer simulations agree with evidence from our experimental data.

Finally, in Chapter 5, we considered the implications for a system for which the detection of signal duration is important but signal amplitude may be variable. We show that while sensing by a simple integrating circuit is confounded by amplitude variation, a common signaling system motif, the type 1 incoherent feed-forward loop, is able to detect the duration of a signal. While many capabilities of the I1-FFL have been evaluated before, we discover this new ability by focusing on the system's dynamic response as well as reconsidering what aspects of a signal may be considered noise.

Research Implications

This dissertation has repeatedly provided evidence that the consideration of noise is critical to understanding biological systems. We showed that detailed analysis and separation of noise sources point to critical aspects of biological system design. Consideration of multiple sources of noise (ie, internal and external) affected fundamental changes in our understanding of a common biological system (gradient sensing). In the case of duration detection, we showed that noise places new constraints on the design of biological systems.

We expect that these results, combined with the expanding base of research on biological noise, will continue to drive biologists towards large single-cell studies. While previously it has been sufficient to provide bounds on a system's mean response, we expect that it will become increasingly commonplace for scientists to desire bounds on second-order statistics [46]. Biological noise may come from many sources. Certainly, some noise measured by scientists will be due to experimental error. Some variation which may initially appear as random noise may be attributed to predictable sources, such as cell cycle or developmental timepoint. Indeed, by investigation of the noise, we may discover that some biological systems are even more precise than originally believed. Regardless, without precisely measuring and understanding the noise, we cannot fully understand a biological system.

This dissertation has also reiterated the value of information-theoretic techniques in measuring the capabilities of a variable system. While previous applications in systems biology have often compared the amount of information in a signal to the

entropy required to make decisions of uniform probability ($H=\log_2[num.\ decisions]$), we have proposed that an organism may have encoded information already (ultimately stored in its genome) which can reduce the uncertainty it has about a decision prior to making it. This, in turn, reduces the entropy of the decision, and the amount of information required to make it. We expect that future studies will not only increasingly use information theory as a performance metric when analyzing biological systems, but also take careful consideration of the complexity of the decision a system when evaluating the amount of information available.

Future Directions

While we chose to apply the method of symmetric noise deconvolution to Drosophila morphogenesis, it was developed sufficiently broadly to be applicable to many other systems which display bilateral symmetry. An obvious next application could be to Sonic Hedgehog signaling, which controls vertebrate neural tube patterning in a symmetric manner [149]. More distantly, the same essential technique could be applied to fully developed bilateral organisms. Could variation in blood pressure in humans left and right femoral arteries be used to identify blockage in the upstream descending aorta?

Our work found that there were two possible explanations for the amount of information available in the Drosophila morphogen. Because there was more information than you would expect for patterning three regions of gene expression, we explored the possibility that this additional information may provide environmental robustness. Experiments which measure the amount of information

available in the Dorsal morphogen when the development is challenged by its environment, such as high temperatures, would provide additional evidence for this theory. Secondly, we showed that given the strength of width noise, the amount of information available to nuclei may be significantly increased if the organism is able to cope with that noise in some way. While some research has shown that there are plausible mechanisms for Drosophila to handle width variation later in development [64], more research is needed to confirm this possibility.

Our analysis of gradient detection was based on a multi-cellular organoid, providing a clear exchange of diffusive communicating molecules between discrete cells. Single cells, however, frequently are required to detect gradients on their own. Expansion of our work to the single cell domain will include extending the theoretical model to a continuous domain, as well as performing computer simulations where molecules are explicitly placed around the cell. We explicitly chose HSIM in our computer model development for its ability to be expanded to such a domain, including the possible inclusion of membrane-bound molecules. We expect that the development of such work would only reinforce the importance of considering internal communication noise to gradient detection models and biological systems.

The work we performed on analysis of duration detection circuits is just the tip of the iceberg, with many possible future avenues of exploration. While the I1-FFL circuit is shown to be very good at duration detection, a comprehensive analysis of all multi-node networks may reveal other circuits which may perform as well or

better. In general, this analysis of circuit dynamics may also extend beyond detection of duration. We have also left it to future work to directly evaluate an I1-FFL circuit detection duration in a biological system. While T-cell differentiation has already been identified as a system that responds to duration, we expect that given the prevalence of I1-FFL circuits, many others may exist.

Besides naturally occurring examples, we also expect this analysis of I1-FFL circuits to be leveraged in synthetic biology circuit designs. As in nature, noise poses a significant challenge in synthetic biology circuits [150]. Circuit designs which are robust to various types of noise may be leveraged by synthetic biology circuits to increase their robustness.

Final Thoughts

When I decided to return to graduate studies, I was disinclined to continue in the field of wireless communications theory, having left with a feeling that many of the fields' fundamental problems had been solved (don't tell my former advisor). In the years I spent between programs, my exposure to biology quickly revealed both how many fundamental problems still exist, and how mathematical and engineering training could be brought to bear on those problems. Biological variation is one such problem. Without understanding, and dissecting, biological variation, we are unable to fully model the systems we study and understand the underlying causes of variation in atypical individuals. Further, we will be challenged in accurately dosing interventions in variable diseases, or miss the modulation of variation as a therapeutic target. It is my hope that, taken together, my contributions have

provided new analytical tools for studying biomedical problems, have shed additional light on the importance of biological noise, and will help drive an increasingly wide-held view that variation is a fundamental aspect of biology.

REFERENCES

1. Thattai M, van Oudenaarden A (2001) Intrinsic noise in gene regulatory networks. *Proceedings of the National Academy of Sciences* 98:8614—8619.

2. Waltermann C, Klipp E (2011) Information theory based approaches to cellular signaling. *Biochimica et Biophysica Acta (BBA) - General Subjects* 1810:924—932.

3. Wang J, Zhang J, Yuan Z, Zhou T (2007) Noise-induced switches in network systems of the genetic toggle switch. *BMC Systems Biology* 1:50+.

4. Ziv E, Nemenman I, Wiggins CH (2007) Optimal Signal Processing in Small Stochastic Biochemical Networks. *PLoS ONE* 2:e1077+.

5. Spencer SL, Gaudet S, Albeck JG, Burke JM, Sorger PK (2009) Non-genetic origins of cell-to-cell variability in TRAIL-induced apoptosis. *Nature* 459:428—432.

6. Paulsson J (2004) Summing up the noise in gene networks. *Nature* 427:415—418.

7. Hooke R (1665). Microphagia, or, Some physiological descriptions of minute bodies made by magnifying glasses: With observations and inquiries thereupon. London: Printed by J. Martyn and J. Allestry.

8. Swain PS, Elowitz MB, Siggia ED (2002) Intrinsic and extrinsic contributions to stochasticity in gene expression. *Proceedings of the National Academy of Sciences* 99:12795—12800.

9. Elowitz MB, Levine AJ, Siggia ED, Swain PS (2002) Stochastic gene expression in a single cell.. *Science (New York, N.Y.)* 297:1183—116.

10. Lawrence PA (1992) The Making of a Fly: The Genetics of Animal Design. Oxford, Blackwell Scientific Publications.

11. Hong J, Hendrix DA, Papatsenko D, Levine MS (2008) How the Dorsal gradient works: Insights from postgenome technologies. *Proceedings of the National Academy of Sciences* 105:20072—20076.

12. Berg HC, Purcell EM (1977) Physics of chemoreception.. *Biophysical journal* 20:193—219.

13. Rappel W, Levine H (2008) Receptor noise limitations on chemotactic sensing. *Proceedings of the National Academy of Sciences* 105:19270—19275.

14. Ebisuya M, Kondoh K, Nishida E (2005) The duration, magnitude and compartmentalization of ERK MAP kinase activity: mechanisms for providing signaling specificity. *Journal of Cell Science* 118:2997—3002.

15. Miskov-Zivanov N, Turner MS, Kane LP, Morel PA, Faeder JR (2013) The Duration of T Cell Stimulation Is a Critical Determinant of Cell Fate and Plasticity. *Science Signaling* 6:97.

16. Ghosh B, Karmakar R, Bose I (2005) Noise characteristics of feed forward loops. *Physical Biology* 2:36+.

17. de Ronde WH, Tostevin F, Wolde PRT (2012) Feed-forward loops and diamond motifs lead to tunable transmission of information in the frequency domain. *Physical Review E* 86:021913+.

18. Locasale J (2008) Signal duration and the time scale dependence of signal integration in biochemical pathways. *BMC Systems Biology* 2:108+.

19. Goentoro L, Shoval O, Kirschner MW, Alon U (2009) The Incoherent Feedforward Loop Can Provide Fold-Change Detection in Gene Regulation. *Mol Cell* 36:894—899.

20. Morel P, Faeder J, Hawse W, Miskov-Zivanov N (2014) Modeling the T cell immune response: a fascinating challenge. *J Pharmacokinet Pharmacodyn* 41:401—413.

21. Shannon CE (1948) A Mathematical Theory of Communication. *Bell System Technical Journal* 27:379—423.

22. Cover TM, Thomas J (1991) Elements of Information Theory. New York: John Wiley and Sons.

23. Cheong R, Rhee A, Wang CJ, Nemenman I, Levchenko A (2011) Information Transduction Capacity of Noisy Biochemical Signaling Networks. *Science* 334:354—358.

24. Dubuis JO, Tkacik G, Wieschaus EF, Gregor T, Bialek W (2013) Positional information, in bits. *Proceedings of the National Academy of Sciences* :201315642+.

25. Alberts B, Johnson A, Lewis J, Raff M, Roberts K, Walter P (2007) Molecular Biology of the Cell. Abingdon, UK: Garland Science

26. Losick R, Desplan C (2008) Stochasticity and Cell Fate. *Science* 320:65—68.

27. Fuller D, Chen W, Adler M, Groisman A, Levine H, Rappel W, Loomis WF (2010) External and internal constraints on eukaryotic chemotaxis. *Proceedings of the National Academy of Sciences* 107:9656—9659.

28. Lenski RE, Travisano M (1994) Dynamics of adaptation and diversification: a 10,000-generation experiment with bacterial populations. *Proceedings of the National Academy of Sciences* 91:6808—6814.

29. Acar M, Becskei A, van Oudenaarden A (2005) Enhancement of cellular memory by reducing stochastic transitions. *Nature* 435:228—232.

30. Borst A, Theunissen FE (1999) Information theory and neural coding. *Nature Neuroscience* 2:947—957.

31. Andrews BW, Iglesias PA (2007) An Information-Theoretic Characterization of the Optimal Gradient Sensing Response of Cells. *PLoS Comput Biol* 3:e153+.

32. Berger T (2003) Living Information Theory. *IEEE Information Theory Society Newsletter* 53:1+.

33. Polani D (2009) Information: currency of life?. *HFSP journal* 3:307—316.

34. Barabasi A, Oltvai ZN (2004) Network biology: understanding the cell's functional organization. *Nat Rev Genet* 5:101—113.

35. de Ronde W, Tostevin F, ten Wolde PR (2011) Multiplexing Biochemical Signals. *Physical Review Letters* 107:048101+.

36. Tkacik G, Callan CG, Bialek W (2008) Information flow and optimization in transcriptional regulation. *Proceedings of the National Academy of Sciences* 105:12265—12270.

37. Simoncelli EP, Olshausen BA (2001) Natural Image Statistics and Neural Representation. *Annual Review of Neuroscience* 24:1193—1216.

38. Bowsher CG, Swain PS (2012) Identifying sources of variation and the flow of information in biochemical networks. *Proceedings of the National Academy of Sciences* 109:E1320—E1328.

39. Cohen-Saidon C, Cohen AA, Sigal A, Liron Y, Alon U (2009) Dynamics and Variability of ERK2 Response to EGF in Individual Living Cells. *Mol Cell* 36:885—893.

40. Milenkovic O, Alterovitz G, Battail G, Coleman TP, Hagenauer J, Meyn SP, Price N, Ramoni MF, Shmulevich I, Szpankowski W (2010) Introduction to the Special Issue on Information Theory in Molecular Biology and Neuroscience. *IEEE Transactions on Information Theory* 56:649—652.

41. Mian IS, Rose C (2011) Communication theory and multicellular biology. *Integr. Biol.* 3:350—367.

42. Pandini A, Fornili A, Fraternali F, Kleinjung J (2012) Detection of allosteric signal transmission by information-theoretic analysis of protein dynamics.. *FASEB journal* 26:868—881.

43. Turing AM (1952) The chemical basis of morphogenesis. *Philosophical Transactions of the Royal Society of London. Series B, Biological Sciences* 237:37—72.

44. Ashe HL, Briscoe J (2006) The interpretation of morphogen gradients. *Development* 133:385—394.

45. Rushlow CA, Shvartsman SY (2012) Temporal dynamics, spatial range, and transcriptional interpretation of the Dorsal morphogen gradient. *Current Opinion in Genetics \& Development* 22:542—546.

46. Dubuis JO, Samanta R, Gregor T (2013) Accurate measurements of dynamics and reproducibility in small genetic networks. *Molecular Systems Biology* 9:.

47. Liberman LM, Reeves GT, Stathopoulos A (2009) Quantitative imaging of the Dorsal nuclear gradient reveals limitations to threshold-dependent patterning in Drosophila. *Proceedings of the National Academy of Sciences* 106:22317—22322.

48. Kicheva A, Pantazis P, Bollenbach T, Kalaidzidis Y, Bittig T, Julicher F, Gonzalez-Gaitan M (2007) Kinetics of Morphogen Gradient Formation. *Science* 315:521—525.

49. Gregor T, Tank DW, Wieschaus EF, Bialek W (2007) Probing the limits to positional information. *Cell* 130:153—164.

50. Rhee A, Cheong R, Levchenko A (2014) Noise decomposition of intracellular biochemical signaling networks using nonequivalent reporters. *Proceedings of the National Academy of Sciences* 111:17330—17335.

51. Little SC, Tikhonov M, Gregor T (2013) Precise Developmental Gene Expression Arises from Globally Stochastic Transcriptional Activity. *Cell* 154:789—800.

52. He F, Saunders TE, Wen Y, Cheung D, Jiao R, ten Wolde PRR, Howard M, Ma J (2010) Shaping a morphogen gradient for positional precision.. *Biophysical journal* 99:697—707.

53. Rushlow CA, Han K, Manley JL, Levine M (1989) The graded distribution of the dorsal morphogen is initiated by selective nuclear transport in Drosophila. *Cell* 59:1165—1177.

54. Steward R (1989) Relocalization of the dorsal protein from the cytoplasm to the nucleus correlates with its function. *Cell* 59:1179—1188.

55. Roth S, Stein D, Nusslein-Volhard C (1989) A gradient of nuclear localization of the dorsal protein determines dorsoventral pattern in the Drosophila embryo. *Cell* 59:1189—1202.

56. Haskel-Ittah M, Ben-Zvi D, Branski-Arieli M, Schejter ED, Shilo B, Barkai N (2012) Self-Organized Shuttling: Generating Sharp Dorsoventral Polarity in the Early Drosophila Embryo. *Cell* 150:1016—1028.

57. Stathopoulos A, Levine M (2002) Dorsal Gradient Networks in the Drosophila Embryo. *Developmental Biology* 246:57—67.

58. Markstein M, Markstein P, Markstein V, Levine MS (2002) Genome-wide analysis of clustered Dorsal binding sites identifies putative target genes in the Drosophila embryo. *Proceedings of the National Academy of Sciences* 99:763—768.

59. Levario TJ, Zhan M, Lim B, Shvartsman SY, Lu H (2013) Microfluidic trap array for massively parallel imaging of Drosophila embryos.. *Nature protocols* 8:721—736.

60. Gilbert SF (2003) Developmental biology. Cambridge, UK: Sinaeur.

61. Reeves GT, Trisnadi N, Truong TV, Nahmad M, Katz S, Stathopoulos A (2012) Dorsal-ventral gene expression in the Drosophila embryo reflects the dynamics and precision of the dorsal nuclear gradient.. *Developmental cell* 22:544—557.

62. Wessel AD, Gumalla M, Grosshans J, Schmidt CF (2015) The mechanical properties of early Drosophila embryos measured by high-speed video microrheology.. *Biophysical journal* 108:1899—1907.

63. Dsilva CJ, Lim B, Lu H, Singer A, Kevrekidis IG, Shvartsman SY (2015) Temporal ordering and registration of images in studies of developmental dynamics.. *Development (Cambridge, England)* 142:1717—1724.

64. Bangs P, White K (2000) Regulation and execution of apoptosis during Drosophila development. *Dev. Dyn.* 218:68—79.

65. Raser JM, O'Shea EK (2005) Noise in Gene Expression: Origins, Consequences, and Control. *Science* 309:2010—2013.

66. Ketola T, Kellermann VM, Loeschcke V, Lopez-Sepulcre A, Kristensen TN (2014) Does environmental robustness play a role in fluctuating environments?. *Evolution; international journal of organic evolution* 68:587—594.

67. Al-Saffar ZY, Grainger JNR, Aldrich J (1996) Temperature and humidity affecting development, survival and weight loss of the pupal stage of Drosophila melanogaster, and the influence of alternating temperature on the larvae. *Journal of Thermal Biology* 21:389—396.

68. Abouchar L, Petkova MD, Steinhardt CR, Gregor T (2014) Fly wing vein patterns have spatial reproducibility of a single cell. *Journal of the Royal Society, Interface / the Royal Society* 11

69. Coppey M, Boettiger AN, Berezhkovskii AM, Shvartsman SY (2008) Nuclear Trapping Shapes the Terminal Gradient in the Drosophila Embryo. *Curr Biol* 18:915—919.

70. Markow TA, Beall S, Matzkin LM (2009) Egg size, embryonic development time and ovoviviparity in Drosophila species. *Journal of Evolutionary Biology* 22:430—434.

71. Swaney KF, Huang CH, Devreotes PN (2010) Eukaryotic chemotaxis: a network of signaling pathways controls motility, directional sensing, and polarity.. *Annual review of biophysics* 39:265—289.

72. Levchenko A, Nemenman I (2014) Cellular noise and information transmission. *Current Opinion in Biotechnology* 28:156—164.

73. Munsky B, Neuert G, van Oudenaarden A (2012) Using Gene Expression Noise to Understand Gene Regulation. *Science* 336:183—187.

74. Endres RG, Wingreen NS (2008) Accuracy of direct gradient sensing by single cells.. *Proceedings of the National Academy of Sciences of the United States of America* 105:15749—15754.

75. Jilkine A, Edelstein-Keshet L (2011) A Comparison of Mathematical Models for Polarization of Single Eukaryotic Cells in Response to Guided Cues. *PLoS Comput Biol* 7:e1001121+.

76. Hu B, Chen W, Rappel W, Levine H (2010) Physical Limits on Cellular Sensing of Spatial Gradients. *Physical Review Letters* 105:48104.

77. Hu B, Chen W, Levine H, Rappel W (2011) Quantifying Information Transmission in Eukaryotic Gradient Sensing and Chemotactic Response. *Journal of Statistical Physics* 142:1167—1186.

78. Goodhill GJ, Urbach JS (1999) Theoretical analysis of gradient detection by growth cones. *J Neurobiol* 41:230—41.

79. Rosoff WJ, Urbach JS, Esrick MA, Mcallister RG, Richards LJ, Goodhill GJ (2004) A new chemotaxis assay shows the extreme sensitivity of axons to molecular gradients. *Nat Neurosci* 7:678—82.

80. Chung CY, Funamoto S, Firtel RA (2001) Signaling pathways controlling cell polarity and chemotaxis. *Trends in Biochemical Sciences* 26:557—566.

81. Takahashi Y, Sipp D, Enomoto H (2013) Tissue Interactions in Neural Crest Cell Development and Disease. *Science* 341:860—863.

82. Dona E, Barry JD, Valentin G, Quirin C, Khmelinskii A, Kunze A, Durdu S, Newton LR, Fernandez-Minan A, Huber W, Knop M, Gilmour D (2013) Directional tissue migration through a self-generated chemokine gradient. *Nature* 503:285—289.

83. Pocha SM, Montell DJ (2014) Cellular and Molecular Mechanisms of Single and Collective Cell Migrations in Drosophila: Themes and Variations. *Annual Review of Genetics* 48:295—318.

84. Lu P, Werb Z (2008) Patterning mechanisms of branched organs. *Science (New York, N.Y.)* 322:1506—1509.

85. Friedl P, Gilmour D (2009) Collective cell migration in morphogenesis, regeneration and cancer. *Nature reviews. Molecular cell biology* 10:445—457.

86. Gregor T, Fujimoto K, Masaki N, Sawai S (2010) The onset of collective behavior in social amoebae. *Science (New York, N.Y.)* 328:1021—1025.

87. Malet-Engra G, Yu W, Oldani A, Rey-Barroso J, Gov NS, Scita G, Dupre L (2015) Collective Cell Motility Promotes Chemotactic Prowess and Resistance to Chemorepulsion. *Current Biology*

88. Lin B, Yin T, Wu YI, Inoue T, Levchenko A (2015) Interplay between chemotaxis and contact inhibition of locomotion determines exploratory cell migration.. *Nature communications* 6

89. Camley BA, Zimmermann J, Levine H, Rappel W (2015) Emergent collective chemotaxis without single-cell gradient sensing. *arxiv.org/abs/1506.06698*

90. Taillefumier T, Wingreen NS (2014) Optimal census by quorum sensing. *PLoS Comput Biol* 11(5):e1004238.

91. Voisinne G, Nixon BG, Melbinger A, Gasteiger G, Vergassola M, Altan-Bonnet G (2015) T Cells Integrate Local and Global Cues to Discriminate between Structurally Similar Antigens.. *Cell reports* 11:1208—1219.

92. Sokolowski TR, Tkacik G (2015) Optimizing information flow in small genetic networks. IV. Spatial coupling. *Physical review. E, Statistical, nonlinear, and soft matter physics* 91

93. Lander AD (2015) Pattern, Growth, and Control. *Cell* 144:955—969.

94. Inman JL, Robertson C, Mott JD, Bissell MJ (2015) Mammary gland development: cell fate specification, stem cells and the microenvironment.. *Development (Cambridge, England)* 142:1028—1042.

95. Huebner RJ, Ewald AJ (2014) Cellular foundations of mammary tubulogenesis. *Seminars in Cell \& Developmental Biology* 31:124—131.

96. Sternlicht MD, Kouros-Mehr H, Lu P, Werb Z (2006) Hormonal and local control of mammary branching morphogenesis.. *Differentiation; research in biological diversity* 74:365—381.

97. Fata JE, Mori H, Ewald AJ, Zhang H, Yao E, Werb Z, Bissell MJ (2007) The MAPKERK-1,2 pathway integrates distinct and antagonistic signals from TGFα and FGF7 in morphogenesis of mouse mammary epithelium. *Developmental Biology* 306:193—207.

98. Ewald AJ, Brenot A, Duong M, Chan BS, Werb Z (2008) Collective Epithelial Migration and Cell Rearrangements Drive Mammary Branching Morphogenesis. *Developmental Cell* 14:570—581.

99. Nguyen-Ngoc KV, Shamir ER, Huebner RJ, Beck JN, Cheung KJ, Ewald AJ (2015) 3D culture assays of murine mammary branching morphogenesis and epithelial invasion.. *Methods in molecular biology (Clifton, N.J.)* 1189:135—162.

100. Schmeichel KL, Bissell MJ (2003) Modeling tissue-specific signaling and organ function in three dimensions.. *Journal of cell science* 116:2377—2388.

101. Coleman S, Silberstein GB, Daniel CW (1988) Ductal morphogenesis in the mouse mammary gland: Evidence supporting a role for epidermal growth factor. *Developmental Biology* 127:304—315.

102. Sebastian J, Richards RG, Walker MP, Wiesen JF, Werb Z, Derynck R, Hom YK, Cunha GR, DiAugustine RP (1998) Activation and function of the epidermal growth factor receptor and erbB-2 during mammary gland morphogenesis.. *Cell growth \& differentiation : the molecular biology journal of the American Association for Cancer Research* 9:777—785.

103. Roussos ET, Condeelis JS, Patsialou A (2011) Chemotaxis in cancer. *Nat Rev Cancer* 11:573—587.

104. Radice GL, Ferreira-Cornwell MC, Robinson SD, Rayburn H, Chodosh LA, Takeichi M, Hynes RO (1997) Precocious mammary gland development in P-cadherin-deficient mice. *The Journal of cell biology* 139:1025—1032.

105. Nguyen-Ngoc KV, Cheung KJ, Brenot A, Shamir ER, Gray RS, Hines WC, Yaswen P, Werb Z, Ewald AJ (2012) ECM microenvironment regulates collective migration and local dissemination in normal and malignant mammary epithelium. *Proceedings of the National Academy of Sciences of the United States of America* 109

106. Berg HC, Purcell EM (1977) Physics of chemoreception. *Biophysical Journal* 20:193—219.

107. Mugler A, Levchenko A, Nemenman I (2015) Limits to the precision of gradient sensing with spatial communication and temporal integration. *arxiv.org/abs/1505.04346*

108. Berg HC (2004) E. coli in motion. New York: Springer-Verlag.

109. Mortimer D, Dayan P, Burrage K, Goodhill GJ (2011) Bayes-optimal chemotaxis. *Neural computation* 23:336—373.

110. Hu B, Chen W, Rappel W, Levine H (2010) Physical Limits on Cellular Sensing of Spatial Gradients. *Physical Review Letters* 105:.

111. Iglesias PA, Levchenko A (2002) Modeling the cell's guidance system.. *Science's STKE : signal transduction knowledge environment* 2002:.

112. Levchenko A, Iglesias PA (2002) Models of Eukaryotic Gradient Sensing: Application to Chemotaxis of Amoebae and Neutrophils. *Biophysical Journal* 82:50—63.

113. Salameh A, Dhein S (2005) Pharmacology of Gap junctions. New pharmacological targets for treatment of arrhythmia, seizure and cancer? *Biochimica et Biophysica Acta (BBA) - Biomembranes* 1719:36—58.

114. Dittmar T, Husemann A, Schewe Y, Nofer JR, Niggemann B, Zanker KS, Brandt BH (2002) Induction of cancer cell migration by epidermal growth factor is initiated

by specific phosphorylation of tyrosine 1248 of c-erbB-2 receptor via EGFR. *FASEB journal* 16:1823—1825.

115. Zariwala HA, Borghuis BG, Hoogland TM, Madisen L, Tian L, De Zeeuw CI, Zeng H, Looger LL, Svoboda K, Chen TW (2012) A Cre-dependent GCaMP3 reporter mouse for neuronal imaging in vivo. *The Journal of neuroscience : the official journal of the Society for Neuroscience* 32:3131—3141.

116. Press WH, Teukolsky SA, Vetterling WT, Flannery BP (2007) Numerical Recipes 3rd Edition: The Art of Scientific Computing. Cambridge, UK: Cambridge University Press

117. Mani M, Goyal S, Irvine KD, Shraiman BI (2013) Collective polarization model for gradient sensing via Dachsous-Fat intercellular signaling. *Proceedings of the National Academy of Sciences* 110:20420—20425.

118. Bialek W, Cavagna A, Giardina I, Mora T, Silvestri E, Viale M, Walczak AM (2012) Statistical mechanics for natural flocks of birds. *Proceedings of the National Academy of Sciences* 109:4786—4791.

119. Gamal AE, Kim Y (2012) Network Information Theory. Cambridge, UK: Cambridge University Press.

120. Lu P, Ewald AJ, Martin GR, Werb Z (2008) Genetic mosaic analysis reveals FGF receptor 2 function in terminal end buds during mammary gland branching morphogenesis. *Developmental Biology* 321:77—87.

121. Osborne LC, Lisberger SG, Bialek W (2005) A sensory source for motor variation. *Nature* 437:412—416.

122. Gregor T, Bialek W, de Ruyter van Steveninck RR, Tank DW, Wieschaus EF (2005) Diffusion and scaling during early embryonic pattern formation. *Proceedings of the National Academy of Sciences of the United States of America* 102:18403—18407.

123. Tsai FC, Meyer T (2012) Ca2+ pulses control local cycles of lamellipodia retraction and adhesion along the front of migrating cells. *Current biology : CB* 22:837—842.

124. Haeger A, Wolf K, Zegers MM, Friedl P (2015) Collective cell migration: guidance principles and hierarchies. *Trends in Cell Biology* 25:556—566.

125. Huang CP, Lu J, Seon H, Lee AP, Flanagan LA, Kim HY, Putnam AJ, Jeon NLL (2009) Engineering microscale cellular niches for three-dimensional multicellular co-cultures. *Lab on a chip* 9:1740—1748.

126. Ewald AJ (2013) Practical considerations for long-term time-lapse imaging of epithelial morphogenesis in three-dimensional organotypic cultures.. *Cold Spring Harbor protocols* 2013:100—117.

127. Endres RG, Wingreen NS (2008) Accuracy of direct gradient sensing by single cells. *Proc Natl Acad Sci USA* 105:15749—54.

128. Thorne RG, Hrabetova S, Nicholson C (2004) Diffusion of epidermal growth factor in rat brain extracellular space measured by integrative optical imaging. *Journal of neurophysiology* 92:3471—3481.

129. Detwiler PB, Ramanathan S, Sengupta A, Shraiman BI (2000) Engineering aspects of enzymatic signal transduction: photoreceptors in the retina. *Biophysical journal* 79:2801—2817.

130. Gadgil C, Lee C, Othmer H (2005) A stochastic analysis of first-order reaction networks. *Bulletin of Mathematical Biology* 67:901—946.

131. Usmani RA (1994) Inversion of a tridiagonal jacobi matrix. *Linear Algebra and its Applications* 212-213:413—414.

132. Usmani RA (1994) Inversion of Jacobi's tridiagonal matrix. *Computers & Mathematics with Applications* 27:59—66.

133. Wartlick O, Kicheva A, González-Gaitán M (2009) Morphogen gradient formation. *Cold Spring Harb Perspect Biol* 1:a001255.

134. Amar P, Legent G, Thellier M, Ripoll C, Bernot G, Nystrom T, Saier MH, Norris V (2008) A stochastic automaton shows how enzyme assemblies may contribute to metabolic efficiency. *BMC Systems Biology* 2:27+.

135. Marshall CJ (1995) Specificity of receptor tyrosine kinase signaling: Transient versus sustained extracellular signal-regulated kinase activation. *Cell* 80:179—185.

136. Dolmetsch RE, Lewis RS, Goodnow CC, Healy JI (1997) Differential activation of transcription factors induced by Ca2+ response amplitude and duration. *Nature* 386:855—858.

137. Murphy LO, Smith S, Chen R, Fingar DC, Blenis J (2002) Molecular interpretation of ERK signal duration by immediate early gene products. *Nature Cell Biology* 4:556—564.

138. Harfe BD, Scherz PJ, Nissim S, Tian H, McMahon AP, Tabin CJ (2004) Evidence for an Expansion-Based Temporal Shh Gradient in Specifying Vertebrate Digit Identities. *Cell* 118:517—528.

139. Hilfinger A, Paulsson J (2011) Separating intrinsic from extrinsic fluctuations in dynamic biological systems. *Proceedings of the National Academy of Sciences* 108:12167—12172.

140. Acar M, Pando BF, Arnold FH, Elowitz MB, van Oudenaarden A (2010) A General Mechanism for Network-Dosage Compensation in Gene Circuits. *Science* 329:1656—1660.

141. Saltelli A, Bolado R (1998) An alternative way to compute Fourier amplitude sensitivity test (FAST). *Computational Statistics \& Data Analysis* 26:445—460.

142. Python Software Foundation. Python Language Reference, version 2.7.

143. Walt Svd, Colbert SC, Varoquaux G (2011) The NumPy Array: A Structure for Efficient Numerical Computation. *Computing in Science & Engineering* 13:22-30.

144. Team RC (2014) R: A Language and Environment for Statistical Computing. :.

145. Pujol G, Iooss B, with contributions from Paul Lemaitre AJ, Gilquin L, Gratiet LL, Touati T, Ramos B, Fruth J, Veiga SD (2014) sensitivity: Sensitivity Analysis. :.

146. Tu Y, Stolovitzky G, Klein U (2002) Quantitative noise analysis for gene expression microarray experiments. *Proceedings of the National Academy of Sciences* 99:14031—14036.

147. Snijder B, Pelkmans L (2011) Origins of regulated cell-to-cell variability. *Nature Reviews Molecular Cell Biology* 12:119—125.

148. Pelkmans L (2012) Using Cell-to-Cell Variability—A New Era in Molecular Biology. *Science* 336:425—426.

149. Patten I, Placzek M (2000) The role of Sonic hedgehog in neural tube patterning. *Cellular and molecular life sciences : CMLS* 57:1695—1708.

150. Purnick PEM, Weiss R (2009) The second wave of synthetic biology: from modules to systems. *Nat Rev Mol Cell Biol* 10:410—422.

CURRICULUM VITAE

MATTHEW BRENNAN

EDUCATION

Ph.D. Biomedical Engineering — 2015
Johns Hopkins University, Baltimore, MD
Advisor: Dr. Andre Levchenko

M.S. Electrical Engineering — 2008
University of Southern California, Los Angeles, CA
Advisor: Dr. Giuseppe Caire

B.S. Computer Systems Engineering — 2006
University of Massachusetts, Amherst, MA

B.S. Electrical Engineering — 2006
University of Massachusetts, Amherst, MA

PROFESSIONAL EXPERIENCE

Special Asst to the Under Secretary for Science & Tech — 2009-2011
Department of Homeland Security

State Data Director — 2007-2008
Obama for America

Research Assistant — 2007
Lab of Guisseppe Caire, University of Southern California

Communications Research and Development Intern — 2007
Northrop Grumman Space Technology

Wideband Tactical Networking Intern — 2006
MIT – Lincoln Laboratory

Computer Engineering Co-op — 2003-2005
National Security Agency

FELLOWSHIPS AND AWARDS

2011 NIH Biomedical Engineering PhD Training Grant Recipient
2007 NSF Graduate Research Fellow
2006 USC Viterbi School of Engineering Dean's Fellow

PUBLICATIONS

Suhail Y, Kshitiz, Lee J, Walker M, DKim DH, Brennan MD, Bader JS, Levchenko A. (2013) Modeling intercellular transfer of biomolecules through tunneling nanotubes. Bulletin of mathematical biology. Volume: 75 (8), 1400-1416

Brennan MD, Cheong R, Levchenko A. (2012) How Information Theory Handles Cell Signaling and Uncertainty. Science. Volume: 338, 6105

Sorber J, Kostadinov A, Garber M, Brennan M, Corner MD, Berger ED. *Eon: A Language and Runtime System for Perpetual Systems.* Proceedings of the Fifth International ACM Conference on Embedded Networked Sensor Systems (SenSys '07), 161-174.

PRESENTATIONS

Noise Sources and Accuracy of Drosophila Dorsoventral Patterning. MD Brennan, B Lim, R Cheong, SY Shvartsman, A Levchenko. The Sixth q-bio Conference, August 2012

*Generalization of Channel Blockage Profiles for SATCOM On-The-Move Using 3-D Models***.** MD Brennan, WM Smith. Proceedings of IEEE Military Communication Conference (MILCOM'06), Washington, DC, October 2006.

TEACHING

2013 Teaching Assistant, Systems Biology 3, Department of Biomedical Engineering, Johns Hopkins University